Università degli studi di Firenze

Scuola di Scienze Matematiche Fisiche e Naturali

Corso di Laurea Magistrale in Scienze Fisiche e Astrofisiche

Elaborato finale

Tailored optical potentials for experiments with atomic superfluids

Potenziali ottici su misura per esperimenti con superfluidi atomici

Anno Accademico 2016-2017

Candidate: **Giulia Del Pace** *Supervisor:* **Dr. Francesco Minardi**

Contents

Introduction

Ultracold atoms and quantum gases are very clean and controllable systems, that can be considered as novel quantum materials and quantum simulators. Hence, they offer an ideal playground to study phenomena otherwise difficult to approach in many fields of research, from condensed matter to high-energy physics and cosmology. In this framework, the study of superfluidity phenomena with cold atoms opens the way for the implementation of new quantum devices, which requires a deep understanding of the superfluid properties and of the possible dissipation in the material. With atomic superfluids it is indeed possible to investigate the intrinsic quantum nature of the superfluid phase and the main occurring excitations.

Both superfluidity and superconductivity are intimately connected to the Bose-Einstein condensation. Such phenomenon was suggested by Einstein in 1924 [1], following the work of Bose on the black body radiation [2] and corresponds to a low temperature phase transition in bosonic systems. Below a certain critical temperature the ground state of the system starts to be extensively occupied by particles that share the same wavefunction. When particles are weakly interacting, Bose-Einstein condensation leads to a superfluid behavior of the system, namely the capability to flow with zero viscosity.

The study of superfluids began in 1911, when Onnes [3] observed that the electrical resistance of mercury vanishes to zero at temperature below 4 K. It was the first experimental evidence of superconductivity. Later, in 1938 a similar dissipation-less flow was observed in liquid ^{4}He in parallel by P. Kapitza [4] and J. F. Allen [5]: when cooled to temperature lower than 2.17 K the viscosity of such fluid rapidly goes to zero. The superfluid behavior of liquid helium was soon explained as the manifestation of Bose-Einstein condensation by F. London [6], but the same explanation is not applicable to the superconductor behavior of metals instead, where the conduction is performed by electrons that are fermionic particles. It took nearly 20 years to understand the microscopic mechanism behind superconductivity: in 1957 J. Bardeen, L. N. Cooper and J. R. Shrieffer formulated the BCS theory [7], which describes superconductivity as a microscopic effect caused by the condensation of Cooper pairs of electrons in a boson-like state.

Ultracold atoms can be used to study superfluidity phenomena, as condensation with bosonic atoms can be achieved at temperature of the orther of 100 nK. The first Bose-Einstain condensate in diluite atomic gases was observed in 1995 by the groups of E. Cornell and C. Wieman at Boulder [8], and a few months later by W.

Ketterle at MIT [9]. Since then, many superfluid properties has been probed in an atomic Bose-Einstein condensate, such as the dissipation-less flow and the creation of quantized vortices under rotation [10] [11] [12]. Atomic systems are particularly suited for the study of superfluidity, as many parameters can be finely controlled, such as the interparticles interaction, the dimensionality and the confining geometry of the gas. The latter can be adjusted using the conservative optical dipole force that light exert on an atomic system. Indeed, the electromagnetic field of the radiation induces a dipole on atoms, that in turn interact with the external electric field, giving rise to an optical potential that depends on the intensity of the radiation. In this way it is possible to trap atoms in local minima or maxima of the intensity, depending upon the laser light frequency. Then, the control over the intensity spatial profile permits to create any desired trapping geometry. In particular, it can be done using Spatial Light Modulator (SLMs), a family of tools which permits to imprint arbitrary spatially varying modulations on an incident light beam. In this context, the Digital Micromirror Device (DMD) is becoming a fundamental tool in cold atoms experiments to implement tailored optical potentials. It is a reflecting SLM, composed by an array of micrometer-sized mirror, through which both static and time-dependent light pattern can be created. In [13], a DMD is used to create a ring-shaped optical potential for a ^{23}Na Bose-Einstain condensate to study persistent current in the superfluid, whereas in [14] and [15] it is implemented to perform multiple-site addressing in periodic optical potential.

The aim of this thesis work was to realize and characterize tailored optical potentials with a DMD, focusing the attention on those geometry that are interesting for experiments with atomic superfluids. In particular, I designed and aligned two different optical setup for the characterization of homogeneous light patterns and disordered potentials respectively. For the first part I wrote a feedback program to improve the DMD-made image quality and to obtain a better overlap with the target patterns projected with the DMD. Then, I implemented a DMD-based technique to measure the resolution of an optical system, and later I used an high-resolution optical system to create disordered potentials on length scales of a μm. Moreover, part of my thesis was dedicated to the realization of a magneto optical trap of ^{87}Rb as the initial part of the construction of a novel experiment with a Bose-Bose mixture for the study of two-components superfluids. This part of the thesis was performed in Lab. 29 of Dipartimento di Fisica e Astronomia in Florence. In particular, I took part in the alignment of the optical setup for the 2D and 3D MOT, and optimized the loading efficiency of the 3D MOT.

The outline of this thesis is the following. In the first chapter I report the main features of Bose-Einstein condensation and analyze its connection with superfluidity. Then, I illustrate how light can be used to manipulate atoms, both to cool and to trap them, and describe two main applications of optical potentials in probing the superfluid behavior: a ring potential to study persistent current and disordered potentials to investigate the superfluid-to-insulator transition.

In the second chapter, I present my work in aligning and optimizing the 3D MOT

of ^{87}Rb. After a brief illustration of the working principle of such cooling technique, I present the experimental setup and the performed measurement for the optimization.

In the third chapter, I describe the DMD and present the optical setup that I used to create tailored optical potentials. In particular, I explain the feedback process used to improve the image quality and analyze the properties of DMD-made time-dependent potentials.

Finally, in the fourth chapter, I present the high-resolution optical system used to create disordered optical potentials. First, the DMD-based technique to measure the resolution of the system is described and the results of such measurement are reported. Then, I illustrate the capability of the system to image disordered potential on the length scale of a μm. In particular, I analyzed two different kinds of disorder, speckles and point-like patterns, and implemented a method to pass the one through the other modifying the resolution of the optical system.

Chapter 1

Theory of atomic superfluidity

In this chapter, the phenomenon of Bose-Einstein condensation is presented from a theoretical point of view. The existence of a low temperature phase transition in a system of bosons was firstly postulated by Einstein in 1921 [1], by following the work of Bose on the black body radiation [2]. In the following, the Bose-Einstain condensation is presented both in the case of an ideal gas, in Sec. 1.1, and for a weakly interacting one, in Sec. 1.2. Such phenomenon can be investigated with ultracold bosonic atoms, despite they are composed by fermionic particles, because in case of weak interactions the internal structure of an atom is not resolved during a scattering process, so it can be considered as only one particle, which statistic is determined by the value of its total angular momentum. Therefore, atoms can exhibit either a fermionic or a bosonic behavior, depending on their internal structure. In the case of bosons, a notable application of Bose-Einstein condensation is the study of its superfluid behavior, namely the ability of the fluid to flow through a channel without dissipation. The connections between condensation and superfluidity are presented in Sec. 1.3. Ultracold atoms are particularly suitable to study superfluidity, because they are very controllable systems, in which the interactions between particles, the dimensionality and the trapping geometry can be adjusted at will. In particular, confining potentials for atomic systems can be created using far off-resonance light, as it will be explained in Sec. 1.4: shaping the spatial intensity profile of a laser beam it is possible to create any desired trapping geometry. In this chapter, two of the main interesting applications of optical potentials in a superfluid system are presented: a ring-shaped confining potential to study persistent currents in a superfluid, and disordered potentials to investigate the superfluid-to-insulator transition.

1.1 Bose-Einstein condensation of an ideal gas

Bosons are particles with integer spin. The wavefunction that describes a system of identical bosons has to be symmetric under the exchange of any two particles, and it does not obey the Pauli exclusion principle .Therefore, two or more identical bosons can occupy the same state, which gives rise to the Bose-Einstein condensation (BEC), a macroscopic occupation of the single particle ground state [16]. We can estimate

the critical temperature of the BEC transition considering that particles exhibit their quantum nature when the interparticle spacing become comparable to their thermal de Broglie wavelength, defined as:

$$\lambda_T = \left(\frac{2\pi\hbar^2}{m k_B T} \right)^{\frac{1}{2}}, \tag{1.1}$$

where $\hbar$ is the Planck constant, k_B the Boltzmann constant, m the mass of particles and T their temperature. On the other hand, the mean interparticle distance depends on the particles density n: $d = n^{-\frac{1}{3}}$. By equating these two quantities, we obtain an evaluation of the critical temperature of condensation. In particular, in an experiment with alkali atoms the particles density is 10^{14} cm^{-3}, so that the transition temperature is of the order of 100 nK.

More formally, we can obtain the exact expression of the transition temperature by calculating the number of atoms in the excited state. To do that, we start from the mean occupation number of single-particle state, that for ideal non-interacting bosons is given by the Bose distribution function. For a system with energy levels ϵ_n with $\epsilon_0 = 0$ for simplicity, that is [17]:

$$f(\epsilon_n) = \frac{1}{e^{(\epsilon_n - \mu)/k_B T} - 1}, \tag{1.2}$$

where μ is the chemical potential, determined as a function of the number of particles N and the temperature T such that N is conserved. For the distribution $f(\epsilon)$ to be positive for all states, the chemical potential is limited by $\mu < 0$, as $\epsilon_0 = 0$ is the minimum energy for the system. That means that, while the occupation of the ground state can be arbitrarily large, the occupation number of any excited state is constrained to be less than $1/(\exp[\epsilon_n/k_B T] - 1)$. The number of particles can now be computed as the sum of the mean occupation number over all the possible energy states. To characterize the Bose-Einstein transition, it is convenient to separate the total number of atoms in two contribution: the number of atoms N_0 in the ground state at $n = 0$, and the number of atoms in the excited states for $n > 0$:

$$N = \sum_n f(\epsilon_n) = N_0 + \sum_{n>0} f(\epsilon_n). \tag{1.3}$$

If the energy levels spacing is much less than $k_B T$, we can replace the sum with an integral:

$$N = N_0 + \int_0^{+\infty} f(\epsilon) g(\epsilon) d\epsilon, \tag{1.4}$$

where $g(\epsilon)$ is the density of state. The number of atoms in the excited state is thus equal to:

$$N_{ex} = \int_0^{+\infty} f(\epsilon) g(\epsilon) d\epsilon, \tag{1.5}$$

and takes its maximum value for greatest value for $\mu = 0$. The transition temperature T_C is determined by the condition that the total number of particles can be

accommodated in excited states, namely [16]:

$$N = N_{ex}(T = T_C, \mu = 0) = \int_0^{+\infty} g(\epsilon) \frac{1}{\exp[\epsilon/k_B T_C] - 1}. \tag{1.6}$$

We note that the density of state $g(\epsilon)$ depends on the confining potential felt by the atoms, so the critical temperature will depend on it too.

We can study the condensation in different trapping potential, by using a semi-classical approach. In this case we can define a local distribution function $f_{\mathbf{p}}(\mathbf{r})$:

$$f_{\mathbf{p}}(\mathbf{r}) = \frac{1}{\exp^{(\epsilon_{\mathbf{p}}(\mathbf{r})-\mu)/k_B T} - 1}, \tag{1.7}$$

where $\epsilon_{\mathbf{p}}(\mathbf{r})$ is the particles energy in the point $\mathbf{r}$:

$$\epsilon_{\mathbf{p}}(\mathbf{r}) = \frac{p^2}{2m} + V(\mathbf{r}), \tag{1.8}$$

where $V(\mathbf{r})$ is the external trapping potential. In such semi-classical approach, $f_{\mathbf{p}}(\mathbf{r}) d\mathbf{p} d\mathbf{r}$ denotes the mean number of particles in the phase space volume $d\mathbf{p}d\mathbf{r}$, so that the density of particles that occupy the excited states can be calculated as:

$$n_{ex}(\mathbf{r}) = \int \frac{d\mathbf{p}}{(2\pi\hbar)^3} \frac{1}{\exp[(\epsilon_{\mathbf{p}}(\mathbf{r}) - \mu)/k_B T] - 1}. \tag{1.9}$$

By solving such integral, we obtain:

$$n_{ex}(\mathbf{r}) = \frac{g_{\frac{3}{2}}(z(\mathbf{r}))}{\lambda_T^3}, \tag{1.10}$$

where $z(\mathbf{r}) = \exp[(\mu - V(\mathbf{r}))/k_B T]$ is the fugacity and $g_{\frac{3}{2}}$ is the polylogarithm function defined as:

$$g_\gamma(z) = \sum_{n=1}^{\infty} \frac{z^n}{n^\gamma}. \tag{1.11}$$

From such expression of the density of atoms in the excited state, we can thus calculate the critical temperature for condensation in different trapping geometries. In particular, we focus our attention to a uniform, an harmonic and a ring-shaped trapping potentials.

1.1.1 Uniform trapping potential

In a uniform trapping potential $V(\mathbf{r}) = 0$, so that the fugacity $z = e^{\mu/k_B T}$ reaches its maximum value for $\mu \to 0$. In such limit we have $z(\mathbf{r}) \to 1$ and thus $g_{\frac{3}{2}}(z) \to g_{\frac{3}{2}}(1) = 2.612$. This gives an upper bound to the density of particles in the excited state:

$$n_{ex}^{max} = n_{ex}(\mu = 0) = \frac{2.612}{\lambda_T^3}. \tag{1.12}$$

As already stated, the critical temperature is the one at which the number of atoms in the excited state is maximum. Therefore, we obtain the expression of the critical

temperature for a uniform gas by using Eq. (1.12) and the definition of the de Broglie wavelength:

$$T_C = \frac{2\pi\hbar^2}{mk_B}\left(\frac{n}{g_{\frac{3}{2}(1)}}\right)^{\frac{2}{3}}, \tag{1.13}$$

where we have considered all the particles to be in the excited state, namely $n_{ex} = n$.

From such expression of the critical temperature, it is possible to calculate the condensed fraction N_0/N. Indeed, Eq. (1.10) says that the density of particles in the excited state scales as $T^{\frac{3}{2}}$, therefore the number of atoms in the excited state can be written as $N_{ex} = N(T/T_C)^{\frac{3}{2}}$. The number of particles in the ground state is thus:

$$N_0 = N - N_{ex} = N\left[1 - \left(\frac{T}{T_C}\right)^{\frac{3}{2}}\right]. \tag{1.14}$$

The condensed fraction increases as the temperature decreases, reaching its maximum $N_0/N = 1$ when $T = 0$: as expected at zero temperature all the particles occupy the ground state, but a macroscopic occupation of such state is present also for finite temperatures.

We note that the same results can be obtained by considering the density of state in a uniform potential of volume V:

$$g(\epsilon) = \frac{Vm^{3/2}}{2^{1/2}\pi^2\hbar^3}\epsilon^{1/2}. \tag{1.15}$$

Inserting such expression in Eq. (1.6), the integral can be solved and the results give the same expression of the density of particles in the excited state of Eq. (1.10).

1.1.2 Harmonic trapping potential

Experiments with cold atoms are usually performed in an harmonic trapping potential, so it is interesting to study how Bose-Einstein condensation can be described in this case. To do that, we now consider the three-dimensional harmonic trapping potential:

$$V(\mathbf{r}) = \frac{m}{2}\left(\omega_x^2x^2 + \omega_y^2y^2 + \omega_z^2z^2\right), \tag{1.16}$$

where ω_i for $i = 1, 2, 3$ are the trapping frequency in the three dimensions. This yields a quantised energy spectrum of single-particle energies that are labelled by the non-negative quantum numbers n_x, n_y, n_z:

$$\epsilon_{n_x,n_y,n_z} = \hbar(n_x\omega_x + n_y\omega_y + n_z\omega_z) + \epsilon_0, \tag{1.17}$$

where $\epsilon_0 = \hbar(\omega_x\omega_y\omega_z)/2$ is the zero point energy. As already mentioned, condensation occurs when the chemical potential takes its maximum value, that in the case of an harmonic potential is when $\mu = \epsilon_0$. In this case, the critical temperature can be calculated directly from the expression for the number of particles in the excited state, that for the energy levels of the harmonic oscillator is [18]:

$$N_{ex} = \int_0^{+\infty} \frac{dn_x dn_y dn_z}{\exp[\hbar(\omega_x n_x + \omega_y n_y + \omega_z n_z)/k_BT] - 1}, \tag{1.18}$$

where we have again replaced the sum over all the possible states with an integral, assuming that $k_B T \gg \hbar\omega_0$, where $\omega_0 = (\omega_x\omega_y\omega_z)^{1/3}$ is the geometric mean of the trapping frequencies. Such integral can be analytically solved with the change in variables: $\hbar\omega_i n_i/k_B T = n_i'$. Therefore, for the number of particles in the excited state we obtain [18]:

$$N_{ex} = g_3(1)\left(\frac{k_B T}{\hbar\omega_0}\right). \tag{1.19}$$

The critical temperature is defined to be the temperature at which $N = N_{ex}$, so it can be calculated from the previous expression:

$$T_C = \frac{\hbar\omega_0}{k_B}\left(\frac{N}{g_3(1)}\right)^{\frac{1}{3}}. \tag{1.20}$$

Then, the condensed fraction can be obtained remembering that $N = N_0 + N_{ex}$, so that for $T \leq T_C$:

$$\frac{N_0}{N} = 1 - \left(\frac{T}{T_C}\right)^3. \tag{1.21}$$

As in the case of uniform potential, the condensed fraction increases as the temperature decreases, but with a different power law.

We now consider the density distribution of particles. For a non interacting gas, the density distribution of the condensed particles can be computed from the ground state wavefunction of a three-dimensional harmonic oscillator:

$$n_0(\mathbf{r}) = N_0|\psi_0(\mathbf{r})|^2 = N_0\left(\frac{m\omega_0}{\pi\hbar}\right)^{\frac{3}{2}}\exp\left[-\left(\frac{x}{a_x}\right)^2 - \left(\frac{y}{a_y}\right)^2 - \left(\frac{z}{a_z}\right)^2\right], \tag{1.22}$$

where $a_i = \sqrt{\hbar/m\omega_i}$ is the oscillator length in the i direction. For the density of particles in the excited states, we can consider the semi-classical expression of Eq. (1.10), that in the case of an harmonic oscillator for $T \leq T_C$ can be written as:

$$n_{ex}(\mathbf{r}) = \frac{g_{\frac{3}{2}}(\exp[-V(\mathbf{r})/k_B T])}{\lambda_T^3} = \frac{g_{\frac{3}{2}}\left(\exp[-m(\omega_x^2 x^2+\omega_y^2 y^2+\omega_z^2 z^2)/2k_B T]\right)}{\lambda_T^3}. \tag{1.23}$$

For typical experimental parameters, the width of n_0 is much narrower than the width of the thermal distribution. Therefore, in an harmonically trapped gas condensation happens also in the real space, in addition to the condensation in the momentum space, as particles occupy the same state. In particular, the occurrence of condensation can be verified by observing the sharp peak in the central region of particles density distribution.

1.1.3 Ring-shaped trapping potential

As it will be depicted in detail in Sec. 1.4, a ring-shaped potential can be used to study persistent currents in an atomic superfluid. Therefore, it is interesting to investigate how the critical temperature of condensation is modified by such trapping geometry.

In particular, we consider that in the (x, y) plane atoms are confined in a ring-shaped potential, such that the potential at the edges of the ring is infinite, whereas in the z direction they are trapped in an harmonic potential. The ring landscape on the (x, y) plane is topologically analogue to a rectangular box, with dimensions fixed by the radial width and the circular length of the ring. So for simplicity, we study the condensation in a rectangular potential in the (x, y) plane. Therefore, the three-dimensional confining potential felt by atoms can be written as:

$$V(\mathbf{r}) = \frac{1}{2}m\omega^2 z^2 + V_{box}(x, y), \tag{1.24}$$

where m is the mass of atoms, ω the frequency of the harmonic trap in the z direction, and $V_{box}(x, y)$ is the rectangular box potential in the (x, y) plane, defined to be 0 inside the box and infinite elsewhere.

To calculate the critical temperature, we can start from the semi-classical expression of the density of particles of Eq. (1.10), and calculate the number of atoms in the excited state as:

$$N_{ex} = \int n_{ex}(\mathbf{r})d\mathbf{r} = \int \frac{g_{3/2}(z(\mathbf{r}))}{\lambda_T^3}d\mathbf{r}, \tag{1.25}$$

where the fugacity $z(\mathbf{r})$ can be written as:

$$z(\mathbf{r}) = e^{(\mu - V(\mathbf{r}))/k_BT} = e^{\mu/k_BT}e^{-V(\mathbf{r})/k_BT} = z_0 e^{-V(\mathbf{r})/k_BT}. \tag{1.26}$$

Using the definition of the polylogarithm function, the number of particles in the excited state become:

$$\begin{aligned} N_{ex} &= \frac{1}{\lambda_T^3}\int d\mathbf{r}\sum_{n=1}^{\infty}\frac{z_0^n e^{-nV(\mathbf{r})/k_BT}}{n^{3/2}} = \\ &= \frac{1}{\lambda_T^3}\sum_{n=1}^{\infty}\frac{z_0^n}{n^{3/2}}\int e^{-nV(\mathbf{r})/k_BT}d\mathbf{r} \end{aligned} \tag{1.27}$$

The integral in the previous expression can be computed, by inserting the expression of the potential:

$$\int e^{-nV(\mathbf{r})/k_BT}d\mathbf{r} = \int_{box} dxdy \int_{-\infty}^{+\infty} e^{-nm\omega^2 z^2/k_BT}dz, \tag{1.28}$$

where the integral over x and y is extended on the rectangular box area. Therefore, it gives simply the area of the rectangular box A_{box}, while that over the z variable is the integral of a Gaussian function that can be easily computed to give:

$$\int e^{-nV(\mathbf{r})/k_BT}d\mathbf{r} = A_{box}\sqrt{2\pi}\left(\frac{k_BT}{nm\omega^2}\right)^{\frac{1}{2}}. \tag{1.29}$$

By inserting such result in the expression for the number of particles in the excited state, we get:

$$N_{ex} = \frac{A_{box}}{\lambda_T^3}\left(\frac{2\pi k_BT}{m\omega^2}\right)^{\frac{1}{2}}\sum_{n=1}^{\infty}\frac{z_0^n}{n^2}. \tag{1.30}$$

The last sum correspond to the definition of the polylogarithm function $g_2(z_0)$, therefore at a given temperature T and chemical potential μ the number of particles in the excited state can be written as:

$$N_{ex}(\mu, T) = \frac{A_{box}}{\lambda_T^3} \left(\frac{2\pi k_B T}{m\omega^2} \right)^{\frac{1}{2}} g_2(z_0). \tag{1.31}$$

We can now find the critical temperature, remembering that condensation happens when $\mu = 0$ and $N_{ex} = N$, where N is the total number of particles. Under these conditions, the previous expression becomes:

$$N = \frac{A_{box}}{\lambda_T^3} \left(\frac{2\pi k_B T_C}{m\omega^2} \right)^{\frac{1}{2}} g_2(1). \tag{1.32}$$

The expression of the critical temperature in a ring geometry can thus be obtained by considering the temperature dependence of the de Broglie wavelength and noting that $g_2(1) = \zeta(2) = 1.645$. In this way we get:

$$T_C = \frac{a_{ho}\hbar\omega}{k_B} \sqrt{\frac{2\pi N}{A_{box}\zeta(2)}}, \tag{1.33}$$

where we have introduced the oscillator length $a_{ho} = \sqrt{\hbar/m\omega}$. Therefore, for a condensate in a ring trap the critical temperature depends on the number of particles to the 1/2 power. From such expression of the critical temperature, we can calculate the condensed fraction:

$$\frac{N_0}{N} = 1 - \left(\frac{T}{T_C} \right)^2. \tag{1.34}$$

As for the uniform and the harmonic potentials, the condensed fraction increases as the temperature decreases, but with a different power law.

The critical temperature for a gas of ^{87}Rb atoms can be estimated by considering a ring potential with radius $r_1 = 10\ \mu$ and $r_2 = 20\ \mu$, and a frequency for the harmonic trap of $\omega = 2\pi \times 100$ Hz. In this case we obtain $T_C \simeq 100$ nK.

1.2 Weakly interacting Bose gas

In the previous section, we saw that an ideal gas of non-interacting bosons can undergo to the Bose-Einstein condensation for sufficiently low temperatures. In reality particles always interact, and even weak interactions modify the behavior of a condensate. In particular, interactions modify the equilibrium state and the dynamical properties of a condensate, and play a fundamental role in the superfluid properties of condensates.

Interactions in an atomic gas are due to the Van der Waals force. In an ultracold gas it leads mainly to two-body collisions, because collisions involving three or more particles are unlike due to the low density. In particular, when both the de Broglie wavelength and the mean distance d between atoms are much greater than the range of the interaction potential, we can describe the two-body scattering process with only

one parameter, the scattering length a [16]. This is always true for an ultracold gas, where $\lambda_T \sim d \sim 100$ nm, whereas the range of the interacting potential is $r_0 \sim 5$ nm. Therefore, interactions in an ultracold atomic gas can be completely described with the scattering length. In particular, as the range of the interaction potential is so short, only its spatial average matters, while its detailed behavior is irrelevant. Therefore we can define a delta-like pseudopotential:

$$V_{pseudo}(\mathbf{r}) = g\delta(\mathbf{r}), \tag{1.35}$$

where g is taken such that the pseudopotential reproduces the scattering properties of the real potential, i.e. the two potential have the same scattering length. With such constrain, it can be demonstrated that [16]:

$$g = \frac{4\pi\hbar^2 a}{m}. \tag{1.36}$$

In the following we will use the pseudopotential to describe the interacting Bose gas. In particular, in Sec. 1.2.1 we derive the Gross-Pitaevski equation that allows to find the ground state of the interacting Bose gas. Then, in Sec. 1.2.2 we describe the Thomas-Fermi regime, when the interacting energy prevails over the kinetic energy, and finally in Sec. 1.2.3 we present the excitation spectrum of the interacting Bose gas.

1.2.1 Gross-Pitaevskii equation

To describe a gas of interacting bosons, we can consider the many body Hamiltonian [18]:

$$\begin{aligned}\hat{H} = &\int d\mathbf{r}\hat{\Psi}^\dagger(\mathbf{r})\left[-\frac{\hbar^2}{2m}\nabla^2 + V_{ext}(\mathbf{r})\right]\hat{\Psi}(\mathbf{r}) + \\ &+ \frac{1}{2}\int d\mathbf{r}d\mathbf{r'}\hat{\Psi}^\dagger(\mathbf{r})\hat{\Psi}(\mathbf{r})V(\mathbf{r}-\mathbf{r'})\hat{\Psi}(\mathbf{r'})\hat{\Psi}^\dagger(\mathbf{r'}),\end{aligned} \tag{1.37}$$

where $\hat{\Psi}^\dagger(\mathbf{r})$ and $\hat{\Psi}(\mathbf{r})$ are the creation and annihilation operators for a boson at position $\mathbf{r}$ respectively, and $V(\mathbf{r}-\mathbf{r'})$ is the interacting potential. The field operators satisfy the usual Bose commutation rules:

$$\begin{aligned}&[\hat{\Psi}(\mathbf{r}), \hat{\Psi}^\dagger(\mathbf{r'})] = \delta(\mathbf{r}-\mathbf{r'}) \\ &[\hat{\Psi}(\mathbf{r}), \hat{\Psi}(\mathbf{r'})] = [\hat{\Psi}^\dagger(\mathbf{r}), \hat{\Psi}^\dagger(\mathbf{r'})] = 0.\end{aligned} \tag{1.38}$$

Instead of solving exactly the many-body problem, we can use a mean-field approach, that allows to understand the physical behaviour of the system, while avoiding heavy calculations. At $T \leq T_C$ the ground state is macroscopically populated, so that we can separate out the condensate contribution to the field operator and write:

$$\hat{\Psi}(\mathbf{r}, t) = \Phi(\mathbf{r}, t) + \delta\hat{\Psi}(\mathbf{r}, t), \tag{1.39}$$

where $\Phi(\mathbf{r}, t) = \langle\Psi(\mathbf{r}, t)\rangle$ is a complex number defined as the expectation value of the field operator on the condensate state, and $\delta\hat{\Psi}$ is a small perturbation due to atoms

not in the ground state. The function $\Phi(\mathbf{r},t)$ is a classical field, that represent the order parameter or wavefunction of the condensate.

The equation for the condensate wavefunction $\Phi(\mathbf{r},t)$ can be derived from the time-evolution of the field operator in the Heisenberg description:

$$\begin{aligned}&\frac{\partial}{\partial t}\hat{\Psi}(\mathbf{r},t) = [\hat{\Psi},\hat{H}] = \\ &= \left[-\frac{\hbar^2\nabla^2}{2m} + V_{ext}(\mathbf{r}) + \int d\mathbf{r'}\hat{\Psi}^\dagger(\mathbf{r'},t)V(\mathbf{r}-\mathbf{r'})\hat{\Psi}(\mathbf{r'},t)\right]\hat{\Psi}(\mathbf{r},t)\end{aligned} \tag{1.40}$$

To the zeroth order, the field operator can be replaced by its mean value $\Phi(\mathbf{r},t)$, neglecting the perturbation $\delta\hat{\Psi}(\mathbf{r},t)$. Moreover, we can describe the interparticles interaction with the pseudopotential $V(\mathbf{r}) = g\delta(\mathbf{r})$. In this way we obtain the Gross-Pitaevskii equation (GPE) [18]:

$$i\hbar\frac{\partial}{\partial t}\Phi(\mathbf{r},t) = \left(-\frac{\hbar^2\nabla^2}{2m} + V_{ext}(\mathbf{r}) + g|\Phi(\mathbf{r},t)|^2\right)\Phi(\mathbf{r},t) \tag{1.41}$$

The ground state of a Bose gas can be easily obtained from the GPE by separating out the time dependency of the condensate wavefunction: $\Phi(\mathbf{r},t) = \phi(\mathbf{r})\exp[-i\mu t/\hbar]$, where μ is the chemical potential. The GPE then become:

$$\left(-\frac{\hbar^2\nabla^2}{2m} + V_{ext}(\mathbf{r}) + g\phi^2(\mathbf{r})\right)\phi(\mathbf{r}) = \mu\phi(\mathbf{r}) \tag{1.42}$$

Such equation has the form of a non-linear Schrödinger equation, where the effect of interactions is to add a mean field potential, proportional to the condensate density $n(\mathbf{r}) = |\phi|^2(\mathbf{r})$.

1.2.2 Thomas-Fermi regime

A simple solution for the ground state of the condensate can be found if the kinetic energy can be neglected respect to the interaction energy. This is valid for a condensate whose size due to interatomic repulsion grows well beyond the extension of the single-particle ground state. This approach is called Thomas-Fermi approximation and yields to the following simplified GPE [16]:

$$[V_{ext}(\mathbf{r}) + g|\Phi(\mathbf{r})|^2]\Phi(\mathbf{r}) = \mu\Phi(\mathbf{r}). \tag{1.43}$$

This is an algebraic equation rather than a differential one, and its solution for the particles density is:

$$n_{TF}(\mathbf{r}) = |\Phi(\mathbf{r})|^2 = \begin{cases} = \frac{\mu - V_{ext}(\mathbf{r})}{g} & \text{for } \mu > V_{ext}(\mathbf{r}) \\ = 0 & \text{for } \mu < V_{ext}(\mathbf{r}), \end{cases} \tag{1.44}$$

because the density of particles has to be a real number. In the case of an harmonic trapping potential for the condensate we obtain a parabolic density profile:

$$n_{TF} = \frac{\mu}{g}\left(1 - \frac{x^2}{R_x^2} - \frac{y^2}{R_y^2} - \frac{z^2}{R_z^2}\right), \tag{1.45}$$

where $R_i = \sqrt{2\mu/m\omega_i}$ is the Thomas-Fermi radius in the i direction. As already mentioned, the particles density is not null for $\mu > V_{ext}(\mathbf{r})$, and such condition in the case of harmonic trapping potential translates to $x < R_x$, $y < R_y$ and $z < R_z$. It is possible to write an expression of the Thomas-Fermi radius in dependence on only trap properties by calculating the chemical potential. It can be demonstrated that for an harmonic trap with dimension $a_0 = \sqrt{\hbar/m\omega_0}$, where ω_0 is the geometric mean of the trap frequencies, the chemical potential can be written as [16]:

$$\mu = \frac{\hbar\omega_0}{2}\left(\frac{15N_0a}{a_0}\right)^{\frac{2}{5}}, \tag{1.46}$$

where N_0 is the total number of particles and a the scattering length.

1.2.3 Excitation spectrum

To derive the excitation spectrum of a condensate, we need to take into account the first order perturbation $\delta\hat{\Psi}(\mathbf{r}, t)$, that we neglected in the calculation that leads to the Gross Pitaevskii equation. This can be done by diagonalizing the Hamiltonian of the condensate in the Bogoliubov approximation [16]. The result is that the system behaves as a collection of non-interacting bosons with an energy given by the Bogoliubov spectrum:

$$\epsilon(p) = \sqrt{\frac{p^2}{2m}\left(\frac{p^2}{2m} + 2gn\right)}, \tag{1.47}$$

where p is the momentum of the excitation and $n = |\phi(\mathbf{r})|^2$ is the particles density.

In the long wavelength limit, when $p^2 \ll 2mgn$, the dispersion relation reduces to a linear function of p:

$$\epsilon(p) \simeq cp, \tag{1.48}$$

where c is the speed of sound in the condensate, given by:

$$c = \sqrt{\frac{gn}{m}}. \tag{1.49}$$

Therefore, in the long wavelength limit excitations in the condensate are phonon-like.

On the other hand, in the short wavelength limit, when $p^2 \gg 2mgn$, the spectrum reduces to that of a free particle:

$$\epsilon(p) \simeq \frac{p^2}{2m}. \tag{1.50}$$

The transition from phonon to free particles excitation occurs when the wavelength of the excitation is $\sim \hbar/\sqrt{2mng}$. Such length scale is the so-called healing length ξ of the condensate, that denotes the shortest distance over which the wavefunction tends to its bulk value when subjected to a local perturbation. The healing length can be evaluated as the length scale at which the kinetic and the interaction energies are balanced [16]:

$$\frac{\hbar^2}{2m\xi^2} = ng, \tag{1.51}$$

that leads to the following expression:

$$\xi = \frac{1}{\sqrt{8\pi n a}}, \tag{1.52}$$

where a is the scattering length. Therefore, on length scales larger than ξ atoms are able to move collectively as phonons, while on shorter length scales they behaves as free particles. In particular, for ^{87}Rb the scattering length is about 100 a_0, where a_0 is the Bohr radius, so that the healing length for a condensate of ^{87}Rb atoms is about 200 nm.

1.3 Condensation and superfluidity

The word superfluidity is used to describe a variety of different phenomena [19]. The most common characteristic of a superfluid is its capability to flow without dissipation, that in the case of superconductors yields to a null resistance in the transport of an electric current. Another interesting property of superfluids is the manifestation of quantized vortices. Anyway, all the superfluid characteristics of a medium can be linked to the existence of a condensate, i.e. a single macroscopically occupied ground state. The superfluid motion can be interpreted as a collective phenomenon in which particles move together to preserve the macroscopic occupation of the ground state. Indeed, the description of the superfluid in term of a condensate leads to the dissipation-less flow and the existence of quantized vortices. In the following the Landau criterion for superfluidity is presented and then the nature of quantized vortex in a rotating superfluid is illustrated.

1.3.1 Landau criterion for superfluidity

The flow of a superfluid is observed to be dissipation-less as long as the velocity of the fluid is lower than a critical velocity v_c. The first explanation and evaluation of the critical velocity was performed by Landau [20], that established a criterion for the dissipation-less flow of a superfluid. To understand it, we consider a superfluid medium in motion with velocity $\mathbf{v}_s$. The only way for the condensate to lose energy is to create an excitation. We consider an energy spectrum for the excitation $\epsilon(p)$, that in the case of a condensate correspond to the Bogoliubov spectrum of Eq. (1.47). We suppose now that the superfluid is able to dissipate by creating an excitation with momentum $\mathbf{p}_e$ and thus energy $\epsilon(p_e)$. For the momentum conservation the momentum of the superfluid after the excitation creation is $\mathbf{p}_s - \mathbf{p}_e$, where $\mathbf{p}_s = m\mathbf{v}_s$ is the superfluid momentum before the excitation. We note that after the excitation emission the momentum of the fluid has to be lower than the initial one because only excitations that reduce the velocity cause a dissipation. We now consider the energy conservation in the process:

$$E(p_s) = E(p_s - p_e) + \epsilon(p_e) \tag{1.53}$$

where $E(p)$ is the energy of the superfluid in motion with momentum p. Considering for the superfluid only the contribution of the kinetic energy, then we obtain:

$$\frac{p_s^2}{2m} = \frac{(p_s - p_e)^2}{2m} + \epsilon(p). \tag{1.54}$$

Remembering that $p_s = mv_s$, the previous equation can be written in the form:

$$\mathbf{v}_s \cdot \mathbf{p}_e = \frac{p_e^2}{2m} + \epsilon(p_e). \tag{1.55}$$

The first term in the second member is always positive so we can say that $\mathbf{v}_s \cdot \mathbf{p}_e > \epsilon(p_e)$. The scalar product can be connected to the modulus of the two vectors considering that $\mathbf{v}_s \cdot \mathbf{p}_e = v_s p_e \cos(\theta) \leq v_s p_e$, where θ is the angle between the two vectors. Then, from the energy conservation we obtain:

$$v_s p_e > \epsilon(p_e) \implies v_s > \frac{\epsilon(p_e)}{p_e}. \tag{1.56}$$

Therefore the creation of an excitation in the superfluid can be performed only if the velocity of the superfluid exceeds the velocity of the excitation. The critical velocity is thus defined as:

$$v_c = \min_p \frac{\epsilon(p)}{p}. \tag{1.57}$$

For $v_s < v_c$ there is no mechanism to transfer energy from the superfluid to an excitation, so the superfluid flows without dissipation. Once the critical velocity is exceeded, the superfluid can lose energy by creating an excitation and the flow becomes viscous. Therefore, the Landau criterion asserts that a fluid can flow without dissipation, exhibiting thus a superfluid behavior, if the critical velocity defined as in Eq. (1.57) is non zero.

For a Bose-Einstein condensate the energy spectrum of excitations is the Bogoliubov spectrum. Therefore, the critical velocity corresponds to the sound velocity, as the lower energy excitations are phonon-like, with a linear dispersion $\epsilon(p) \simeq cp$. Due to its finite critical velocity, the condensate behaves like a superfluid. The typical speed of sound of an alkali condensate is of the order of mm/s. We note that the critical velocity of a condensate is finite because of the phonon-like dispersion. In the case of condensate of non interacting particles the spectrum reduces to that of a single particle and the critical velocity is null. Therefore, interparticles interactions are essential for the existence of superfluidity.

The concepts of condensation and superfluidity are thus fundamentally connected, as an interacting condensate exhibit a supefluid behavior. However, the Landau criterion is only a necessary, but not sufficient criterion for superfluidity. This is due to the fact that in many systems excitations at lower energy than phonons exist. Such excitations can be vortices, that lead to turbulence in the superfluid flow, or rotons in the spectrum of strongly interacting He II.

1.3.2 Quantized vortices

We demonstrated in the previous section that condensation and superfluidity are fundamentally connected, as condensates admit a dissipation-less flow for velocity lower than the speed of sound. We now use the condensate formalism, and in particular the GPE, to describe another key property of superfluids: the existence of quantized vortices.

From the condensate wavefunction we can define the current operator, in the usual form of quantum mechanic:

$$\mathbf{J}(\mathbf{r}) = \frac{\hbar}{2mi}\left(\Phi^*(\mathbf{r})\nabla\Phi(\mathbf{r}) - \Phi(\mathbf{r})\nabla\Phi^*(\mathbf{r})\right). \tag{1.58}$$

By expressing the condensate wavefunction as $\Phi(\mathbf{r}) = \sqrt{n(\mathbf{r})}\exp[i\phi(\mathbf{r})]$, where n is the density and ϕ the phase of the condensate, the current can be written as [16]:

$$\mathbf{J}(\mathbf{r}) = \frac{\hbar}{m} n(\mathbf{r})\nabla\phi(\mathbf{r}). \tag{1.59}$$

From such expression of the current, we then calculate the velocity of the condensate, so that $\mathbf{J} = n\mathbf{v}$. Therefore, we obtain:

$$\mathbf{v}(\mathbf{r}) = \frac{\hbar}{m}\nabla\phi(\mathbf{r}), \tag{1.60}$$

the velocity depends solely on the gradient of the condensate phase. From this it follows that the condensate velocity is irrotational, namely:

$$\nabla \times \mathbf{v} = 0. \tag{1.61}$$

The irrotationality of the condensate motion leads to the quantization of circulation. Indeed, around a closed path we find that the circulation Γ is:

$$\Gamma = \oint \mathbf{v}\cdot d\mathbf{l} = \frac{\hbar}{m}\oint \nabla\phi \cdot d\mathbf{l} = \frac{\hbar}{m}\Delta\phi, \tag{1.62}$$

where $\Delta\phi$ is the phase variation along the closed line. For the condensate wavefunction to be single-valued, $\Delta\phi$ has to be multiple of 2π, so the circulation become:

$$\Gamma = \frac{\hbar}{m} 2\pi l, \tag{1.63}$$

where l is an integer number: the circulation is quantized. Such state is characterized by a phase singularity and can exist only in a multiply-connected geometry, where the condensate density vanishes at this phase singularity. A multiply-connected geometry can be both created by an external trapping potential and by the formation of a vortex, a line of zero density about which the condensate phase winds. Indeed, the phase singularity determines also a singularity in the density. To prove that, we consider a condensate in purely azimuthal flow in a system with rotational symmetry respect to

the z axis. The velocity at distance r from the trap axis can be calculated using the definition of the circulation, that leads to [16]:

$$v(r) = \frac{\hbar}{mr} l. \tag{1.64}$$

At the same time, the phase of the condensate must vary as $e^{il\theta}$ around the trap axis, where θ is the azimuthal angle. For the kinetic energy of the condensate to remain finite, the density has to vanish along the axis of the trap, such that the phase is no longer well-defined and similarly the velocity of the condensate. Therefore, when a condensate is forced to rotate, it creates quantized vortices, as observed in several experiments [12] [11] [10].

To find whether such vortices form, we first calculate the energy per unit length of a single vortex of charge l and radius R in a uniform condensate of density n. As a first approximation, it can be calculated as the integral of the kinetic energy associated with the flow along a closed path [16]:

$$E = \frac{nm}{2} \int_0^{2\pi} \int_0^R v_s^2 r dr d\theta = \frac{\pi N}{m} l^2 \hbar^2 \int_0^R \frac{dr}{r}, \tag{1.65}$$

where we have used Eq. (1.64) for the velocity of the superfluid v_s. The previous integral diverges for $r = 0$, so a cutoff r_c has to be introduced. In this way we obtain:

$$E = \frac{\pi n}{m} l^2 \hbar^2 \log\left(\frac{R}{r_c}\right). \tag{1.66}$$

Typically the cutoff r_c is taken to be equal to the healing length ξ of the condensate. In principle, also the potential energy due to the density profile of the vortex should be included, but such terms can be shown to be small and its contribution is included in the uncertainty of r_c. Therefore, the energy of a vortex scales as l^2, so the lowest energy configuration for a multiply charged vortex is to break up into an array of l single charged vortices. In particular, vortices will form an hexagonal array to maximize their separation and minimize the total energy [10].

From the expression of the energy of a vortex, we can see that also the rotational flow admit a critical angular velocity, below which the system remain at rest because it does not have enough energy to create a vortex. In particular, it can be demonstrated that the critical angular velocity is:

$$\Omega_c = \frac{\hbar}{\mu R^2} \log\left(\frac{R}{\xi}\right). \tag{1.67}$$

When the angular velocity imprinted on the condensate exceeded Ω_c, it is energetically favourable for the condensate to rotate and form vortices.

1.4 Optical potentials for atomic superfluids

One of the most attractive properties of atomic superfluids is the possibility to change their confinement in an optical way. The interaction of light with atoms has indeed

two main contributes: one linked to absorption of photons that leads to a dissipative force, and one due to the dispersive behavior of atoms that originates a conservative dipole force. The latter opens the possibility to create arbitrary potentials for atoms by shaping the spatial intensity profile of a laser beam. The nature of the radiative forces that light acts on an atomic system is illustrated in Sec. 1.4.1, with a particular attention to the optical dipole force that allows to create optical potentials. Then in Sec. 1.4 two interesting applications for an atomic superfluid are presented: a ring shaped potential to study persistent current, and a disorder potential to investigate the superfluid-to-insulator transition.

1.4.1 Radiative forces

In a semiclassical approach, the atom-light interaction can be interpreted as a force acting on the atom, once the momentum conservation is considered [21] [22]. When a photon is absorbed or emitted, the atom recoils and thus changes its momentum state. Such momentum exchange can be seen as a radiative force that light exerts on the atom. In particular, there are two kinds of radiative forces, associated with the absorptive and dispersive properties of interaction: the dissipative radiation pressure force, and the conservative optical dipole force. The radiation pressure is associated with the transfer of momentum from light to atoms in a resonant scattering process: atoms absorb photons from an incident light beam and change both their internal state in the excited one and their momentum by the photon momentum $\hbar\mathbf{k}$, where $\mathbf{k}$ is the wave vector of the absorbed photon. From the excited state they then decay spontaneously to the ground state, emitting fluorescent photons in random directions. The average change in momentum due to the spontaneous emission is thus null, so that the dissipative force corresponds to an average momentum transfer of $\hbar\mathbf{k}$ per atom in each absorption/emission cycle. The radiation pressure force is the basis of the most common laser-cooling techniques. Instead, the optical dipole force is conservative, and arises from the dispersive behaviour of atoms. In particular, it originates from the interaction between the external electric field and the induced atomic electric dipole. Thanks to the optical dipole force it is possible to create optical traps for atoms.

Now we describe the two forces in detail, considering the case of an atom in interaction with an incoming laser beam at frequency ω.

Radiation pressure force

As already mentioned, the radiation pressure arises from the absorption of photons. If N_{ph} photons are absorbed in a time Δt, the radiation pressure can be written as:

$$\mathbf{F} = \hbar\mathbf{k}\frac{N_{ph}}{\Delta t}, \tag{1.68}$$

where $\hbar\mathbf{k}$ is the momentum carried by each absorbed photon. It is possible to evaluate $N_{ph}/\Delta t$ from the theory of interaction between coherent radiation and a two-level atom

and demonstrate that the radiation pressure is [21]:

$$\mathbf{F} = \hbar\mathbf{k}\frac{\gamma}{2}\frac{s}{1+s+\frac{4\delta^2}{\gamma^2}}, \tag{1.69}$$

where γ is the natural linewidth of the transition, $\delta = \omega - \omega_0$ is the detuning between the laser frequency ω and the resonance frequency ω_0 and $s = I/I_{sat}$ is the saturation parameter defined as the ratio between the the intensity I of the laser and the atomic saturation intensity I_{sat}. We note that the force has the same direction of the incoming light beam, that defines the direction of the wave vector $\mathbf{k}$. Moreover, the radiation pressure is maximum at resonance when $\delta = 0$ and scales as I/δ^2 out of resonance. In particular, looking at the intensity dependence, we see that for strong fields the force saturates to the limiting value of $\mathbf{F} = \hbar\mathbf{k}\gamma/2$ when $s \gg 1$. In this case, the atom is continuously absorbing and re-emitting photons at the maximum rate $\gamma/2$, limited only by the lifetime $1/\gamma$ of the excited state.

For typical atomic velocities, the momentum exchange from the absorption of a single photon is small compared to the momentum of atom, which justify the classical treatment of the motion variables. In particular, for ^{87}Rb at room temperature the mean velocity of the atom is $v_T = \sqrt{3k_BT/m} \simeq 300$ m/s, while the velocity change induced by a single photon at resonant wavelength $\lambda = 780$ nm is $v_R = \hbar k/m \simeq 6$ mm/s. The recoil velocity is about 10^4 times smaller than the atomic velocity, but still the radiation pressure force experienced by atoms can be quite intense if the number of absorbed photons is large. Therefore, using radiation pressure of resonant light, it is possible to decelerate atoms and cool them.

Optical dipole force

Unlike the radiation pressure, the optical dipole force is conservative, so it can be derived from a potential, the minima of which can be used for atom trapping. It arises from the fact that, when an atom is placed into laser light, the electric field $\mathbf{E}$ induces an atomic dipole moment $\mathbf{p}$ that oscillates at the driving frequency ω. In a classical model of the atom, the dipole moment arises from the periodic displacement of the atomic electron, that is forced to oscillate by the external electric field. In a quantum mechanical approach, the dipole moment arises from the mixing of the ground and excited states, that have different charge distributions. In particular, if we consider an electric field with amplitude $E(\mathbf{r})$, the amplitude of the induced dipole can be expressed in terms of the atomic polarizability α:

$$p(\mathbf{r}) = \alpha E(\mathbf{r}). \tag{1.70}$$

We note that such proportionality between $p(\mathbf{r})$ and $E(\mathbf{r})$ is valid only in the linear regime of weak excitations, when the saturation of the two-level system is negligible and α does not depend on E.

The analytic expression of the atomic polarizability can be derived from a theoret-

ical model of atom-light interactions [21]:

$$\alpha = -\frac{e^2\mu_{eg}^2}{\hbar}\frac{\delta - i\frac{\gamma}{2}}{\delta^2 + \frac{\gamma^2}{4} + \frac{\Omega}{2}}, \tag{1.71}$$

where e is the electronic charge, μ_{eg} is the transition dipole moment and Ω is the Rabi frequency. The atomic polarizability is a complex quantity: the real part, representing the dipole component oscillating in phase with the electric field, is responsible of the dispersive properties of interaction, while the imaginary part, describing the out-of-phase component of the dipole, is connected with the absorption. In particular, the two components have different dependence on the detuning δ: at the resonance $\delta = 0$ the real part is null and the imaginary is maximum, while out of resonance the real part scales as $1/\delta$ and the imaginary decays faster as $1/\delta^2$. Therefore, if we consider an incoming laser beam far of resonance, the only contribution to the polarizability will be from its real part, so the medium becomes purely dispersive. In this case, the induced dipole interacts with the radiation electric field and we can define the optical dipole potential as the potential energy of such interaction:

$$U_{dip}(\mathbf{r}) = -\frac{1}{2}\langle \mathbf{p}\cdot\mathbf{E}\rangle = -\frac{1}{2\epsilon_0 c}\mathrm{Re}(\alpha)I(\mathbf{r}), \tag{1.72}$$

where ϵ_0 is the electric constant, c the speed of light and $I(\mathbf{r})$ the intensity of the laser beam. The dipole force can be now calculated as the gradient of the potential energy.

From the obtained expression of U_{dip} we see that if we create a spatial modulation of the intensity $I(\mathbf{r})$, the atoms will feel a potential energy that is proportional to such intensity modulation. In particular, we can trap atoms in intensity maxima or minima in dependance of the sign of the detuning. Indeed, if we explicit the expression of $\mathrm{Re}(\alpha)$ we get [23]:

$$U_{dip}(\mathbf{r}) = \frac{3\pi c^2}{2\omega_0^3}\left(\frac{\gamma}{\delta}\right)I(\mathbf{r}). \tag{1.73}$$

If the light is red-detuned ($\delta < 0$) the dipole potential is negative, hence maxima of the intensity correspond to minima of the potential, whereas in the case of blue-detuned light ($\delta > 0$) the dipole potential is positive and maxima of the intensity correspond to maxima of the potential. Therefore, for red-detuning we can trap atoms in regions of high-field intensity, while for blue-detuning the atoms are trapped where the intensity has its minima.

So far, we neglected the imaginary part of the absorption coefficient, but it plays a fundamental role in determining the lifetime of an atomic gas inside an optical trap. As already mentioned, it is associated with the absorption of photons from the incident light field, so it generally determines a heating of the trapped sample. This process can be quantified by the average number of photons scattered in the unit of time in cycles of absorption and spontaneous emission [23]:

$$\Gamma_{sc}(\mathbf{r}) = \frac{1}{\hbar\epsilon_0 c}\mathrm{Im}(\alpha)I(\mathbf{r}) = \frac{3\pi c^2}{2\hbar\omega_0^3}\left(\frac{\gamma}{\delta}\right)^2 I(\mathbf{r}). \tag{1.74}$$

We see that the photon scattering rate scales as $1/\delta^2$. Although far of resonance the dispersive behavior dominates over the dissipative process, the finite value of Γ_{sc} sets the limit of the lifetime in an optical trap.

1.4.2 Probing superfluidity with optical potentials

The control over the spatial intensity distribution of a laser beam permits to create any desired potential for the atomic population. In this section, two different kinds of optical potentials useful to study the superfluid behavior of a condensate are presented. First, the possibility to study persistent current in a ring geometry is illustrated. The multiply-connection of such potential is particularly suited to this kind of study because it prevents the instability due to vortex motion in a rotating superfluid. Then, the role of disorder is examined: in general it corresponds to a localization effect of the wavefunction of the components of a system, that in the case of a supefluid may lead to a superfluid-to-insulator transition.

Persistent current in a toroidal trap

A persistent current is a perpetual flow of particles, that may determine an electrical current if they are charged, without requiring an external power source. Persistent currents have been observed both in superfluid and superconducting systems, as the response of the system under rotation or external magnetic field respectively. As described in [24], a persistent current can be observed in liquid helium superfluid in an annular geometry. In particular, an observation of persistent current can be performed as follows: above the critical temperature of superfluid transition, the annular container is set into a rapid rotation, so that the fluid inside is forced to rotate because of its viscosity. Then the temperature is decreased below the critical value for the superfluid transition and the container rotation is stopped. The superfluid liquid helium continues to rotate indefinitely because now its flow is dissipation-less, forming a persistent mass current. In particular, the persistent current is observed as long as the velocity of the fluid inside the container is below the critical velocity. For a stationary container, the rotating state of the superfluid cannot be the stationary state, so the persistent current is an example of an extremely long-lived metastable state.

As already mentioned, such state can be observed also in superconductors in a similar annular geometry, but now the persistent current is induced by an external magnetic field. When the system is above the critical temperature of the superconducting transition, an external magnetic field is applied along the axis of symmetry, then the material is cooled down below the critical temperature and the external field removed. In this case, a surface persistent current is induced in the material, generating a magnetic field such that the flux penetrating the sample remains unchanged.

The stability of persistent currents and their properties can be studied with a Bose-Einstein condensate in a ring geometry. To study persistent current, such geometry is preferable to a simply-connected one, as an usual harmonic trap, because in a rotating superfluid the creation of vortices is unavoidable. Vortices are unstable and are

observed to move inside the superfluid towards region of lower density, reducing the angular momentum of the system [11] [10]. To avoid vortex instability, a multiply-connected geometry can be used, as a ring trap. In this case, vortices are pinned at the center of the ring where the density is null [25] and superfluid flow may be stable as long as the angular velocity at which the condensate circulates around the ring is lower than the critical angular frequency for excitations of the condensate.

Several schemes have been implemented to create a ring trap, using both magnetic and optical confinement. The disadvantage of a magnetic trap is that in the zero magnetic field regions the Majorana spin-flip causes critical losses of atoms. On the other hand, optical traps are easy to create, as discussed in the previous section, and the desired geometry can be obtained by using a laser beam with a ring-shaped intensity spatial profile. To do that, Laguerre-Gauss beams [26] [27] can be used or spatial light modulators, as in this work, in combination with other trap to create a total confinement for the atomic population.

Using optical ring trap, it has been possible to observe persistent currents in a condensate with lifetime up to a minute [26], and to investigate their dependency on the temperature [28] and spin imbalance in the case of a mixture of condensate of the same element in two different spin states [29]. The study of a condensate in a ring trap finds application also in atom interferometry, where a ring-shaped condensate is used to measure rotations thanks to the Sagnac effect [30] [31], and in atomtronics, the field of research that focuses on the creation of atoms analog to electronic materials, devices and circuits. In this framework, a ring-shaped condensate can be used to create the analog of a Superconducting Quantum Interference Device (SQUID), a very sensitive magnetometer used to measure extremely subtle magnetic fields, based on superconducting loops containing Josephson junctions. To do that, in [32] a toroidal condensate was created and forced to rotate with a Laguerre-Gauss beam, and a weak link emulating a Josephson junction was introduced via a repulsive optical potential.

Disordered superfluids

The effect of disorder in a quantum system was firstly investigated by Anderson, that in 1958 found out that the presence of disorder in a crystal lattice has a dramatic consequence on the electronic transport properties, and in particular that it can turn metallic materials into insulators [33]. Such effect is due to interference: the multiple scattering of a single electron by randomly distributed defects causes a destructive interference on its wavefunction, that localizes the electron on a finite region of space. In particular, Anderson identified the existence of a critical condition for localization that depends on the amount of disorder and on the electronic configuration. Such phenomenon has been called Anderson Localization (AL) after his studies and regards not only the transport of electric current in metallic materials, but also the propagation of any kind of wave in a disordered medium.

In general, in a disordered medium three typical energy-dependent length scales can be used to characterize the three basic effects induced by disorder [34]. Single

scattering from impurities defines the scattering mean free path $l_s = v\tau_s$, where v is the velocity of the wave and τ_s the mean time between two consecutive scattering events. The mean free path characterizes the typical length traveled by the wave before it loses the memory of its initial state, and mostly the memory of its initial phase. Such length scale depends of the particular scattering process between the wave and impurities. Multiple scattering defines instead the Boltzmann mean free path l_B, that corresponds to the length traveled by the wave before it loses the memory of its initial direction. In general, several scattering events are requested to modify significantly the trajectory of the wave, so typically $l_B > l_s$. The Boltzmann scale defines the distance within whom the transport crosses over from ballistic to diffusive. And it is the diffusive nature of transport that gives rise to the localization effect of disorder. Indeed, due to the stochastic nature of diffusion, the wave has a non-null probability to return back to its initial position via loop paths and interference effects have to be considered. Each loop consists in a multiple scattering path and can be traveled in both direction, but the phase accumulated in one loop is the same. This generates a constructive interference of the matter wave because the two paths are in phase, and the probability to return in the initial position is enhanced. In this case, the effect of disorder induces coherent back scattering and a weak localization that reduces the diffusion coefficient. When the disorder is strong enough, such interference effect completely cancels the diffusion coefficient and the system enter in a regime of strong, or Anderson, localization. Here, the probability distribution of the wave decays exponentially in space and the characteristic length of such decay is the so-called localization length L_{loc}. Such length scale can be connected to the Boltzmann mean free path in the limit of high momentum scattering $kl_B \gg 1$ [35]:

$$L_{loc} = l_B \exp\left[\frac{\pi}{2} k l_B\right]. \tag{1.75}$$

The above picture of the localization effect of disorder tells us that the strength of localization depends on two characteristics of the medium: the coherence of the multiple-scattering path, governed by the interference parameter kl_B, and the dimensionality of space, that determines the return probability. In particular, in lower dimensions the probability for the wave to return in its initial position is higher, and Anderson localization occurs for any small amount of disorder.

When disorder is added in a superfluid system, the localization effect it produces can determine a superfluid-to-insulator transition. This is particularly evident in two-dimensional systems, as here any little amount of disorder is sufficient to localize the wavefunctions of the components. Such transition has been studied mainly in thin films of disordered superconductors [36] [37], leading to different insulator state in dependance on the strength of disorder [38]. In the presence of weak disorder the superconductor is divided into several regions of superfluid surrounded by walls of insulating material. Different regions can be connected by coherent tunneling of particles as in the Josephson effect, so the order parameter of the superfluid is not destroyed. For stronger disorder, the wavefunction of the superfluid components becomes localized and a superfluid phase can no longer exist.

The effect of disorder in a superfluid or superconducting material can be studied using atomic superfluids to mimic the behavior of solid state physics. Quantum gases indeed offer a versatile system in which disorder can be introduced in a controlled manner. In particular, in an atomic system, disorder can be realized in several way: with disordered optical potentials, with quasi-random potentials of bicromatic optical lattices, or with a second atomic specie or spin state as impurities. In [39] a bicromatic optical lattice was used to probe the Anderson localization of a condensate in one dimension, while in [40] a speckles optical potential was implemented for the same purpose. As it will be illustrated in detail in Sec. 4.2, a speckles pattern consists in a granular distribution of intensity, that can be obtained using a glass with rough surface. In a three dimensional system, Anderson localization has been observed using speckles optical potentials [41] [42], but in two dimension Anderson localization is more elusive. Indeed, speckles potentials cause classical trapping of atoms: speckles form potential landscapes that constrain atomic motion, that results thus localized, but not because of Anderson localization. To avoid such problem, a different kind of disordered light pattern can be used: the point-like disorder, characterized by a random distribution of spots of light surrounded by regions of darkness. Such kind of disorder can be set not to cause any classical trapping of atoms [43], which makes it preferable to a speckles pattern. Moreover, point-like is a perfect candidate to mimic the random presence of impurities inside a solid state superconductor.

Chapter 2

Magneto optical trapping of ^{87}Rb

Part of my master thesis work has been dedicated to the construction and optimization of a magneto optical trap (MOT) for ^{87}Rb atoms. In particular, I took part in the alignment of the optical system and work at the optimization of the efficiency of the 2D and 3D MOT in Lab. 29 of Dipartimento di Fisica e Astronomia in Florence. My thesis work represent the initial part of the construction of a novel experiment for a Bose-Bose mixture of ^{87}Rb and ^{39}K to study two-components superfluidity. This Chapter is organized as follows: in Sec. 2.1 I present the working principle of the magneto optical trap and investigate the possibility to create a beam of collimated atoms with a 2D MOT scheme. In Sec. 2.2 I present the experimental setup used for this master thesis work: I discuss ^{87}Rb properties and the experimental system used to create a MOT for such atom. Finally, in Sec. 2.3 I illustrate the measuring techniques used to probe the atomic population in the MOT and report the measurement preformed for the optimization of the loading efficiency of the 3D MOT.

2.1 The Magneto Optical Trap

The magneto-optical trap (MOT) is a robust experimental technique, that allows to both trap and cool atoms for arbitrarily long time. Trapping times can be as long as several minutes, limited only by losses of atoms due to collisions with the background gas. For this reason a vacuum chamber evacuated down to the ultra-high vacuum regime ($< 10^{-9}$ mbar) is required in order to keep the cold atoms well isolated from the environment.

A MOT is composed by the combination of the laser cooling technique of optical molasses and a magnetic gradient. Optical molasses are realized with two counter-propagating laser beams with the same frequency ω, smaller than the atomic resonance frequency ω_0, that act on the atomic population as a viscous force. The viscosity of optical molasses is due to the Doppler effect: an atom with velocity $\mathbf{v}$ sees photons of the two beams with different frequencies. In particular, if we consider the velocity of the atom parallel to the direction of propagation of the two laser beams for simplicity, than in the reference frame of the atom the frequency of the laser beam propagating in the opposite direction of the atom is upshifted $\omega' = \omega(1 + v/c)$, where v is the

modulus of the atomic velocity, while the frequency of the beam propagating in the same direction of the atom is downshifted $\omega'' = \omega(1 - v/c)$. As $\omega < \omega_0$, the frequency ω' is closer to the resonance than ω'', so that the atom will preferably absorb photons from the beam propagating in the opposite direction, reducing thus its velocity due to the recoil.

The decelerating force due to an optical molasses can be obtained quantitatively starting from the radiation pressure force described in 1.4.1. In the small intensity limit $I \ll I_{sat}$, the total force acting on the atom in an optical molasses can be written simply as the sum of the radiation pressure forces exerted by the two beams separately. Including the Doppler shift in Eq. (1.69), we get [22]:

$$\mathbf{F} \simeq \hbar\mathbf{k}\frac{\gamma}{2}\left[\frac{s}{1+\frac{4(\omega-\omega_0-kv)^2}{\gamma^2}} - \frac{s}{1+\frac{4(\omega-\omega_0+kv)^2}{\gamma^2}}\right], \tag{2.1}$$

where $s = I/I_{sat}$ is the saturation ratio. The first term in square parentheses is due to the co-propagating laser beam, and the second to the counter-propagating one. With a small velocity expansion we obtain:

$$F = -\beta v + O(v^3), \tag{2.2}$$

where β is the damping coefficient:

$$\beta = -8\hbar k^2 s \frac{\frac{\delta}{\gamma}}{\left(1+\frac{4\delta^2}{\gamma^2}\right)^2}. \tag{2.3}$$

Therefore, the force acting on atoms in an optical molasses is viscous, and permits to slow down exponentially the atoms to vanishing velocity. We note that such force derives from two conservation principles: momentum conservation, resulting in the presence of the radiation pressure force, and the energy conservation, that lead to the preferential absorption of the counter-propagating beam.

Optical molasses provide a very efficient method to cool atomic gases, but they do not produce any spatial confinement. For this reason in a MOT we add an inhomogeneous magnetic field to an optical molasses, to create a trapping force able to spatially confine the atomic population. The magnetic field is generated by a pair of coils in a anti-Helmholtz configuration, namely with currents circulating in opposite directions. To understand the working principle of a MOT we consider a simplified 1D version, composed by the two counter-propagating laser beams with opposite circular polarization for the optical molasses and the pair of anti-Helmholtz coils. The latter provides a magnetic field $\mathbf{B}(x) = bx\hat{x}$, with uniform field gradient in the trap-centre $x = 0$. For simplicity, we consider an atom with a ground state with angular momentum $J = 0$ and an excited state with $J = 1$. The energy levels of the excited state are modified by the Zeeman shift:

$$\Delta E(x) = g_{J'}\mu_B m_{J'} bx, \tag{2.4}$$

where $g_{J'}$ is the Landé factor of the excited state, $\mu_B = e\hbar/2m_e$ is the Bohr magneton, and the magnetic field gradient is chosen in such a way that $g_{J'}b > 0$. In Fig. 2.1

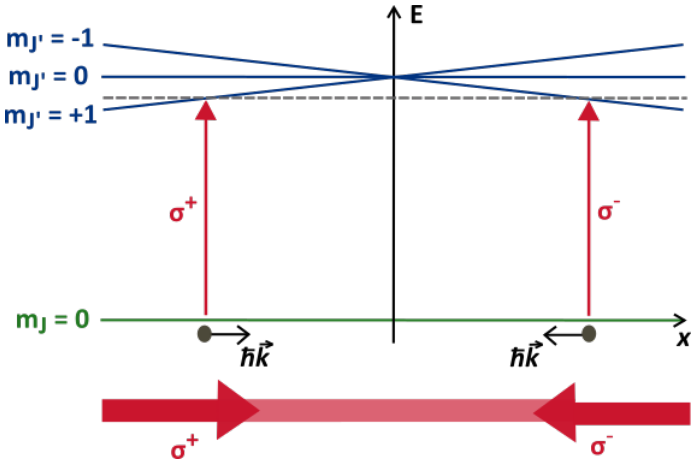

Figure 2.1: Illustration of the working principle of a MOT in a simplified 1D scheme: the energy levels of the excited state are modified by the presence of the external magnetic field, such that for an atom in $x > 0$ the transition to the $m_{J'} = -1$ state is favoured. Because of the momentum conservation, the transition can happen only if a σ^- polarized photon is absorbed, so the atom receive an $\hbar\mathbf{k}$ momentum kick in the trap center direction. Vice versa an atom in $x < 0$ will absorb preferably a photon from the σ^+ polarized beam, that push it in the trap centre direction.

an illustration of the working principle of a MOT is presented. The presence of the magnetic field introduces a position-dependence in the global force acting on the atoms. An atom in $x > 0$ preferentially absorbs a photon from the σ^- polarized beam, because of the selection rules: with the red-detuned laser beam of the optical molasses the transition $m_J = 0 \to m_{J'} = -1$ is closer to the resonance and to perform it a photon with polarization σ^- has to be absorbed. The recoil due to the absorption pushes the atom in the trap center direction. Vice versa for an atom in $x < 0$: the transition $m_J = 0 \to m_{J'} = +1$ now is closer to the resonance so a σ^+ photon will be absorbed, and again the recoil will push the atom to the trap center. More formally, the force acting on the atom in the presence of the optical molasses and the magnetic field can be calculated from Eq. (1.69), taking into account the Doppler and the Zeeman shifts [22]:

$$\mathbf{F} \simeq \hbar\mathbf{k}\frac{\gamma}{2}\left[\frac{s}{1+\frac{4(\omega-\omega_0-kv-g_{J'}\mu_B m_{J'}bx)^2}{\gamma^2}} - \frac{s}{1+\frac{4(\omega-\omega_0+kv+g_{J'}\mu_B m_{J'}bx)^2}{\gamma^2}}\right] \tag{2.5}$$

Expanding such expression in the limit of small velocity and small displacement, we get:

$$F \simeq -m\omega^2 x - \beta v, \tag{2.6}$$

which describes the force acting on a damped harmonic oscillator. Therefore, in a MOT the force acting on atoms has two contribution: an elastic term $-m\omega^2 x$, provided by the magnetic field, and a damping term $-\beta v$, provided by the optical molasses. The elastic term supplies the trap for the atoms, while the damping one cools them. This results can be extended to atoms with different electronic configurations and in higher dimensions. In particular, we can obtain a total confinement of the atomic

population with three pairs of counter-propagating beams in three orthogonal directions intersecting in the region of zero magnetic field of the anti-Helmholtz coils. Also in this case the polarization of the beams has to be circular and opposite for the couple of beams counter-propagating in the same direction.

Finally, it is interesting to determine the lower temperature that can be achieved in a MOT. Such limit arises from the heating effects due to the spontaneous emission that results in a recoil kick in a random direction, and to the intensity fluctuations of the laser beam. It can be demonstrated [44] that the lower temperature that can be reached in a MOT is the so-called Doppler temperature:

$$T_D = \frac{\hbar\gamma}{4k_B}\frac{1+\left(\frac{2\delta}{\gamma}\right)^2}{\frac{2|\delta|}{\gamma}}, \tag{2.7}$$

which takes its minimum value for $|\delta| = \gamma/2$:

$$T_D^{min} = \frac{\hbar\gamma}{2k_B}, \tag{2.8}$$

that depends only on the linewidth γ of the transition. For ^{87}Rb atoms $\gamma = 2\pi \times 6$ MHz, so the minimum Doppler temperature is $T_D^{min} \simeq 150$ μK.

2.1.1 2D MOT

A 3D MOT is the starting point for all the cold atoms experiments, as it provides a large number of atoms, $N \simeq 10^9$, at a temperature of few tens of μK. However, even if it is possible to create a 3D MOT directly from a vapour cell source of atoms (VCMOT) [45], usual 3D MOTs are preceded by a first stage of cooling. Indeed, in a VCMOT the lifetime of atoms loaded in a different trap after the MOT cooling is limited by collisions with the background thermal gas. Therefore, the most common configuration to produce cold atoms is a dual chamber system: in a first vacuum chamber atoms are extracted from a vapour cell or an oven and preliminarily slowed and cooled down to create an atomic beam. Such beam transfers atoms in a second chamber with ultra-high vacuum where the 3D MOT cooling stage is performed. Here the collisions with the background gas are negligible, so that a long lifetime for the atomic traps can be achieved.

There are two main way to create a beam of atoms to load the 3D MOT: by slowing down atoms with a Zeeman slower, or by cooling them with a 2D MOT. A Zeeman slower uses the radiation pressure force to decelerate an atomic beam, typically exiting from a oven, and a magnetic field to compensate the Doppler effect and keep the atoms in resonance with the cooling light for all the trajectory to the 3D MOT. The Zeeman slower technique displays some disadvantages: a great engineering effort to design and construct the system is required, and the atomic beam created exhibits a divergence that reduces the loading efficiency of the MOT.

On the other hand, a 2D MOT uses the magneto-optical trapping technique illustrated in the previous section to create a collimated beam of atoms. With such tech-

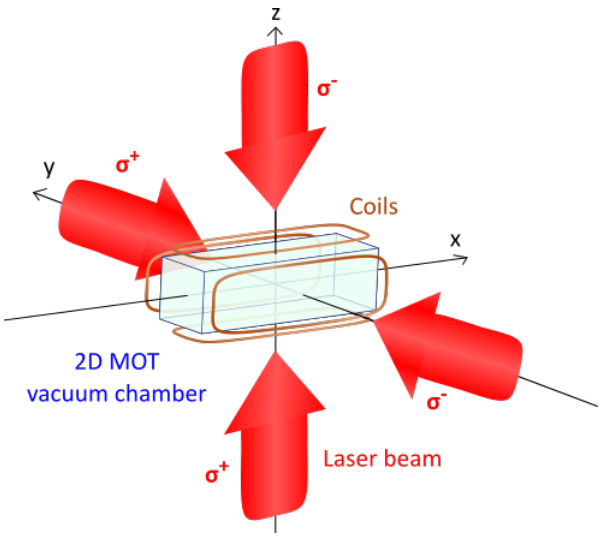

Figure 2.2: Illustration of the working principle of a 2D MOT: two couples of laser beams with opposite circular polarization create an optical molasses in the radial direction, while the two pairs of coils create the elastic confinement.

nique, atoms are trapped and cooled in two dimensions using two couples of counter-propagating beams with opposite circular polarization and two sets of coils to generate the desired inhomogeneous magnetic field, as shown in Fig. 2.2. The coils are used in a Ioffe configuration to produce a cylindrical quadrupole field with a line of zero field in the x direction. As the atoms are free to move in the x direction the 2D MOT produces a beam of atoms moving in such direction, that is extremely collimated thanks to the radial cooling of the atomic population. A 2D MOT can be used as a first stage of cooling both if the atoms are extracted from a vapour cell or from a oven, although their escaping velocity are very different. In particular, if atoms come from an effusive oven, the 2D MOT can be load both by a longitudinal and a transverse beam of atoms [46].

Several configuration of 2D MOT has been probed to produce an atomic beam. The simplest one is by using the 2D MOT setup of two couple of counter-propagating laser beams and the Ioffe coils [47]. In such scheme the radial cooling compresses atoms in correspondence of the x axis, while the x component of their velocity is not changed. Therefore, two different beams of atoms are created, propagating in opposite direction along the x axis. With this technique, it is possible to obtain a flux of $\sim 10^{10}$ atoms/s with a velocity distribution centered around $\sim$ 50 m/s [47]. This technique has the disadvantage that half the cooled atoms are moving in the opposite direction of the 3D MOT, and are thus not used for its loading. This problem can be overcome by adding a launching technique that creates an atomic beam only in direction of the 3D MOT.

In the $2D^+$ MOT scheme [48] an unbalanced optical molasses in the x direction is added to reduce the velocity of the atoms in the x direction and to launch them towards the 3D MOT chamber. To do that, an extra pair of counter-propagating laser beams can be introduced in the x direction to create the optical molasses. The intensity in these two beams can be set independently, so that atoms are pushed in the direction

of the most intense laser beam. In this way, atoms with a large velocity in the x direction are slowed down by the optical molasses, so that they can be captured by the subsequent 3D MOT stage. In particular, with such scheme it is possible to obtain a flux of $\sim 10^9$ atom/s at a mean velocity of 8 m/s [48].

Other kinds of launching technique can be used, like an external magnetic field [49], that has the disadvantage to create a large velocity distribution in the atomic beam, or a pushing laser beam [50]. In the latter case, the frequency of the pushing beam can be optimized to obtain an efficient loading of the 3D MOT. In [50], a two-color pushing beam propagating along the $+x$ direction is added to the 2D MOT scheme, formed by the composition of a blue and a red detuned light. The blue-detuned light interact mostly with the atoms moving in the $+x$ direction, accelerating them and reducing the losses in the transfer from the 2D to the 3D MOT. The red-detuned light interacts preferably with atoms moving in the $-x$ direction and it is used to avoid their loss from the 2D MOT and to turn their direction to the $+x$, so that they can be captured by the 3D MOT too.

2.2 Experimental setup

In this section I illustrate the experimental setup used to create the magneto optical trap of ^{87}Rb atoms. In particular, in Sec. 2.2.1 the main properties of ^{87}Rb are reported and the laser system used to cool down the atomic population is presented. In Sec. 2.2.2, I illustrate the vacuum system created for the experiment and the optical system we aligned for the realization of the 2D MOT and 3D MOT of ^{87}Rb atoms.

2.2.1 Rubidium-87 and laser sources

Rubidium-87 is an alkali atom, characterized by the energy level structure in Fig. 2.3. The fine structure of the atom gives rise to two different spectroscopy lines, the D_1 and D_2 lines. For the laser cooling of rubidium the D_2 line with wavelength 780 nm is used. Among all the possible hyperfine levels of the ground $^2S_{1/2}$ state and the excited $2P_{3/2}$ state, the cooling is performed with the transition $F = 2 \rightarrow F' = 3$. This is a closed transition: an atom excited in $F' = 3$ can decay only in $F = 2$ because of the selection rule $|\Delta F| \leq 1$. In this way, an atom can perform as many absorption/emission cycle as requested to be cooled down to the limit of Doppler laser cooling. However, because of the small energy separation between the states $F' = 2$ and $F' = 3$, there is a probability for the cooler laser to excite the $F' = 2$ state. From here atoms can decay to the $F = 1$ ground state, so that they are lost for the cooling procedure. For this reason a repumping laser is needed to bring the atoms decayed in $F = 1$ back to $F = 2$.

In our experimental setup, two different laser sources are used to create the cooler and the repumper light. For the cooler a diode laser in an extended Toptica DLPRO100 cavity is used. The repumper light is instead generated by a distributed feedback (DFB) diode laser Toptica DFBRO100. For the cooler, the extended cavity permits to fine

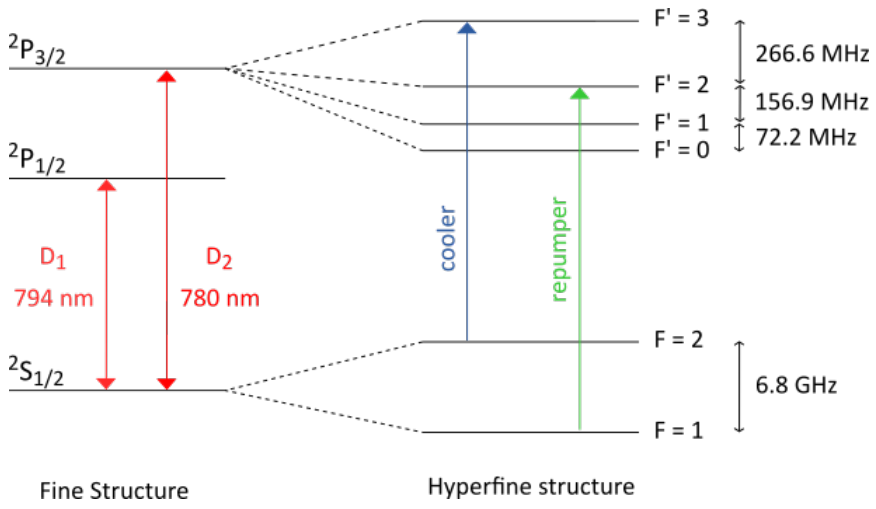

Figure 2.3: Energy levels of ^{87}Rb.

tune the laser frequency by modifying the length of the cavity using a piezoelectric element. In addition, for both lasers it is also possible to tune the frequency by varying the electric current flowing in the diode and its temperature.

The frequency of the cooler is stabilized to the atomic resonance using the modulation transfer spectroscopy technique [51]. This is a pump-probe technique which produces sub-Doppler lineshapes, that can be directly used for laser locking. Modulation transfer spectroscopy is a variation of the frequency modulation spectroscopy where the modulation is imposed to the pump beam instead of the probe one. In frequency modulation spectroscopy [52] the probe beam is passed through an Electro-Optical Modulator (EOM), driven at a radio-frequency ω_m, that introduces a time-dependant phase modulation in the beam. The light emerging from the EOM can be represented in terms of a carrier at frequency ω_L and sidebands separated by the modulation frequency. If the amplitude of the phase modulation is sufficiently small, we can represent the probe beam as the composition of a strong carrier and only two weak sidebands at frequencies $\omega_L \pm \omega_m$ [52]. Both the probe and the pump beams are directed to the atomic vapour cell: as in saturation spectroscopy technique, the pump modifies the dispersion properties of the atomic system and the probe investigates them. The intensity of the emerging probe beam is then observed with a photodiode and the electric signal arising from such device is de-modulated at the same modulation frequency ω_m. When a scan of the laser frequency ω_L is introduced, the de-modulated signal of the photodiode has a profile as in Fig. 2.4, due to different interaction of the three frequency components of the probe beam with the atomic system. As already mentioned, in the modulation transfer technique used to lock the cooler frequency in our case the modulation is imposed in the frequency of the pump rather then to the probe beam. In this case, if the interactions of the pump and the probe beam with atoms are sufficiently non-linear, the frequency modulation of the pump can be transferred to the unmodulated probe. The great advantage of modulation transfer technique is that in this case the strongest signals are observed for closed transitions [51]. Moreover, modulation transfer only takes place when the sub-Doppler resonance condition

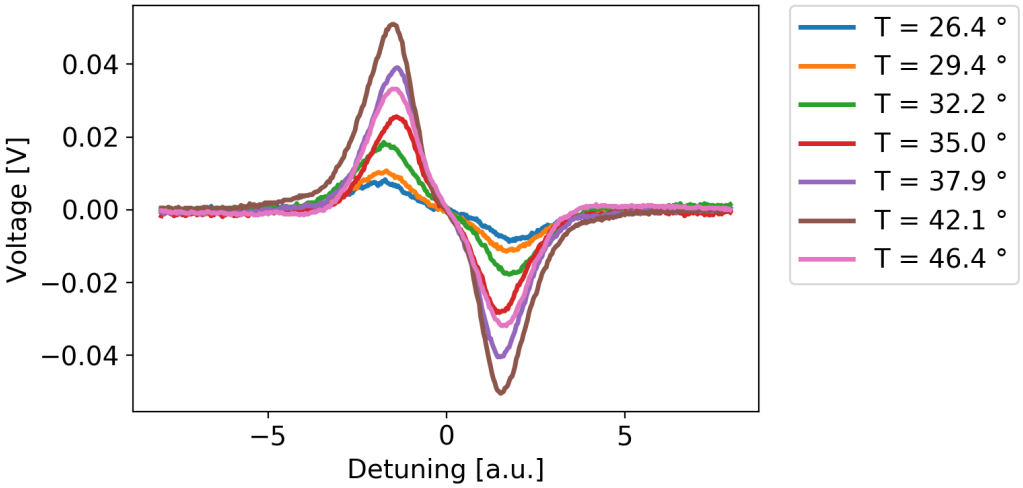

Figure 2.4: Optimization of the modulation transfer spectroscopy signal in dependence on the temperature of the atomic vapour cell. The signal and its slope in correspondence of the zero crossing increase with temperature up to a maximum for $T = 42.1°$, that is thus chosen as the working point for the laser locking. We note that the units in the x axis are arbitrary: the aim of the optimization was to analyse the changes in the signal slope, so an accurate calibration of the laser frequency scan was not performed. Anyway, the width of the spectroscopy signal is of the order of the natural linewidth of the transition, that is 6 MHz.

is satisfied, which leads to a flat, zero background signal where the zero crossing is accurately centred in correspondence of the atomic transition.

The spectroscopy signal has been optimized for two different parameters: the temperature of the cell, and the ratio of the powers in pump and probe beam. Fig. 2.4 shows the spectroscopy signal obtained for different temperature of the vapour cell. We see that the signal and its slope in correspondence of the zero crossing increase with temperature up to a maximum for $T = 42.1°$, that is thus chosen as the working point for the laser locking. The pump and probe powers analysis is reported in Fig. 2.5, where the difference between the maximum and the minimum of the spectroscopy signal ΔV is plotted versus the ratio P_{pump}/P_{probe}. We can see that the modulation transfer spectroscopy signal is maximum when the two beams have almost the same power.

Therefore, with modulation transfer spectroscopy the cooler light is locked to the atomic transition. Then the laser light is divided to create all the lights needed for the MOT. The frequency of each light is set using a dedicated Acousto-Optic Modulator (AOM), that introduces the desired detuning from the resonance. In particular, 2D and 3D MOT lights are red-shifted by 15 MHz.

The repumping light frequency is instead locked to the cooler frequency via a beat note stabilization. The cooler and repumper lights are superimposed and then observed with a fast photodiode. Because of the interference between the two radiation, the intensity observed with the photodetector oscillates with a frequency equal to the difference between the frequencies of the two laser beam, the so-called beat note. The oscillating electric signal of the photodiode is then digitalized and down-converted to

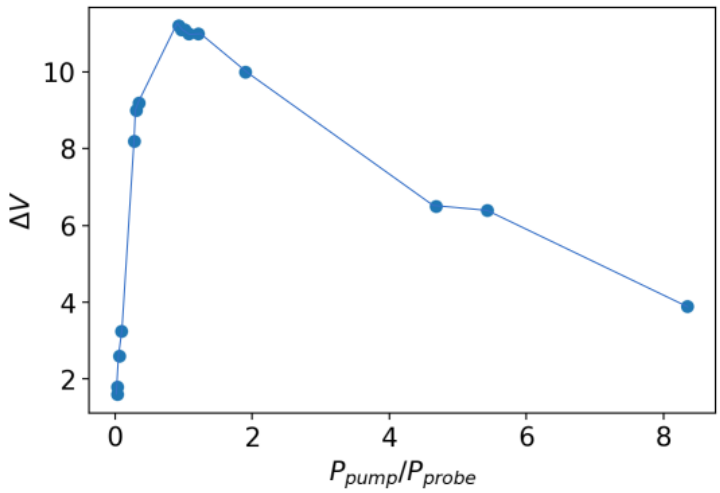

Figure 2.5: Optimization of the spectroscopy signal, varying the power of pump and probe beam. In figure the difference between the maximum and the minimum of the spectroscopy signal ΔV is plotted versus the ratio P_{pump}/P_{probe}. The maximum signal is obtained when pump and probe beam have the same power.

a slower frequency. In particular, the down-conversion process divides the frequency of the digitalized signal by an integer number that is set to $64 \times 105 = 6720$. Finally, the down-converted digital signal is compared to a well-known local oscillator signal, and the frequency difference between the two is used as error signal to lock the repumper frequency. In particular, the frequency of the repumper is set by choosing the local oscillator frequency, that fixes the difference between the cooler and the repumper lasers. The repumper frequency is set to be 6.750 GHz above the cooler one, which is locked 182 MHz below the closed transition $F = 2 \rightarrow F' = 3$.

2.2.2 Vacuum and optical systems

The vacuum and laser systems used to create the 2D and 3D MOTs are illustrated in Fig. 2.6.

The vacuum system has a dual chamber configuration: ^{87}Rb atoms are extracted from a vapour cell below the 2D MOT chamber at about 40° C, they are cooled and collimated by a 2D MOT and then transferred to the 3D MOT chamber via a push beam. A filter for the atomic beam is placed between the two vacuum chambers: it corresponds to two thin tubes with diameters 1.5 mm and 2 mm, 2 cm and 3 cm long respectively.

For the 2D MOT an elliptical beam is created by means of a telescope with two cylindrical lenses of focal lengths $f_1 = 100$ mm and $f_2 = 150$ mm. With such telescope a beam elongated in the horizontal direction is created with an aspect ratio of 3 between the horizontal and the vertical directions, so that almost all the 2D MOT cell is illuminated by the cooling light. The beam is then retro-reflected to create the counter-propagating beam for the 2D MOT. Two quarter-wave ($\lambda/4$) plates set the opposite circular polarizations of the counter-propagating beams. Such optical scheme

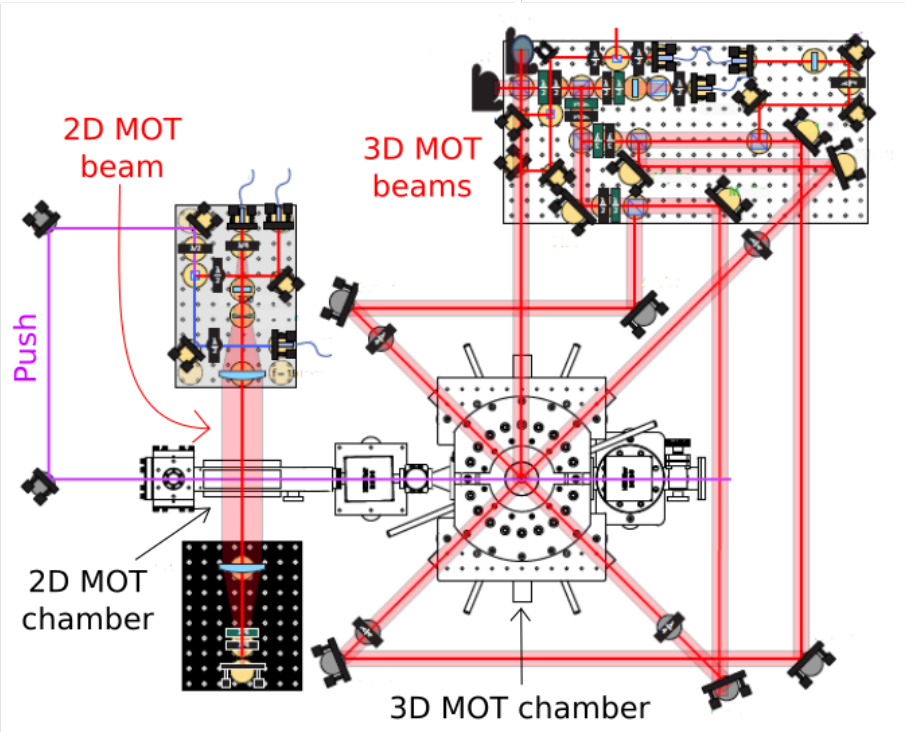

Figure 2.6: Vacuum and laser system for the magneto optical trap of ^{87}Rb.

is used both for the horizontal and for the vertical beams of the 2D MOT. The power of the two beams is approximately 200 mW. The inhomogeneous magnetic field requested for the 2D MOT is generated with two couple of Ioffe coils, driven with a current of about 5 A.

The push is realized with a beam with waist of about 1 mm and power $P = 1.5$ mW. The direction of the beam is finely tuned to center the atomic filter, such that the beam can get through and arrive in the 3D MOT chamber.

For the 3D MOT six independent laser beams are used. They are realized starting from the same fibre output, divided in different beams by three polarizing beam splitters (PSB). The power of each beam can be set with a half-wave plate ($\lambda/2$) placed before the PBS. The total power of the 3D MOT beams, measured at the output of the fiber before all splittings, is set to be around 110 mW. The inhomogeneous magnetic field needed for the magneto optical trap is created by a set of two coils in an anti-Helmholtz configuration, placed in the vertical direction above and below the vacuum chamber. The coils are composed by 36 winding of a copper wire, in which flows an electric current of 13 A, in opposite directions for the two coils. Before implementing the coils in the experimental system, a characterization of the magnetic field they produce has been done. To do that, we powered one coil at a time and measured the magnetic field in several positions along the axial direction with an Hall probe. We repeated the measurement for different values of the electric current and the results are illustrated in Fig. 2.7. We note that the distances are taken from an arbitrary position. The measured data are fitted with a function that represents the magnetic field generated

by a coil with N windings according to the Biot-Savart low:

$$B(z) = \frac{\mu_0 I N}{2} \frac{R^2}{(z^2 + R^2)^{\frac{3}{2}}}, \tag{2.9}$$

where μ_0 is the magnetic permeability, I is the elctric current that flows in the coil and R its radius. We can see that the fit curve well represents the experimental data. The fit parameters obtained are reported in Table 2.1, according to the fit function:

$$y = A \frac{r_0^2}{((x - x_c)^2 + r_0^2)^{\frac{3}{2}}} + c. \tag{2.10}$$

From the characterization of the two coils the value of the gradient of the magnetic field experienced by the atoms at the center of the 3D MOT can be calculated. In our setup the centre of the two coils are at distance 64.8 mm, so that the magnetic field gradient is 15 Gauss/cm for a powering electric current of 13 A, as used for the 3D MOT realization.

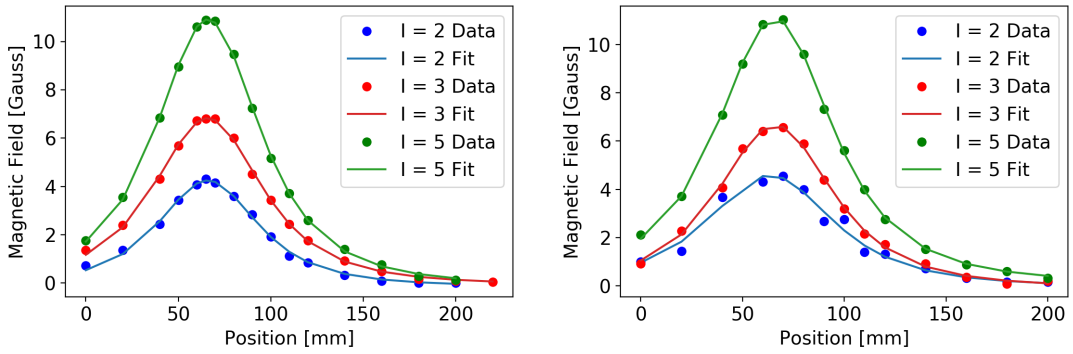

(a) Coil A **(b)** Coil B

Figure 2.7: Experimental data and relative fit for the characterization of the magnetic field produced by the two coils for the 3D MOT. For each coil the magnetic field produced with several powering electric currents is measured with an Hall probe, than a fit with the function in Eq. (2.10) is performed.

Coil	I (A)	A (Gauss/mm)	r_0 (mm)	x_c (mm)	c (Gauss)
A	2	184 ± 7	42.0 ± 1.4	65.9 ± 0.5	-0.15 ± 0.07
A	3	313 ± 6	45.3 ± 0.8	65.8 ± 0.3	-0.09 ± 0.05
A	5	481 ± 6	43.5 ± 0.4	65.97 ± 0.15	-0.12 ± 0.05
B	2	224 ± 25	48 ± 4	63.6 ± 1.6	-0.06 ± 0.20
B	3	297 ± 10	43.9 ± 1.2	65.9 ± 4.2	-0.10 ± 0.08
B	5	483 ± 7	43.8 ± 0.5	65.9 ± 0.2	0.08 ± 0.06

Table 2.1: Fit parameter of the coils characterization.

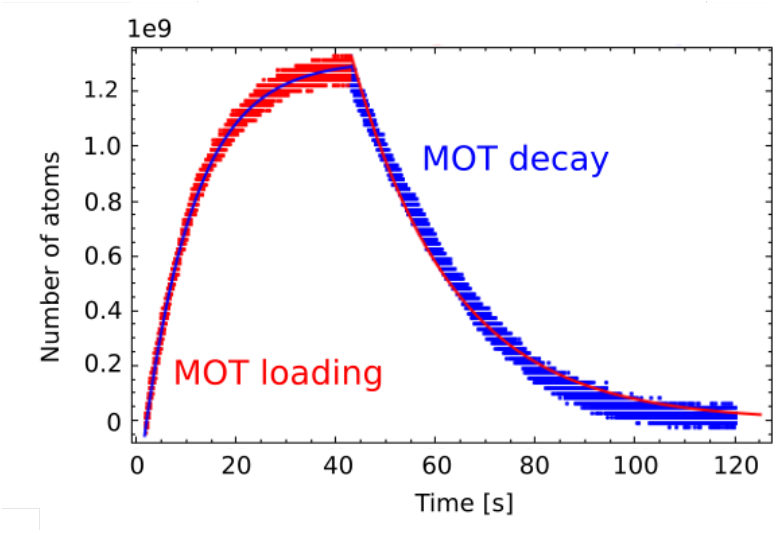

Figure 2.8: Time evolution of the atomic population inside a MOT. Two regions can be individuated: the loading (red), where the number of atoms rapidly increases up to a saturation value, and the decay of the MOT (blue), when the 2D MOT is abruptly turned off and the population in the 3D MOT decreases because of collision with the background gas.

2.3 Optimization of the 3D MOT loading efficiency

In this section we study the loading efficiency of the 3D MOT. We say that a MOT is efficient if it is capable to load a large number of atoms in a short time. In general, the time evolution of the atomic population inside a MOT is characterized by a trend as in Fig. 2.8, where the time dependence of the number of atoms in the trap is illustrated. We note two different regions: the loading, where the number of atoms rapidly increase up to a saturation value, and the decay of the MOT, when the 2D MOT is abruptly turned off and the population in the 3D MOT decreases because of collisions with the background gas. We can describe both evolutions with the same differential equation. In particular, the time-evolution of the atomic population N con be represented by the equation:

$$\frac{dN}{dt} = R(t) - \frac{N}{\tau}, \tag{2.11}$$

where $R(t)$ is the loading rate of the MOT, that vanishes when the 2D MOT is turned off, and τ is its decay constant. During the loading we can assume that the loading rate is constant, so the solution of the previous equation is:

$$N(t) = R\tau \left(1 - e^{-\frac{t}{\tau}}\right). \tag{2.12}$$

In the decay regime the loading rate is null, so the population exhibit an exponential decay:

$$N(t) = N_0 e^{-\frac{t}{\tau}}, \tag{2.13}$$

where N_0 is the number of atoms in the MOT when the 2D MOT is turned off.

The experimental data in Fig. 2.8 are fitted with Eq. (2.12) and Eq. (2.13) for the loading and decay part respectively. From the fit we obtain the following parameter:

$$\begin{aligned} R &= (1.278 \pm 0.001) \times 10^8 \text{ atoms/s} \\ \tau_l &= (10.31 \pm 0.02) \text{ s} \end{aligned} \tag{2.14}$$

for the loading, and:

$$\begin{aligned} N_0 &= (1.7 \pm 0.1) \times 10^9 \text{ atoms} \\ \tau_d &= (20.23 \pm 0.01) \text{ s} \end{aligned} \tag{2.15}$$

for the decay. We note that the decay time τ_d is double than the one for the MOT loading τ_l: during the loading, the collisions with the atomic beam delivered by the 2D MOT increase the decay rate. Anyway, the lifetime of the MOT is long, thanks to the ultra-high vacuum in the 3D MOT chamber.

As already mentioned, in this section we present the 3D MOT loading efficiency optimization, so we focused our attention rather to the loading time-evolution than to the lifetime of the MOT. The aim of the optimization is to obtain the maximum rate R permitted. To do that, we have to consider both the efficiency of the 2D MOT in creating an atomic flux suitable for the capture in the 3D MOT and the efficiency of the 3D MOT itself in creating a trap for atoms. In particular, the optimization of the 2D MOT is presented in Sec.2.3.2, while that of the 3D MOT is illustrated in Sec. 2.3.3. Before that, in Sec. 2.3.1 we present the two measuring techniques used during the optimization: the fluorescence and absorption imaging.

2.3.1 Measuring techniques

To probe the atomic population, we used two different optical techniques: fluorescence and absorption imaging. In the first one, the light emitted by the atoms is collected by a photodiode, that measures its intensity. This method is particularly useful to measure the number of atoms in a MOT, where they continuously absorb and re-emit photons, and provides a non-destructive probe. Absorption imaging is a superior method that provides more information about the atoms, but it is a destructive measurement. Here, the atomic cloud is illuminated by a resonant probe light and then the transmitted light is observed with a CCD. Atoms absorb the resonant light, so that their shadow is cast on the CCD. The image of such shadow provides information about the size and the optical density of the atomic cloud, from which we can extract the number of atoms and the temperature.

Fluorescence

We used fluorescence measurements for the first part of the 3D MOT loading optimization. This method is particularly suitable for the optimization because it provides a measurement of the number of atoms in the MOT without destroying it, so that a quick optimization can be performed. Moreover, it is particularly easy to set up: in

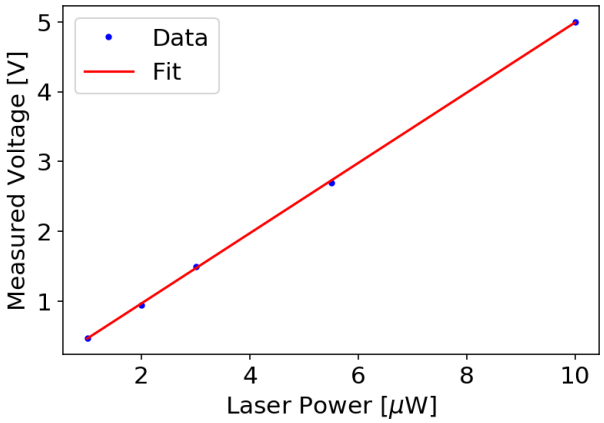

Figure 2.9: Calibration of the photodiode used for fluorescence imaging measurement.

our case a photodiode is placed in front of one of the 3D vacuum chamber windows to measure the emitted intensity. To characterize the response of the photodiode, it was previously calibrated by illuminating it with a laser light with well-known and variable power. The photodiode is used with a loading resistance of 500 kΩ and the potential difference over the resistance is measured. The results of the calibration are reported in Fig. 2.9. From the linear fit we get the power to voltage conversion: (0.503 ± 0.04) V/μW.

As already mentioned, from a measure of the emitted power it is possible to extract the number of atoms in the MOT. Indeed, the emitted power P_{em} depends on the number of emitting atoms N_a, according to:

$$P_{em} = \hbar\omega N_a R, \tag{2.16}$$

where ω is the frequency of the emitted light and R the rate of emission processes, that can be written as:

$$R = \frac{I}{I_{sat}} \frac{\gamma}{2} \frac{1}{1 + \frac{I}{I_{sat}} + 4\left(\frac{\delta}{\gamma}\right)^2}, \tag{2.17}$$

where I is the intensity of the laser that illuminates the atomic population, $I_{sat} = \frac{2\pi^2\hbar\gamma c}{3\lambda^3}$ is the saturation intensity, γ is the natural linewidth of the transition and δ the detuning. P_{em} correspond to the whole emitted power, but we can collect only a fraction of it with the photodiode. In particular, the measured power depends on the solid angle Ω_s covered by the photodiode area:

$$P_{meas} = \Omega_s P_{em}, \tag{2.18}$$

and the solid angle can be written as:

$$\Omega_s = \frac{A_{PD}}{4\pi D^2}, \tag{2.19}$$

where A_{PD} is the photodiode area and D its distance from the atomic cloud. Therefore, the number of atoms can be calculated as:

$$N_a = \frac{P_{meas}}{\hbar\omega R\Omega_s}. \tag{2.20}$$

In our case, we use a photodiode with square a area of 1 cm^2 placed at a distance of about 15 cm from the centre of the 3D MOT vacuum chamber. The laser light that illuminates the atomic population is one of the 3D MOT beam, with a detuning of 15 MHz from the resonance. Taking into account the photodiode calibration too, we obtain a volt to number of atoms conversion of 8.5×10^8 atoms/V.

The accuracy in the measurement of the atom number is limited mainly by the uncertainty in the solid angle: the distance between the photodiode and the atomic cloud is an estimate based on the geometry of the vacuum cell, that introduces an error of around 10% in the evaluation of the number of atom. However, the calculated conversion yields the correct order of magnitude of the atom number in the cloud, and for the optimization measurement performed the relative value of it between two distinct measurements is sufficient. The volt to number of atoms conversion depends on the detuning between the 3D MOT light and the atomic resonance. Therefore, we cannot use the fluorescence technique to optimize the frequency of such light for the MOT loading, because the conversion would change in each measurement. For this reason and to have an independent measurement of the atom number we implemented the absorption imaging method too.

Absorption Imaging

For the absorption imaging measurements, a probe beam with waist of about 5 mm is focused to the atomic cloud. The transmitted probe light from the atomic cloud is observed with an Andor Camera iKon M-934. In particular, for each measurement three different images are acquired: the profile of the probe beam absorbed by the atoms, the probe profile without the MOT and an image of the background. Combining these images, a measurement of the optical density of the cloud is obtained. Indeed, the absorbed intensity follows the Beer law:

$$I_t = I_0 \exp^{-OD}, \tag{2.21}$$

where I_t is the transmitted intensity, I_0 is the incident intensity and OD is the optical density of the medium. Therefore, the spatial profile of the optical density of the atomic cloud can be obtained from the following combination of the three acquired images:

$$OD(x,y) = -\log\left(\frac{I_1(x,y) - I_3(x,y)}{I_2(x,y) - I_3(x,y)}\right), \tag{2.22}$$

where $I_i(x,y)$ with $i = 1,2,3$ is the spatial intensity profile of the i-th acquired image. Fig. 2.10 shows an example of the optical density of the cloud. From such measurement we get several quantities of the atomic cloud. The optical density is indeed defined as:

$$OD(x,y) = \sigma \int n(x,y,z)dz, \tag{2.23}$$

where $n(x,y,z)$ is the density of atoms and σ is the absorption cross section, that, when the illumination intensity is well below saturation, can be written as:

$$\sigma = \frac{3}{2}\frac{\lambda^2}{\pi}\frac{1}{1+4\left(\frac{\delta}{\gamma}\right)^2}. \tag{2.24}$$

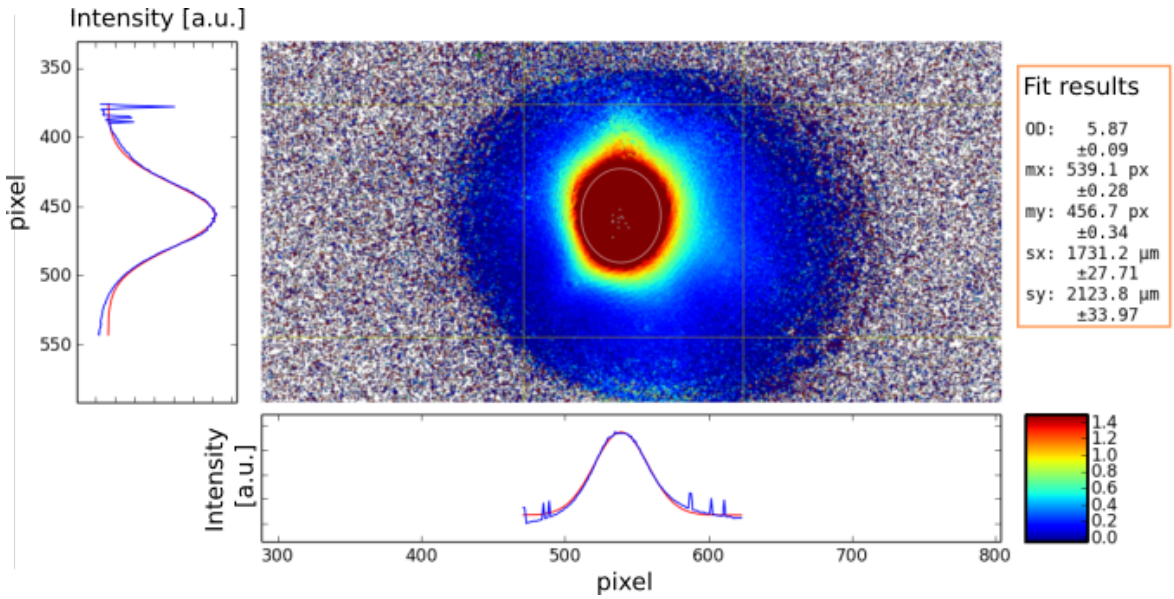

Figure 2.10: Screenshot of the acquisition program for the absorption imaging measurement. The atomic cloud is imaged after 3 s of TOF. The optical density is calculated by the combination of three acquired images, as in Eq. (2.22). The horizontal and vertical profile of such image are obtained by integration on the y and x variable respectively. Then a Gaussian fit of these profile is performed to obtain the value of the centre of the Gaussian, its width and the maximum value of the optical density.

If we consider a Gaussian density profile in each direction, namely:

$$n(x,y,z) = \frac{N_a}{(2\pi)^{3/2}\sigma_x\sigma_y\sigma_z} \exp^{-\frac{x^2}{2\sigma_x^2}-\frac{y^2}{2\sigma_y^2}-\frac{z^2}{2\sigma_z^2}}, \tag{2.25}$$

where N_a is the number of atoms in the cloud, the optical density integral can be calculated to get:

$$OD(x,y) = \frac{\sigma N_a}{2\pi\sigma_x\sigma_y} \exp^{-\frac{x^2}{2\sigma_x^2}-\frac{y^2}{2\sigma_y^2}}. \tag{2.26}$$

Therefore, the optical density has a two-dimensional Gaussian profile, as can be seen from Fig. 2.10. From a two-dimensional Gaussian fit of the measured $OD(x,y)$ we can extract the centre for the cloud and its widths, and in addition the number of atoms N_a can be calculated from the value of the optical density at the centre of the cloud OD^{max}:

$$N_a = \frac{2\pi\sigma_x\sigma_y}{\sigma} OD^{max}. \tag{2.27}$$

Before using the absorption imaging technique to optimize the efficiency of the MOT loading, two different calibrations have to be done. First, the probe beam frequency has to be optimized to maximize the signal we get from the imaging. The probe calibration is performed as follows: we load the 3D MOT for 5 seconds, then we turn off the trap and perform a 6 ms time of flight (TOF) of the cloud. After the TOF, an image of the cloud is acquired with the described method. Such procedure is repeated for several frequencies of the probe light, tuned with an AOM. In this way, we obtain

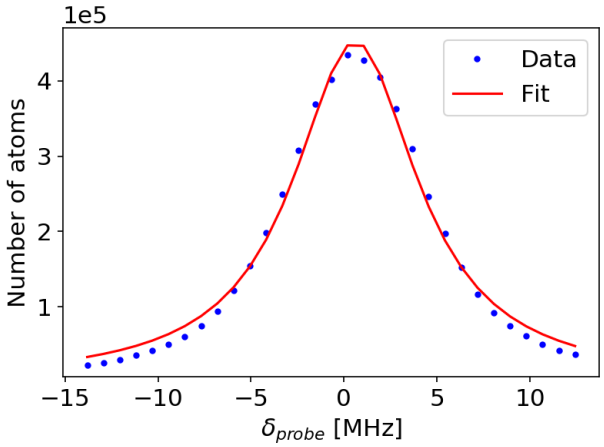

Figure 2.11: Probe frequency calibration. Varying the probe frequency with an AOM we obtain the absorption profile of the atoms, then a Lorentzian fit is preformed. We get that the width of the absorption line is (8.1 ± 0.4) MHz.

the absorption profile in Fig. 2.11, where the measured number of atoms is plotted in dependence on the probe detuning from the resonance. We perform a Lorentzian fit of the experimental data and get that the width of the line is (8.1 ± 0.4) MHz. This is larger than the natural linewidth of 6 MHz, indicating the presence of a power broadening of the line. As expected, we see that the absorption imaging signal is maximum when the probe light is resonant with the atomic transition, so we take this value of detuning as a working point.

Secondly, we perform a calibration of the Andor Camera, to get the pixel to μm conversion. Indeed, after the 3D MOT chamber, the probe light passes through a telescope with lenses of nominal focal lengths $f_1 = 300$ mm and $f_2 = 25$ mm, so that the expected magnification of the atom cloud is $25/300 = 1/12$. To get the real dimension of the cloud it is necessary to calibrate the exact magnification of the atom cloud image. To do that, we image the atom cloud loaded for 5 seconds after several duration of TOF. The cloud fall down because of gravity, following the equation:

$$y = \frac{1}{2}gt^2 + v_0 t + x_0, \tag{2.28}$$

where y is the vertical position of the atomic cloud obtained from the two-dimensional fit of the OD spatial profile, g is the gravitational acceleration and the time t correspond to the set time of flight for the cloud. Fig. 2.12 shows the vertical position of the centre of the cloud after several TOF. We can see that the trajectory is a parabola as expected, and from the fit we get the desired pixel to μm conversion of 1 px $= (92 \pm 3)$ μm. Such conversion will be used in the following to rescale the measured size of the cloud in real units.

From the time of flight measurement another important information about the cloud can be obtained: the temperature. In particular, we can define the temperature of the atomic cloud from the energy equipartition theorem:

$$\frac{1}{2}m \langle v \rangle^2 = \frac{1}{2}k_B T, \tag{2.29}$$

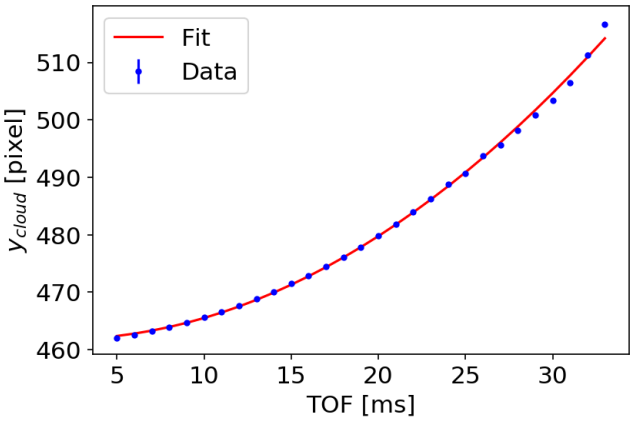

Figure 2.12: Andor Camera calibration. The vertical position of the atomic cloud centre is plotted in dependence of the time of flight performed. The trajectory of the cloud is a parabola because of the effect of gravity. The fit is performed with a parabolic function $y = \frac{1}{2}gt^2 + v_0t + x_0$. We can get the pixel to μm conversion by comparing the obtained fit parameter $\frac{1}{2}g = (0.053 \pm 0.002)$ pixel/ms^2 with the well known value of the gravitational acceleration $g = 9.81$ m/s^2. The obtained conversion is thus 1 px $= (92 \pm 3)$ μm.

where m is the mass of the atoms, $\langle v \rangle$ their mean velocity, k_B the Boltzmann constant and T the temperature of the sample. If TOF is large enough that the size of the atomic cloud is completely dominated by the expansion, namely $\sigma(TOF) \gg \sigma(0)$ where $\sigma(t)$ is the size of the cloud after an expansion time t, then the mean velocity in the x direction is $\langle v \rangle = \sigma_x/TOF$ and the same for the y direction. Indeed, particles velocities are transformed in distance from the cloud center during the expansion. Therefore, the temperature of the cloud in the x direction can be calculated from the size of the cloud in such direction, according to the relation:

$$\sigma_x = \sqrt{\frac{TOF^2 k_B T_x}{m}}, \tag{2.30}$$

and similarly for the temperature in the y direction. Fig. 2.13 shows the plot of the measured size of the cloud in the horizontal (a) and vertical (b) direction in dependence on the TOF performed. Data are fitted with the function:

$$y = \sqrt{\sigma_0^2 + A(TOF - t_0)^2} \tag{2.31}$$

to extract the temperature of the cloud in the two directions. In particular, we obtain $T_x = (181 \pm 8)$ μK and $T_y = (225 \pm 8)$ μK. These value are of the same order of the Doppler limit temperature of 150μK.

2.3.2 2D MOT optimization

To have an efficient 3D MOT loading process, we first optimize the atom flux from the 2D MOT. Indeed, an atom can be trapped in the 3D MOT only if its velocity is below a critical capturing velocity $v^{max} \sim \Gamma\lambda/2\pi$, that is the velocity for which the Doppler

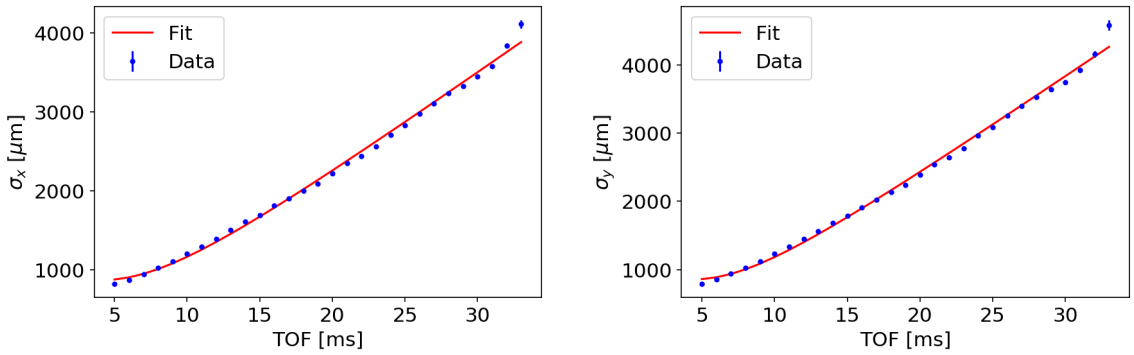

(a) Horizontal direction **(b)** Vertical direction

Figure 2.13: Plot of the cloud sizes in horizontal (a) and vertical (b) direction. To get the temperature of the cloud a fit is performed with the function: $y = \sqrt{\sigma_0^2 + A(TOF - t_0)^2}$. Comparing the used fit function to Eq. (2.30), we can extract the temperature of the cloud from the fit parameter A. In particular, we obtain: $T_x = (181 \pm 8)$ μK, $T_y = (225 \pm 8)$ μK.

shift equals the natural linewidth of the transition. Therefore, we need to optimize the parameters of the 2D MOT to obtain an atomic flux of a large number of atoms, but with a quite low mean velocity, as in our case $\Gamma\lambda/2\pi \sim 5$ m/s. In particular, we explore the dependency of the number of atoms loaded in the 3D MOT, after a 5 seconds loading time, on the following parameters: the electric current on the Ioffe coils, the frequency of the 2D MOT cooler and repumper lasers and the frequency and the power of the push beam. All the measurement for the optimization of the 2D MOT parameter were done with the fluorescence imaging technique, presented in the previous section.

We first report the optimization of the magnetic field produced by the 2D MOT coils. We use the following nomenclature for the four coils: A and C coils are positioned in the vertical direction, while B and D coils in the horizontal direction, perpendicular to the atomic flux. We start from a current of 4 A for A and B coils, and vary the current in C and D to maximize the number of atoms in the 3D MOT after the loading process. Fig. 2.14 (a) shows the result of such optimization: we find that the best configuration is reached when in the horizontal coils couple B-D flows the same powering current, while the vertical coils couple A-C needs to be unbalanced with a ratio in the powering current of $I_C/I_A = 1.075$. Then, we vary the currents in all the coils keeping the ratio I_C/I_A constant and setting the same current in the B-D couple. The results of this second step of coils optimization are illustrated in Fig. 2.14 (b). We found the best configuration of the coils current to be: $I_A = 5.5$ A, $I_B = I_D = 5$ A, $I_C = 5.9$ A. The gradient produced by the coils in this configuration is about 19 G/cm.

Subsequently, we optimize the frequencies of the 2D MOT cooler and repumper beams, tuned by changing the corresponding AOM driving frequency. Fig. 2.15 shows the results of such optimization: the measured number of atoms in the 3D MOT after a loading time of 5 seconds is plotted in dependence on the 2D MOT cooling beam

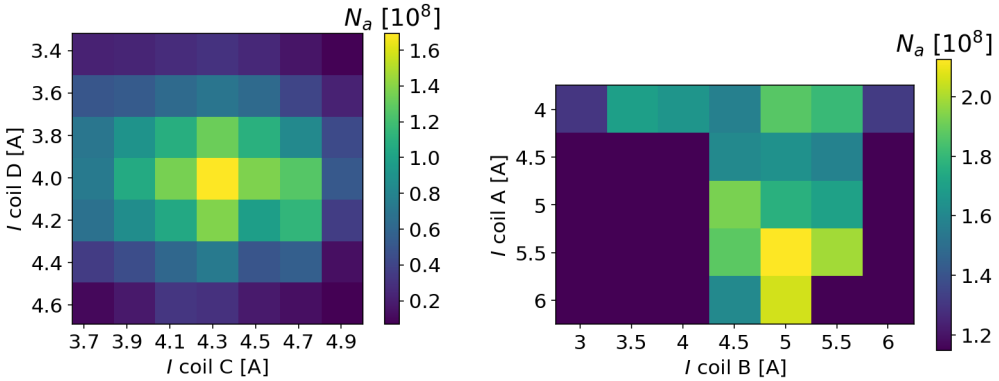

(a) Optimization of C and D coils

(b) Optimization of A and B coils

Figure 2.14: Optimization of the electric current in the 2D MOT coils measuring the number of atoms in the 3D MOT after a loading time of 5 seconds. In (a) the current in C and D coils is varied, while in A and B coils the current is set to be 4 A. The results shows that the best point is when in the couple B-D flows the same current, while the couple A-C is unbalanced. In (b) the measured number of atoms in function of the current in A and B coils is reported. The dark blue point correspond to value of current not explored during the optimization. In this case, the current in C and D coils is set to follow the relations: $I_B = I_D$, $I_C/I_A = 1.075$, as suggested by the results in (a). The best configuration is found to be: $I_A = 5.5$ A, $I_B = I_D = 5$ A, $I_C = 5.9$ A.

detuning δ_c for several value of the detuning of the repumper beam from the cooler δ_r. The best point is found to be: $\delta_c = -16.8$ MHz, $\delta_r = 6785.9$ MHz.

Finally, we vary the frequency and the power of the push beam to optimize the 3D MOT loading efficiency. The push frequency is controlled with a dedicated AOM, so that it can be modified by varying the driving frequency of the AOM. Fig. 2.16 (a) shows the measured number of atoms in dependence on the push detuning from the resonance δ_p, and the relative fit with a Gaussian function. Although the measured data are pretty scattered, it is possible to individuate a peak in the number of atoms in the MOT. In particular, the fit individuates the centre of the Gaussian function in correspondence of a detuning $\delta_{p0} = (-5.7 \pm 0.9)$ MHz. Therefore, the optimal push frequency is red-detuned from the resonance by approximately one linewidth: in this way the push light interact more with atoms propagating in the direction opposite to the 3D MOT chamber, it slows them down and eventually changes the direction of their velocity. Fig. 2.16 (b) shows the value of the measured number of atoms after the 5 seconds loading time in dependence on the push power. We tune the power of the push beam with an half-wave plate in front of a PBS in the push path toward the 2D MOT chamber. We can see that the higher the power of the push is the higher is the loading efficiency of the MOT. We chose as working point the power of 1.5 mW.

2.3.3 3D MOT optimization

As already mentioned, also two parameters of the 3D MOT itself have to be considered to maximize its loading efficiency: the powering current of the anti-Helmholtz coils and

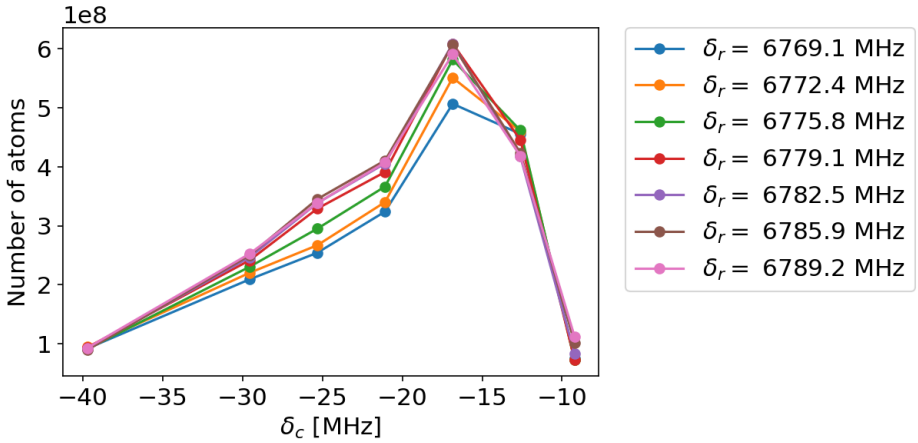

Figure 2.15: Optimization of the frequencies of the 2D MOT cooler and repumper light: the plot shows the number of atoms in the 3D MOT after a loading time of 5 seconds in dependence on the 2D MOT cooling beam detuning δ_c for several value of the detuning of the repumper from the cooler δ_r.

the frequency of the cooler light of the 3D MOT. Indeed, on such parameter depends the capability of the 3D MOT to trap atoms.

First, we report the magnetic field optimization. In this case, we measure the number of atoms in the MOT when it is saturated with the fluorescence imaging technique. We proceed as follows: we change the current of the coils and measure the saturation number of atoms in the trap, once it has stabilized to the new value. Fig. 2.17 shows the results of such optimization: we can see that the loading efficiency of the MOT grows with the current in the first part of the curve. Than it forms a plateau where the saturation number of atoms is more or less constant for current values between 13 and 22 A. Therefore, we choose the current value of 13 A to be our

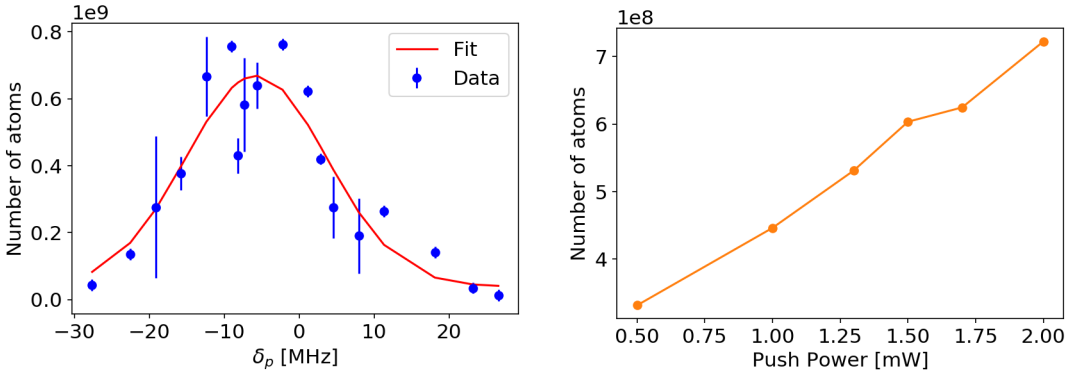

(a) Optimization of the push frequency **(b)** Optimization of the push power

Figure 2.16: Optimization of the push beam. In (a) the measured number of atoms in dependence on the push detuning from the resonance δ_p is plotted. We see that the optimal point is reached for a slightly red-detuned light. Plot (b) represent the measured number of atoms in dependence on the power if the push beam.

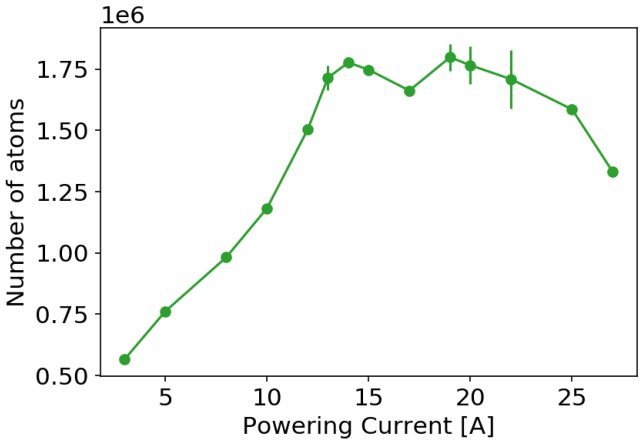

Figure 2.17: Optimization of the magnetic field of the anti-Helmholtz coils. The plot shows the number of atoms at the MOT saturation in dependence on the powering current of the two coils. We choose 13 A to be our working point. This measurement has been performed with the fluorescence imaging technique.

working point, because it is the smaller value with higher number of atoms. A lower electrical current is useful to avoid an excessive heating of the coils.

Then we vary the frequency of the cooler beam of the 3D MOT. As already mentioned, in this case the fluorescence imaging technique cannot be used because the volts to number of atoms conversion depends of the detuning of the 3D MOT light from the atomic resonance. Therefore, we use the absorption imaging technique and proceed as follows: we change the 3D MOT cooler frequency modifying the driving frequency of the dedicated AOM and the measure the number of atoms in the MOT after a loading time of 5 seconds and a time of flight of 8 ms. In Fig. 2.18 the measured number of atoms in dependence on the detuning of the 3D MOT light from the resonance δ_{3D} is

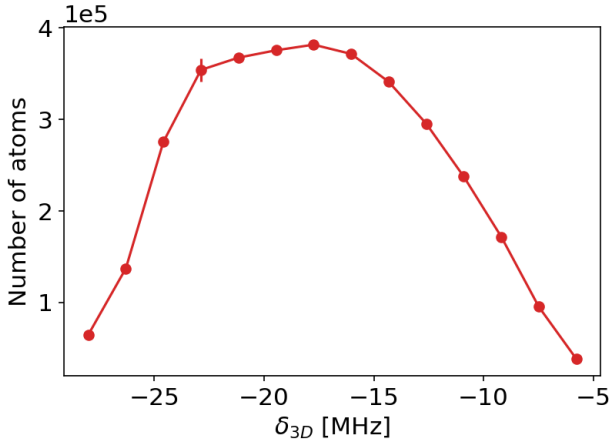

Figure 2.18: Optimization of the frequency of the 3D MOT cooler beam. The plot shows the number of atoms in dependence on the detuning of the 3D MOT cooler light from the resonance δ_{3D}. The maximum efficiency is obtained for a detuning of about -20 MHz. This measurement has been performed with the absorption imaging technique.

illustrated. We see that the maximun efficiency is obtained for a detuning of about -20 MHz.

In conclusion, the performed optimization yields to a MOT of about 10^9 atoms at saturation with a temperature of about 200 μK and a loading efficiency of $\sim 10^8$ atoms/s. We note that the temperature of atoms in the MOT is far from the critical temperature of condensation. To obtain an atomic superfluid another cooling technique has to be implemented: the evaporative cooling permits to reach the Bose-Einstein condensation.

Chapter 3

Tailored Optical Potentials with a DMD

The second part of my master thesis was dedicated to the realization and characterization of arbitrary optical potentials with a Digital Micromirror Device (DMD). Such device is a reflective spatial light modulator (SLM) that can be used to manipulate the spatial intensity profile of a laser beam. The working principle of the DMD is illustrated in Sec. 3.1 and in Sec. 3.2 its optical properties are described. Then, in Sec. 3.3 the optical setup I designed and aligned for the characterization of the DMD-made light patterns is presented. The DMD offers the possibility to create both static and time-dependent potentials. In Sec. 3.4 I investigate two main properties of static patterns: the smoothness of the image edges and the homogeneity of the image bulk. In particular, I present the capability to have smooth potentials by cutting the high frequency component of an image with an iris, and the feedback program that I wrote to obtain homogeneous potentials. Finally, in Sec. 3.5 I illustrate the main properties of a time-dependent potential created with the DMD, showing that the timing characteristic of the device are well suited for applications to atomic superfluids.

3.1 The Digital Micromirror Device

The Digital Micromirror Device (DMD) is a reflecting Spatial Light Modulator (SLM), a device that gives control over the amplitude and the phase of an incoming laser beam. For the atomic physics applications this device is preferable to other kind of SLMs, like Liquid Crystal Displays (LCDs), because it provides both truly static highly defined images and a fast switching rate, in case of a time-dependent potential is required.

The DMD used in this master thesis work is a DLP70000 Discovery ^{TM} 4100 0.7" XGA 2xLVDS, produced by Vialux, with a V-7000 board. This device is composed by an 1024×768 array of square mirrors. Each mirror has dimension of 13.68 μm and can be tilted over its diagonal axis by an angle of $\pm 12°$. The state of a single mirror is thus binary and can be accessed using a computer through the board. Mirrors can be arranged in any kind of binary pattern to reproduce a black and white image.

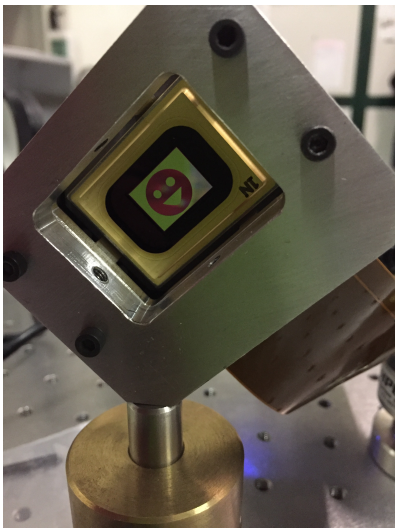

Figure 3.1: Picture of the DMD mounted in its support with a smiling image loaded on board.

A picture of the DMD mounted in its support is reported in Fig. 3.1. Here, a black and white smile is loaded in the DMD board and displayed on its screen: mirrors assume the tilt position fixed by the loaded image and make its visible on the DMD screen thanks to their different reflecting properties in the two states. The mounting support is tilted by a 45° angle, in such a way that the tilting axis of the mirrors is vertical. This is useful to obtain a mainly horizontal diffraction pattern, as it will be illustrated in Sec. 3.2, which is easier and safer to handle with an optical system.

3.1.1 Controlling the DMD

Vialux provides a default controlling program to communicate with the DMD: the ALP basic GUI. This program controls the DMD via an USB2.0 connection: a binary image can be sent to the device and a sequence of at most five alternating images can be created. The operation doable with this program are yet limited, so that it is not suitable for atomic physics applications of the DMD. A much deep control over the characteristic of the image and the timing properties of the sequence is indeed requested. For these reasons in this master thesis work I used the open source Python module by Sebastien Popoff ALP4lib to control the DMD [53].

ALP4lib is a Python module to control Vialux DMDs based on ALP4.X API, that uses the Dynamic-Link Library (DLL) files provided by Vialux. The ALP4lib library gives a number of function to interface with the device. For example one can allocate the memory for a sequence of images and send the sequence to the DMD using the functions `SeqAlloc` and `SeqPut` respectively, or set the timing properties of the sequence to display using the `SetTiming` function. In this way the only limitation in the operations that can be done are given by the intrinsic characteristic of the device.

The Discovery 4100 DMD used in this master thesis work has a RAM capacity on board of 32 Gbit, so it can store at most 43690 binary pattern. That gives the limit of

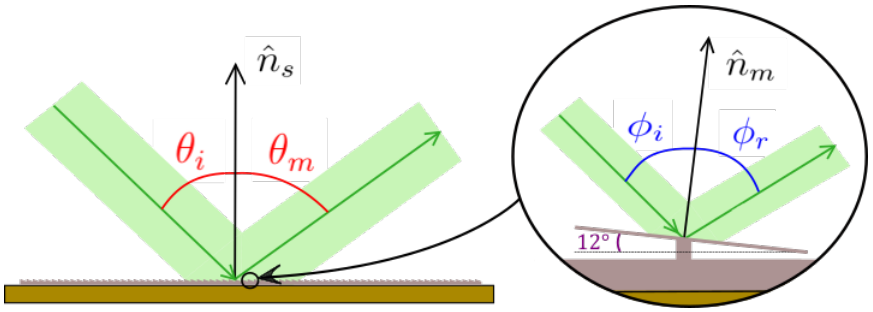

Figure 3.2: Illustration of the adopted angles convention: θ angles are taken from the DMD surface normal $\hat{n}_s$, while ϕ angles are taken from the mirrors normal $\hat{n}_m$.

the dimension of the sequence that can be send to DMD, assuming that the transfer process can be supported by the computer that controls the device. The limit on the timing properties is instead given by the higher array switching rate of the device, that for the DMD used in this work is 22727 Hz.

3.2 Optical Properties

The DMD is a reflecting device so it is important to determine its behaviour when it is illuminated with a laser beam. In this thesis work I used a 532 nm laser beam to illuminate the DMD and to realize a repulsive optical potential for alkali atoms.

As already mentioned, each mirror of the DMD can be set in one of two different states, tilted by an angle of $\pm 12°$ from the DMD surface plane. The light impinging on a mirror is thus reflected in two different directions, depending on the tilt state of the mirror. But to understand the whole optical behaviour of the device, it has to be noticed that the DMD is composed by an array of micrometer-sized mirrors. Thus, it acts like a 2D diffraction gratings for the incoming light because the mirrors dimension is comparable to the wavelength of the laser beam. Therefore, the laser light impinging on the DMD surface is not just reflected into one of the two directions fixed by the tilt state of mirrors, but rather into a number of different diffraction orders.

In general, the distribution of the laser power over many diffraction orders is inconvenient, because only one of these direction is used. The power of the reflected light in a particular direction can be maximized, finding the blazing condition of the device, which is discussed in the next section.

3.2.1 Blazing condition

In a diffraction grating the laser light reflected from a single element of the grating interfere with light reflected from the surrounding elements. In some direction the interference is constructive and destructive in the others, so that light is overall reflected only in particular directions called diffraction orders. Analyzing the diffraction grating problem more formally, one can find the grating equation [54]:

$$m\lambda = d(\sin\theta_i + \sin\theta_m), \tag{3.1}$$

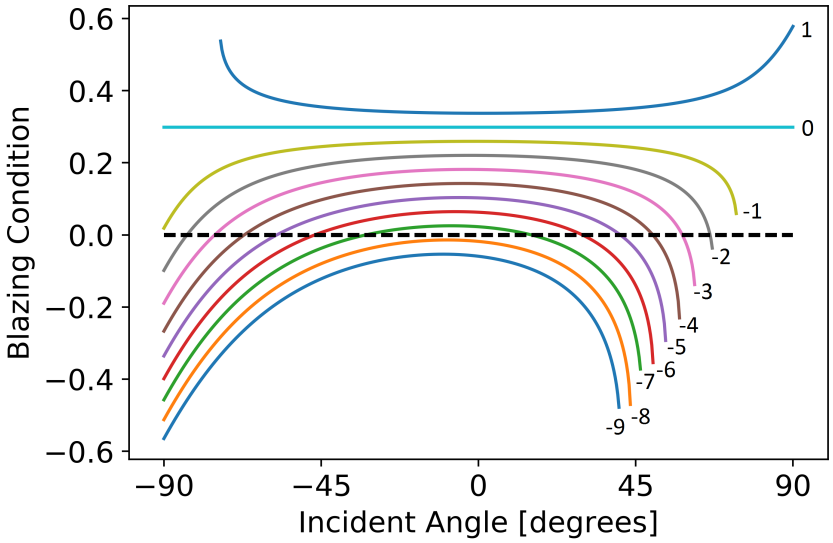

Figure 3.3: Trend of the corrected blazing condition of equation (3.3) in dependence of the angle of incidence θ_i for several order of diffraction m, printed beside the corresponding line. The blazing condition is realized when the curve for fixed m cross the zero value. The plot is obtained for $\lambda = 532$ nm and $d = 13.68\sqrt{2}$ μm.

where m is the diffraction order, λ is the wavelength of the impinging light, d is the spacing of the grating, θ_i is the incident angle and θ_m the reflation angle, respect to the DMD surface's normal $\hat{n}_s$, as depicted in Fig. 3.2.

But in a DMD mirrors are tilted from the device's surface plane, and this angle has to be taken into account to find the blazing condition. Let indicate the angles measured respect to the normal of the mirror plane $\hat{n}_m$ with the Greek letter ϕ, as in Fig. 3.2, just to distinguish them from the θ angles taken respect to the DMD surface's normal. The two class of angles can be connected by the relation: $\theta = \phi - 12°$, because of the mirror's tilt angle.

Fixed the incident angle of the laser beam, the blazing condition for the device is achieved when each mirror reflects the light in a single diffraction order m of the whole diffraction grating. Formally that means that the angles must satisfy this condition:

$$\theta_m = \theta_r, \text{ where } \theta_r = \phi_r - 12°. \tag{3.2}$$

Combining this request with the grating equation, one finds that the blazing condition is achieved when the following relation is satisfied:

$$\arcsin\left(\frac{m\lambda}{d} - \sin\theta_i\right) + \theta_i + 24.° = 0. \tag{3.3}$$

The first member of the equation can be seen as a function of θ_i and studied for several m, looking for a zero.

The blazing condition for our case has been explored, studying the function of θ_i on the left side of equation (3.3) for several diffraction orders. The result are shown in Fig. 3.3, where the function of θ_i is plotted for many values of the diffraction order m for

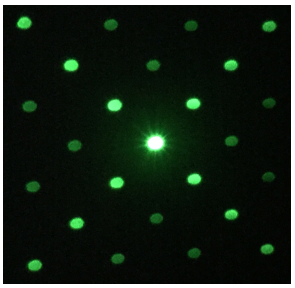

Figure 3.4: Picture of the several diffraction orders reflected from the DMDM when it is illuminated with a 532 nm laser beam. Note that the DMD acts like a two-dimensional diffraction gratings creating diffraction orders not in only one direction. Furthermore, the picture shows the achievement of the blazing condition: the central order is much more illuminated than the surrounding others.

Diffraction Order	Power Efficiency
0	61.5%
1	5.2%
2	2.1%
3	1.8%

Table 3.1: Power efficiency of different diffraction order.

$\lambda = 532$ nm and $d = 13.68\sqrt{2}$ μm, because the DMD mirrors are tilted respect to their diagonal. The graph shows that there are at least 6 diffraction orders (from $m = -2$ to $m = -7$) that satisfy the blazing condition. Among all these possible solution, the best one is the one that admit the lowest value for reflection angle $\theta_r = -\theta_i - 24$. A lower θ_r means indeed that the plane where the DMD surface lies is almost orthogonal to the propagation direction of the reflected light. This characteristic is useful to avoid aberration and distortion in the image of the DMD made by an imaging setup aligned in the selected order.

In our case the best configuration is the $m = -7$ order of diffraction that provides a reflection angle $\theta_r \simeq 8^\circ$ with an incident angle $\theta_i \simeq 32^\circ$. In practice, this blazing condition is realized positioning the DMD with almost the correct angle, and then changing the incident angle until one diffraction order is much more illuminated than the others. This situation is illustrated in Fig. 3.4: here several diffraction orders are illuminated but is clear that the central one is brighter than the others. We note that the diffraction orders are tilted by an angle of 45° from the horizontal because of the tilt of the DMD support, as illustrated in Fig. 3.1.

To verify the validity of the blazing condition realized, the efficiency of the light reflected in the different order of diffraction has been measured, obtaining the results recorded in Tab. 3.1. In this table the value of the diffraction order are taken respect to the blazed configuration shown in Fig. 3.4: the central spot is indicated as the 0 diffraction order and the others are counted moving on the diagonals. The power efficiencies are obtained measuring the light power in the different orders far enough

from the DMD so that the orders are sufficiently separated. Such values are then compared to the power of the impinging light to estimate the efficiency. In particular, for the 7th order used we have a power efficiency of 61.5%.

3.3 Optical Setup

The optical setup used to characterize the arbitrary optical potentials created by the DMD is shown in Fig. 3.5.

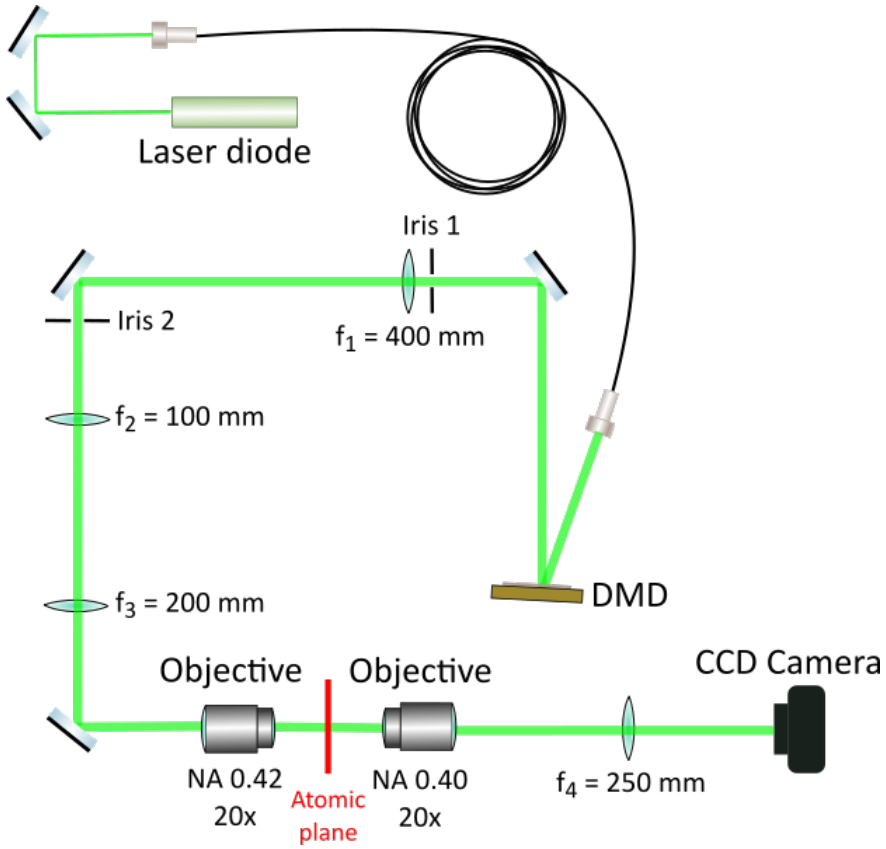

Figure 3.5: DMD optical setup

The laser source used is a 532 nm laser diode. The light emerging from the diode is sent to the DMD setup via an optical fiber, so that the working mode is the Hermite-Gauss $TEM_{0,0}$ mode. After the fiber the laser beam is collimated by a collimator with a waist of about 5 mm, and then sent to the DMD. This device reflects the light approximately in the orthogonal direction to the DMD plane thanks to the blazing condition already mentioned. The 7th diffraction order we need is selected by an iris, in Fig. 3.5 indicated as Iris 1.

The subsequent optical scheme is used to image the DMD plane into the atomic plane, demagnifying the image created by the DMD so that the size of the optical potential felt by the atoms is comparable to the dimensions of the atomic cloud. A first stage of demagnification is realized by a telescope, that decreases the size of the image of a factor of about 4. The telescope is composed by two lens with focal length

of $f_1 = 400$ mm and $f_2 = 100$ mm at distance of 50 cm, and is coupled with an iris placed in the focus of the first lens. The aperture is used as a spatial filter of the image, as it cuts the high frequency components in the Fourier domain, as it will be discussed in Sec. 3.4.1.

The DMD image is further demagnified by a Mitutoyo Plan Apo microscope objective and its tube lens with $f_3 = 200$ mm focal length. The objective is infinity corrected and provides a demagnification of 20×, with a working distance of 29 mm. The overall demagnification of the system is thus of about 80×, which means that the image after the objective is too small to be resolved by an usual CCD camera. The CCD camera used in this work is a Thorlabs CMOS DCC1645C camera, with pixel dimension of 5.2 μm. A full-screen image on the DMD with dimension of about 1 cm is reduced to 125 μm after the objective, so that only about 20 CCD pixels would be illuminated. That's why another objective with its tube lens of $f_4 = 250$ mm focal length is used after the first one. The second objective is a Zeiss LD Achroplan infinity corrected objective, with a magnification of 20× and working distance of 10.2 mm. This objective is positioned at a distance of about 4 cm from the previous one. The image emerging from the objective tube lens is finally observable with the camera, thanks to the magnification of 20× by the second objective.

In conclusion, the telescope and the first objective image the DMD plane into the atomic plane, applying a demagnification of 80×, while the second objective image the atomic plane onto the CCD plane, with a magnification of 20×.

3.4 Static Optical Potentials

With the optical system described in the previous section, static optical potentials can be realized and characterized. In particular, I focused my attention on two main properties of a DMD-made light pattern: the smoothness of the image edges and the homogeneity of the image bulk. On one hand, smooth potentials are useful to trap the atoms without any abrupt change in their energy. On the other hand, homogeneous potentials are important if one wants to have the same physical condition in all the atomic cloud. The scope of this section is to explain how a smooth and an homogeneous optical potential can be created with a DMD.

As already mentioned, the state of a single mirror of the DMD is binary. That means that only black and white image can be reproduced by a DMD, no gray-scale is accessible. To overcome this limit one can use dithering algorithms, like the Floyd-Steinberg one [55], that create a synthetic gray-scale using only black and white pixels. Therefore, using dithering algorithms it is possible to create a smooth potential. However, the aim of this thesis work was not to explore the fascinating field of image processing, but rather to probe and understand the capability of an optical imaging system. Therefore, smoothness is achieved in an optical way, using a spatial filter, as it will be illustrated in 3.4.1.

On the other hand, all the black and white images sent to the DMD are homogeneous, but we cannot say the same for the imaged light pattern on the atomic plane.

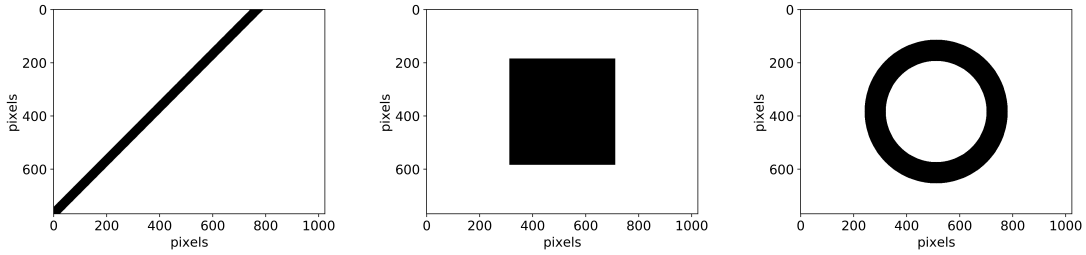

(a) Stripe DMD image **(b)** Flat-top DMD image **(c)** Torus DMD image

Figure 3.6: DMD image used to characterize static optical potentials.

Indeed, the Gaussian profile of the impinging beam has to be considered: the light pattern emerging from the DMD will keep part of the Gaussian shape of the input beam, that has to be removed to achieve a really homogeneous potential. For this purpose I wrote a feedback program for the DMD image, as it will be described in 3.4.2.

Regarding static potentials, I focused my attention in three different geometries: a barrier, a flat-top and a ring potential. The first one has been used to characterize the smoothing properties of the spatial filter, that are much more clearly observable with tiny structures. On the other hand, the large constant black area of the flt-top makes it particularly useful to study the capability of the setup to reproduce an homogeneous pattern. Finally, the ring potential has been characterized for its interesting application in experiments with atomic superfluids, as already discussed in Chapter 1. The DMD images used to realize such potentials are shown in Fig. 3.6. The barrier DMD image consists in a stripe of black pixels tilted by an angle of 45°, so that the light stripe emerging from the DMD is vertical. The width of the stripe is about 70 pixels, that correspond to 12 μm in the atomic plane. The flat-top pattern is obtained with a square with side of 400 pixels, that correspond to 68.4 μm on the atomic plane. Finally the ring image has a radial thickness of 79 pixels, that correspond to 2.3 μm on the atomic plane. These dimensions have been chosen to be comparable with those requested in typical atomic superfluids experiments, but can be changed at will.

3.4.1 Spatial Filtering

As already mentioned in Sec 3.3, the first telescope of the optical system is coupled with an iris used as a spatial filter. In this section I will explain in details the operating principle of this tool.

The spatial filtering is performed by the iris thanks to the Fourier transforming properties of lenses. To understand how, let consider the system illustrated in Fig. 3.7. An input image is placed at distance d in front of a converging lens of focal length f. The input image is a monochromatic plane wave, with amplitude $U_0(x, y)$, where x and y are coordinates in the normal plane respect to the light propagation direction. In our case the dependency on x and y of the plane wave electric field is created by the DMD: $U_0(x, y)$ depends on the mirrors tilt position, that is fixed by the matrix sent to the DMD. Therefore, we can say that $U_0(x, y)$ is the amplitude function of the image in

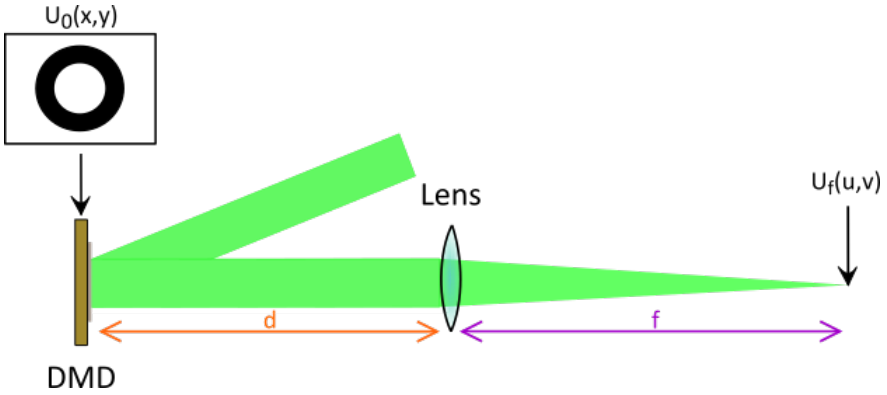

Figure 3.7: Illustration of the Fourier transforming properties of a lens.

the DMD plane, namely in Fig. 3.7 it has a ring shape. Such a plane wave propagates towards the lens, that focuses the image at distance f. It can be demonstrated [56] that the electric field in the lens focus is proportional to the Fourier transform of the input field:

$$\mathcal{F}[U_0] = F_i(f_x, f_y) = \frac{1}{\sqrt{2\pi}} \int_{-\infty}^{+\infty} \int_{-\infty}^{+\infty} U_0(x, y) \exp^{-i(f_x x + f_y y)} \, dxdy. \tag{3.4}$$

In particular, when the lens is placed at a distance equal to its focal length from the input image, namely $d = f$, the electric field in the lens focus is:

$$U_f(u, v) = \frac{F_i(u, v)}{i\lambda f}. \tag{3.5}$$

Therefore, the electric field in a lens focus is straight proportional to the Fourier transform of the input electric field. That is, a converging lens perform the two-dimensional Fourier transform of the electric field in input.

Going back to the DMD setup in Fig. 3.5, the first lens of the telescope is positioned at a distance f_1, equal to its focal length, from the DMD, while the spatial filtering iris is located in correspondence of the first lens focus. Here the electric field is proportional to the Fourier transform of the image sent to DMD, so the iris cuts the high frequency of the DMD image. In this sense the iris works as a spatial filter: it cleans the DMD image from the high frequency components, smoothing its intensity profile.

To verify this behaviour, an image with well-known frequency has been created. Such image, depicted in Fig. 3.8 (a), is composed by a sum of 1000 sinusoidal functions in the horizontal direction with fixed frequency, rounded to obtain a black and white image. This pattern is sent to DMD, and the image created after the telescope is observed with the CCD Camera for several iris diameter. The light pattern is observed before the two objective to see more clearly the effect of the spatial filter. The first objectives introduces indeed another frequency cut because of its small aperture of 5.6 mm, while all the previous optics have a diameter of $2''$. The results are shown in Fig. 3.8: we can see that decreasing the diameter of the aperture only the lower frequency remain.

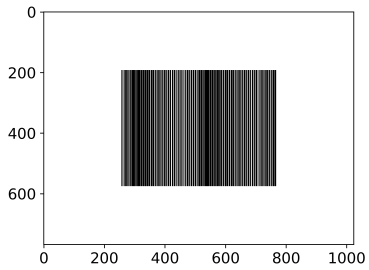

(a) DMD image

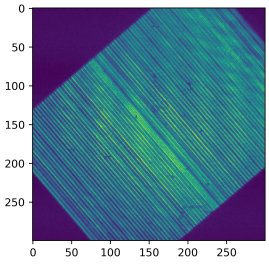

(b) Iris wide open

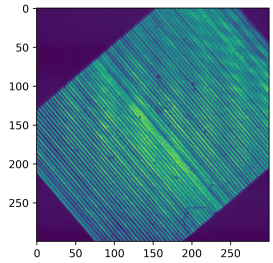

(c) Iris diameter of 4 mm

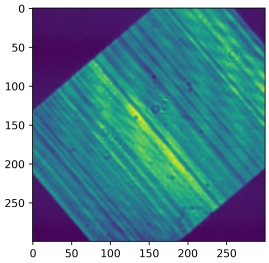

(d) Iris diameter of 2 mm

Figure 3.8: Effect of the spatial filter for several iris diameter.

The spatial filter has been then tested with the barrier image of Fig. 3.6 (a). In this case the high frequency cut results in a smoothing of the light pattern, as reported in Fig. 3.9. Here, the horizontal profile of the light pattern is plotted for the two extreme iris diameter, namely the iris wide open and with a diameter of 1 mm. These horizontal profiles are obtained integrating the image acquired with the CCD camera over 40 rows in the central part of the barrier.

In conclusion, the spatial filter is a very useful optical tool to realize smooth potentials on the atom cloud, starting from a black and white image on the DMD.

3.4.2 Feedback Program

The necessity to write a feedback program for the DMD image starts from the fact that the light profile on the atomic plane would never be the same as in the DMD image. This is mainly due to two reasons: the not-uniform intensity profile of the input beam and the presence of defects on the imaging system.

As already mentioned, the Gaussian profile of the incoming beam affects the image created by the DMD. This is because the DMD acts like a light mask: where the mirrors are ON it reflects the light without changing its intensity profile. Therefore, if a flat-top image is sent to the DMD, the light emerging from the device will keep the Gaussian profile of the reflected portion of the incoming beam. On the other hand, defects on the optical imaging system can create imperfections in the image on the atomic plane, like dark region in the light pattern created by flecks of dust.

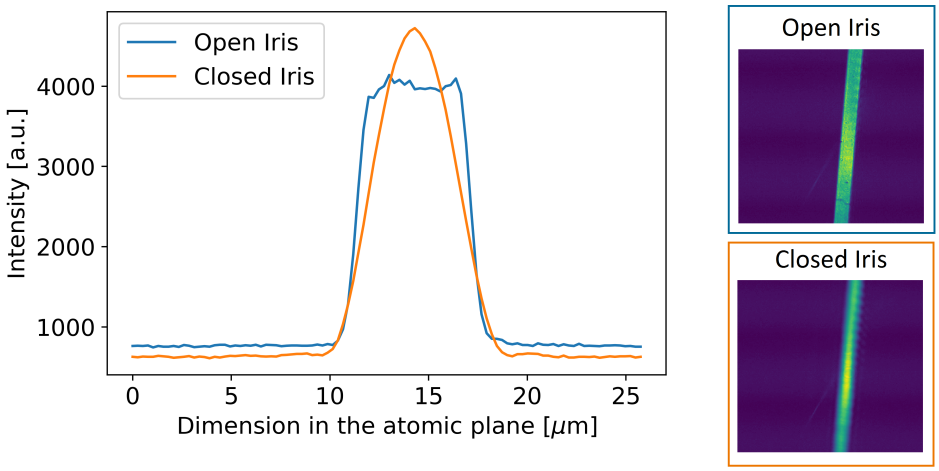

Figure 3.9: Horizontal profile of an optical barrier with and without the spatial filter. The profile is obtained integrating the image acquired with the CCD over 40 rows. A section of the CCD image analyzed is reported in the lateral box, for the two considered iris diameter.

The feedback program that I wrote corrects these two issues, realizing on the atomic plane a light pattern that is closer to the desired one. The feedback program operates like a PI controller: the image created by the optical system on the CCD is acquired and compared to the target image of the light pattern we want to reproduce. The pixel-by-pixel error matrix, i.e. the difference between the two, is calculated and then summed to the previous DMD image, weighted by a proportional and an integral coefficient. This new image is sent to the DMD and the process is iterated as long as the difference between the acquired and the target images is not sufficiently low.

In order to compare the acquired and the target image, a transformation has to be done to the first one. The image on the CCD plane is indeed tilted by an angle of 45° because of the DMD support tilt, and smaller than the target image because of the demagnification of the optical system. Therefore, before the feedback process it is necessary to calibrate the DMD on the CCD. This process is described in details in the next section.

Calibration of the CCD image

The calibration of the DMD in the CCD image is achieved through an affine transformation of the image acquired. Affine transformations are functions between matrices that preserve point, strait lines and planes, so that parallel lines remain parallel after the transformation. In our calibration case the wanted transformation involves a rotation and a scaling, both operations within the class of affine transformations.

In particular, the calibration program operates as illustrated in Fig. 3.10: an image with three point of 20 pixel diameter is sent to DMD (a) and acquired with the CCD camera (b). The coordinates of the three point in such CCD image is revealed by a two-dimensional Gaussian fit. Then, the affine transformation matrix is defined by the `getAffineTransform` function of the Open-CV Python module, using the

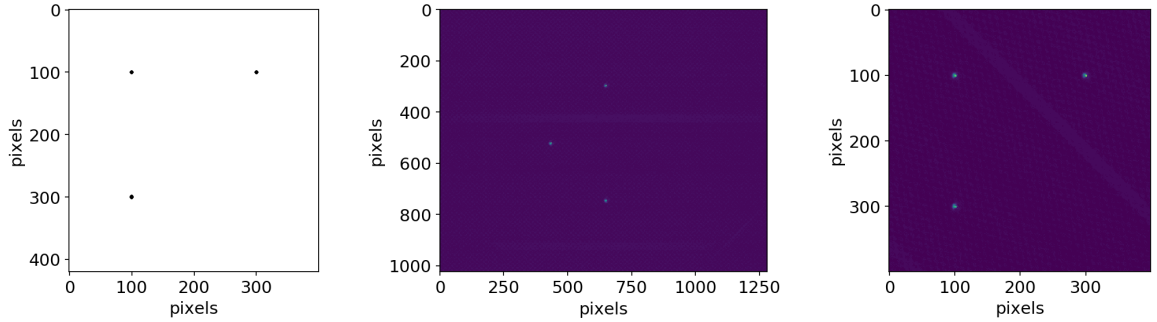

(a) Calibration image sent to DMD

(b) Acquired image before the calibration

(c) Acquire image after the calibration

Figure 3.10: Illustration of the calibration process: in (a) the DMD image used for the calibration is reported, (b) shows the image of (a) as acquired by the CCD, in (c) the affine transformation of (b) is reported. We note that (a) and (c) images show a limited area of the DMD screen,the same square of 400 pixels side that is used in Chapter 4

coordinates of the points in the CCD image and their well-known position in the input image on the DMD. This matrix can be then applied to the acquired image using the Open-CV `warpAffine` function. The resulting matrix can be set to have the same dimensions of the DMD image, namely a 768×1024 array, so that it can be compared to the image sent to DMD, as requested in the feedback program. We note that (a) and (c) images show a limited area of the DMD screen, the same square of 400 pixels side that is used in Chapter 4. The calibration procedure in the two cases is the same, just the used DMD screen area is different: for the feedback program we use all the 1024×768 array of pixels, whereas a reduced area is considered in Chapter 4.

Feedback process

Once obtained the affine transformation matrix from the calibration process, it is used in the feedback program. The feedback program is mainly composed by an iteration, where the error between the target image and the acquired one is estimated, and the input image on the DMD is modified to reduce such error. To do that, the program applies the pixel-by-pixel error matrix to the DMD image. The error matrix E_n for the n-th iteration is simply obtained by the difference between the target and the acquired image, once transformed by the affine transformation matrix A:

$$E_n = T - A \times CCD_n, \tag{3.6}$$

where T and CCD_n are the matrix corresponding to the target image and to the image acquired in the n-th iteration respectively.

Two kinds of correction can now be used, as in a PI controller: a proportional and an integral one. The proportional correction acts simply adding to the previous DMD image the error matrix E_n weighted by the a coefficient k_P. On the other hand, the integral correction is set to keep memory of the past corrections: it adds the sum of

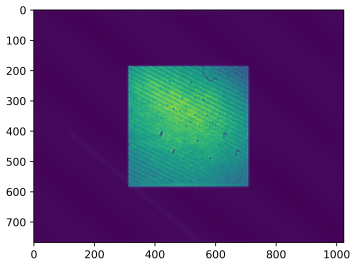

(a) Flat-top profile without the feedback program

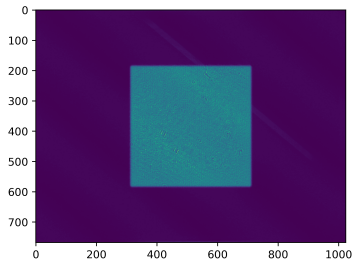

(b) Flat-top profile with the feedback program

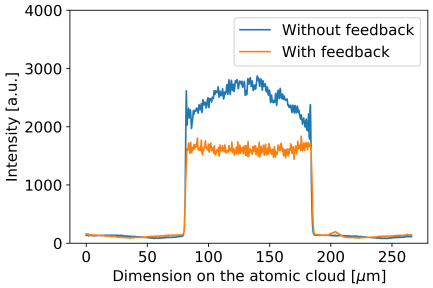

(c) Horizontal profile with and without the feedback program

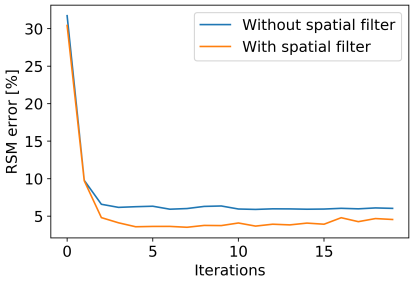

(d) RMS error with and without the spatial filter

Figure 3.11: Effects of the Feedback program on the flat-top profile.

all the error matrix already evaluated to the DMD image, weighted by a coefficient k_i. Finally, another kind of correction can be introduced to the feedback program. This is a fast correction that add to the DMD image the error matrix raised to the 3rd power and weighted by a coefficient k_{p3}. Such fast correction has never been used in this work, but can be useful when the program is requested to correct the image in only few iterations. Therefore, the new DMD image evaluated in the n-th iteration, DMD_{n+1}, is obtained as:

$$DMD_{n+1} = DMD_n + k_p E_n + k_i \sum_{m=0}^{n} E_m + k_{p3}(E_n)^3, \tag{3.7}$$

The DMD_{n+1} image is sent to the DMD and the procedure is repeated in the consecutive iteration. Furthermore, in each iteration the RMS error is evaluated:

$$RMS = 100 \sqrt{\sum_{(i,j)} \left(\frac{CCD[i,j] - T[i,j]}{T[i,j]} \right)^2 \frac{1}{RC}}, \tag{3.8}$$

where $R = 768$ is the number of rows in the DMD matrix and $C = 1024$ the number of columns. The sum over the two matrices elements is restricted to the region where the target image is non zero, otherwise the error is saturated by the background noise and the effect of the feedback program on it cannot be seen.

As a first step, the feedback parameter k_p and k_i has been optimize to achieve the lower RMS error in the minimum number of iteration, using the flat-top profile as

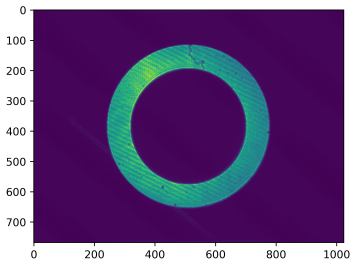

(a) Torus profile without the feedback program

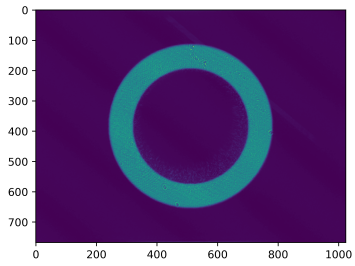

(b) Torus profile with the feedback program

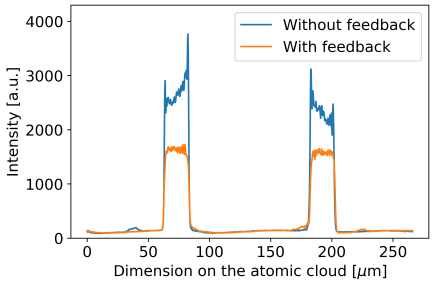

(c) Horizontal profile with and without the feedback program

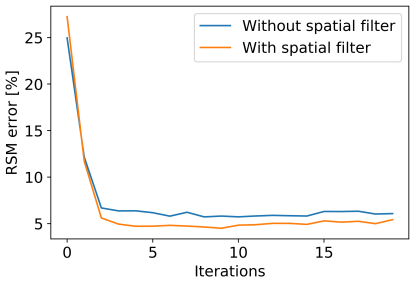

(d) RMS error with and without the spatial filter

Figure 3.12: Effects of the Feedback program on the toroidal profile.

the target image. Then, the feedback program has been tested with the ring profile too. The results are shown in Fig. 3.11 and 3.12. The (a) and (b) images show the light profile in the CCD plane without feedback and after 20 steps of feedback process respectively. We can see that the light profile in (b) is much more homogeneous than the one in (a) for both geometries. In particular, the feedback program is capable to correct bot the Gaussian profile of the impinging beam and the imperfections in the light profile due to defects in the optical setup. In Fig. 3.11 and 3.12 (c) is then plotted the horizontal profile integrated over 40 rows of the two images to see more clearly the feedback effect. We see that for the corrected image the intensity is reduced, but almost constant. To achieve an homogeneous profile indeed not all the DMD mirrors in the light part of the image are ON: the feedback program modulates the density of ON mirrors to achieve the corrected image. Finally, in Fig. 3.11 and 3.12 (c) the trend of the RMS error over several iteration is reported. Here, two lines are plotted, corresponding to a feedback process done with and without the spatial filter illustrated in 3.4.1. We see that the spatial filter reduce the RMS error, because without the high frequency components the corrected image is smoother, and so more similar to the target one. Furthermore, we note that the number of iterations required to achieve the stable state for the corrected image is quite the same for both case: less than 5 iterations are required to achieve an RMS error around 5%. In particular, for the flat-top pattern the minimum RMS is achieved in the 11th step with the value of 5.90% without the feedback and in the 7th step with the value of 3.52% with the spatial filter.

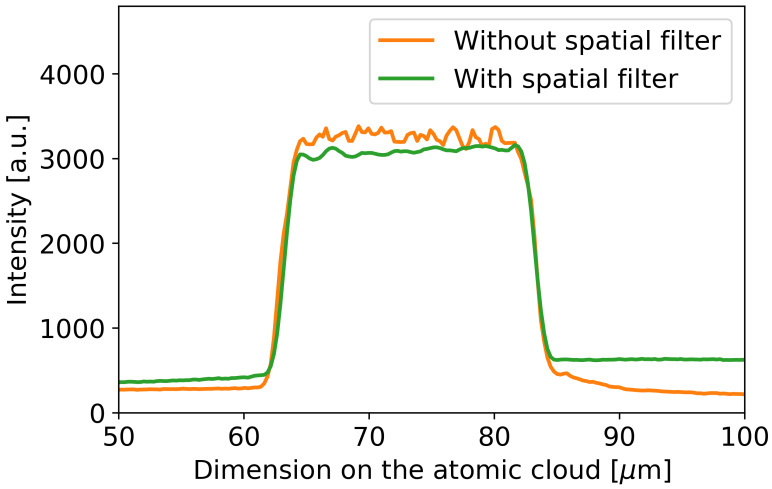

Figure 3.13: Comparison between the horizontal profile of the ring potential, integrated over 40 rows, at the end of the feedback process with and without the smoothing action of the spatial filter. The spatial filter extremely reduce the intensity fluctuations in the light pattern.

For the ring patter these value are instead 5.72% in the 8th step and 4.50% in the 9th step respectively.

Fig. 3.13 shows a comparison between the horizontal profile of the ring potential, integrated over 40 rows, at the end of the feedback process with and without the smoothing action of the spatial filter. We can see that with the spatial filter, the fluctuations in intensity are extremely reduced. In particular, only residual fluctuations of 1.4% over a length scale of about 5 μm remain in the image after the feedback process with the spatial filter. Such length scale is bigger than the healing length of an atomic superluid, that for rubidium is about 200 nm, so that for what concerns the atomic motion, the optical potential created by such light profile is seen as homogeneous.

In conclusion, with the feedback program I developed in this thesis work it is possible to create arbitrary light pattern that differ from the target image only few percentage points. In particular, with this tool we can obtain homogeneous potentials, and their homogeneity is increased by the spatial filter.

3.5 Time-Dependent Optical Potentials

A sequence of images can be loaded into the DMD memory and then displayed at a fixed frequency to obtain a time-dependent light pattern. In particular, with the ALP4lib Python Module [53] this is achieved with three different functions. The `SeqAlloc` function allocate memory on the DMD board RAM for the desired sequence of images. Such sequence can be then loaded on board with the `SeqPut` function, using the memory previously allocated. Finally the timing properties of the sequence can be set using the `SetTiming` function. The latter has two main entries to fix the frequency of the image sequence to display: `IlluminationTime` fixes the display time of a single

image of the sequence, while `pictureTime` sets the time between the display of two consecutive image. Therefore, the dark time between the display of two consecutive pictures is fixed by the difference between these two parameter.

In this thesis work two main kinds of time-dependent light patterns have been studied: the translation and the rotation of a starting image. A sequence of image resembling these two situation is easily obtained using the geometric transformation functions available in the Open-CV python module. Now, the properties of such moving images on the atomic cloud has to be determined. In particular, it is interesting to compare the velocity of a time-dependent obstacle with the sound speed of the atomic superfluid. As already mentioned in Chapter 1, typical sound speed are in the order of mm/s for an atomic superfluid. The DMD can then be used to realize a time-dependent potential suitable for experiment with atomic superfluids if the display velocity it can achieve is in the order of mm/s. Let then examine the two time-dependent light pattern separately.

For the translational motion we can consider a cluster of ON pixels moving along a row of the DMD screen. The motion cannot be continuous because pixels are discrete unit. The best we can do is to make the change of position of the cluster between two consecutive image as little as possible. In this way the discrete jump of the potential felt by the atoms is less sudden. Consider thus a sequence of images where the position of the cluster vary of only one DMD pixel between two consecutive frame. The velocity of such cluster can be evaluated as:

$$v = \frac{\Delta s}{\Delta t}, \tag{3.9}$$

where $\Delta s = 1$ px is the change in position between two consecutive images and Δt is the time between the display of the two. In our case $\Delta t = 1/f$, where f is the display frequency of the image sequence, that can be set with the `SetTiming` function. We are interested in the maximum velocity achievable with the DMD, so the maximum switching rate of the device has to be considered. For the DMD used in this work, this is $f^{max} = 22.727$ kHz. To evaluate the actual velocity of the potential felt by the atoms, we need to consider the change of position of the light pattern in the atomic plane. That is:

$$\Delta s_{atoms} = \frac{1\text{px} \times 13.68\ \mu\text{m}}{M}, \tag{3.10}$$

where M is the demagnification operated by the imaging system and 13.68 μm is the DMD mirrors dimension. Therefore, the maximum velocity achievable with the DMD is:

$$v^{max} = \Delta s_{atoms} f^{max} = \frac{310.9\ \text{mm/s}}{M}. \tag{3.11}$$

That is, the maximum velocity depends on the demagnification of the optical system. In particular, with the demagnification of 80$\times$ operated by the optical system described in Sec. 3.3 the maximum velocity is $v^{max} = 3.8$ mm/s. For the imaging system used to realize high-resolved optical potential described in the next Chapter, the demagnification operated is 20$\times$, so the maximum velocity is $v^{max} = 15.5$ mm/s. In both cases

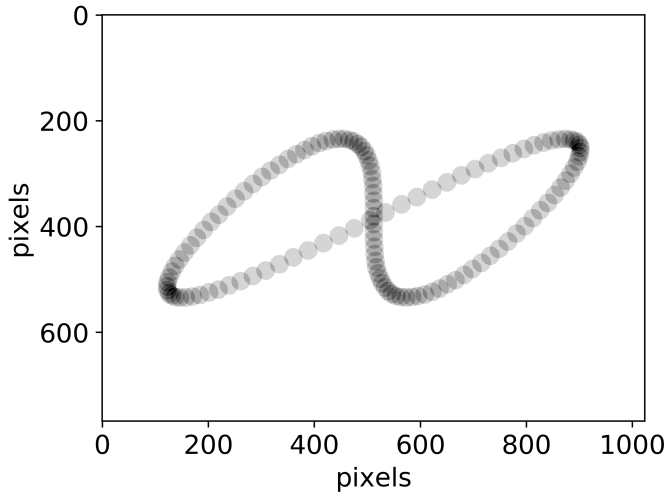

Figure 3.14: Illustration of the figure-8 trajectory of a light obstacle.

the maximum velocity is of the right order of magnitude. Anyway, this value can be increased by using an higher change in position between two consecutive image of the sequence.

Let now consider a sequence of image where a cluster of ON mirrors is rotated around a fixed point. Again, we want to evaluate the maximum velocity of such a cluster achievable with the DMD. Also this motion is limited by the non continuity of the pixels in the DMD image, which now translates to a constrain in the rotation angle $\Delta\theta$ between two consecutive images on the sequence. $\Delta\theta$ has to be such that the change in position of the cluster is as little as possible, namely equal to one pixel. For a circular trajectory of radius R we obtain: $\Delta\theta = 1\ \text{px}/R[\text{px}]$. Now we can estimate the maximum angular frequency achievable with a DMD:

$$\omega^{max} = \frac{\Delta\theta^{max}}{\Delta t^{min}} = \Delta\theta^{max} f^{max} = \frac{22.727\ \text{kHz}}{R[\text{px}]}, \tag{3.12}$$

that correspond to a radial velocity:

$$v_r^{max} = \omega^{max} R' = \omega^{max} \frac{R}{M} = \frac{310.9\ \text{mm/s}}{M}, \tag{3.13}$$

where $R' = R/M$ is the trajectory radius measured in the atomic plane. Therefore, we obtain the same results as before.

These calculations demonstrate that the DMD can be certainly used to create time-dependent optical potentials suitable for experiments with atomic superfluids. In addition to the translational and rotational motion of a cluster of pixels studied in this section, other exotic geometries can be implemented.

As a test, the figure-8 path for a circular obstacle studied in [57] has been realized. As demonstrated in [57], if the light is blue detuned from the main atomic resonance, this time-dependent potential is an efficient way to generate a large number of vortices in the atomic superfluid. In particular, the figure-8 geometry is useful to create a vortex tangle due to its minimal net transfer of angular momentum.

An illustration of the DMD realization of such time-dependent profile is reported in Fig. 3.14. Here, the positions of the moving obstacle are represented all together in the same image to see more clearly its trajectory, but to create the desired excitation of the superfluid each frame of the sequence will keep only one spot. The coordinates of the obstacles are given by:

$$x(t) = x_0 \cos(\nu_L t)[1 - \sin(\nu_L t)] \quad , \quad y(t) = y_0 \cos(\nu_L t) \sin(\nu_L t) \tag{3.14}$$

where $x_0 = y_0 = A$ is the amplitude of the figure-8 path and ν_L its frequency. The light obstacle is created with a circular light pattern with diameter of 30 px, that correspond to 5.13 μm in the atomic plane, whereas the amplitude of the curve is 300 px, namely 51.3 μm in the atomic plane. These dimensions have been chosen to create a more evident light pattern in Fig. 3.14, but can be changed at will to achieve the requirement of an atomic superfluids experiment. Also the timing properties of the sequence can be set to be the same as in [57]. Specifically, a figure-8 path frequency of $\nu_L = 0.74 \times 150$ Hz used in [57] corresponds to a switching rate of about 2 kHz for the DMD.

Chapter 4

Highly-resolved Optical Potentials

In this chapter I present the possibility to create optical potentials on the length scale of a μm, comparable to the resolution of the optical system, with the DMD. To do so, I used a different optical setup than the one presented in the previous chapter, as a lower demagnification is requested to be able to resolve the light pattern imaged on the atomic plane with the CCD.

The first part of this chapter is dedicated to the study and measurement of the resolution of the optical system. In particular, in Sec. 4.1 the theory of image formation in an optical system is briefly illustrated, then a numerical simulation of the expected point spread function of the optical setup used is presented. Successively, I propose a DMD-based method to measure the size of the point spread function of the system and report the results of the application of such method. In Sec. 4.2 I present the capability of the optical system to realize disordered potentials on the length scale of its resolution, namely of the order of μm. In particular, two different kinds of disordered pattern have been studied: speckles and point-like disorder. Their statistical properties are illustrated and then a characterization of the disordered potentials created with the DMD is performed.

4.1 Measurement of the resolution of an optical system with the DMD

To create highly-resolved optical potentials it is necessary to know the resolution of the optical system. In Sec. 4.1.1 the theory of image formation is briefly summarized in, in order to understand the role of the Point Spread Function (PSF), namely the response of the system to a point source illumination. Then, in Sec. 4.1.2 the DMD setup used to create highly resolved potentials is presented and the PSF of such system is numerically evaluated in Sec. 4.1.3. Finally, the PSF measurement technique developed in this work is presented in Sec. 4.1.4: the DMD is used to generate a grid of point sources, that are processed by the optical system and observed afterwards by means of a CCD. The dimensions of such point source images provides information about the PSF and allow to identify the possible aberrations of the optical system.

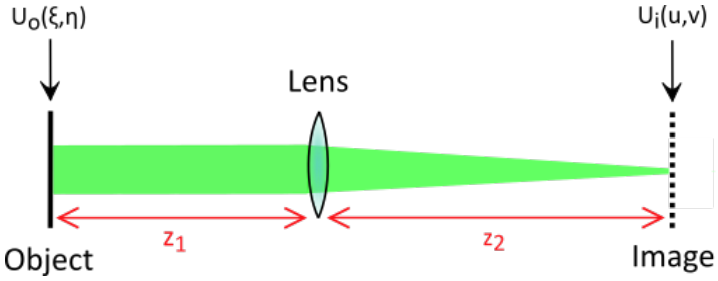

Figure 4.1: Illustration of the process of image formation performed by a lens of focal length f.

4.1.1 Theory of image formation

If we put an object in front of a lens and illuminate it, under the appropriate conditions a distribution of light intensity that closely resembles the object will appear across a second plane beyond the lens. This is what we call the image formation capability of lenses.

To illustrate the process of image formation in detail, we consider first a planar object placed at distance z_1 in front of a positive aberration-free lens with focal length f and illuminated by monochromatic light, as depicted in Fig. 4.1. If we neglect the polarization of the electromagnetic field, we can treat it as a scalar field. In particular, we call $U_o(\xi, \eta)$ and $U_i(u, v)$ the amplitude of the electric field of the object and of the image observed at distance z_2 beyond the lens respectively. The latter one can be expressed as :

$$U_i(u, v) = \int_{-\infty}^{+\infty} \int h(u, v; \xi, \eta) U_o(\xi, \eta) d\xi d\eta, \tag{4.1}$$

where $h(u, v; \xi, \eta)$ is the impulse response or Point Spread Function (PSF) of the lens. We note that Eq. (4.1) is valid for all imaging systems, because of the linearity of the wave propagation phenomenon. The PSF correspond to the electric field amplitude produced at coordinates (u, v) by a point source placed in coordinates (ξ, η) in the object plane. Therefore, all the properties of an imaging system are specified by the PSF. In particular, the image is as much similar to the object as the PSF is:

$$h(u, v; \xi, \eta) \approx K\delta(u \pm M\xi, v \pm M\eta), \tag{4.2}$$

where K is a complex constant, M is the magnification of the optical system and the $\pm$ indicates the possibility of an image inversion.

We can find the PSF of an optical system by considering a point source at coordinates (ξ, η) as the object and calculating the amplitude of the image electric field $U_i(u, v)$ produced by the lens. Following [56], it can be demonstrated that the PFS can be expressed as:

$$h(u, v; \xi, \eta) = \frac{1}{\lambda^2 z_1 z_2} \int_{-\infty}^{+\infty} \int_{-\infty}^{+\infty} P(x, y) \exp\left[-i\frac{2\pi}{\lambda z_2}\left((u - M\xi)x + (v - M\eta)y\right)\right] dxdy, \tag{4.3}$$

where $P(x, y)$ is the pupil function of the lens, defined to be unitary inside the lens, and null elsewhere. To obtain Eq. (4.3), some approximations have been done. In particular, the paraxial approximation to consider only rays near the optical axis and the lens law $\frac{1}{z_1} + \frac{1}{z_2} - \frac{1}{f} = 0$ permit to simplify considerably the PSF expression.

Now we can use the PSF expression of Eq. (4.3) in Eq. (4.1) to find the profile of the image electric field amplitude. Using the variables change:

$$\tilde{\xi} = M\xi \ , \ \tilde{\eta} = M\eta \tag{4.4}$$

and defining $\tilde{h} = \frac{h}{|M|}$, the superposition integral in Eq. (4.1) translates into a convolution of function [56]:

$$U_i(u, v) = \tilde{h}(u, v) \otimes U_g(u, v) = \int_{-\infty}^{+\infty} \int_{-\infty}^{+\infty} \tilde{h}(u - \tilde{\xi}, v - \tilde{\eta}) U_g(u, v) d\tilde{\xi} d\tilde{\eta}, \tag{4.5}$$

where:

$$U_g(u, v) = \frac{1}{|M|} U_o \left(\frac{u}{M}, \frac{v}{M} \right) \tag{4.6}$$

is the geometrical optics prediction of the image when the optical system perform a magnification M. Therefore, Eq. (4.5) express the electric field amplitude of the image performed by a lens as a convolution between the PSF of the optical system and the geometric amplitude of the image. This is due to the diffraction only, no aberrations have been taken into account. The effect of diffraction thus leads to a smoothing operation that can attenuate the details of the object, limiting the resolution of the optical system.

In general, the results of Eq. (4.5) can be obtained also for composite imaging system, the only request for them is to be diffraction-limited, i.e. free from aberrations. In this case the PSF is expressed as in Eq. (4.3), where now $P(x, y)$ is the pupil function of the most limiting aperture of such system. Moreover, it is possible to find a more clear expression of the PSF noting that the integral in Eq. (4.3) is a Fraunhofer diffraction integral for a circular aperture. As reported in [56], it can be solved to obtain the Airy pattern:

$$\tilde{h}(u, v) = \frac{A}{\lambda z_2} 2 \frac{J_1(x)}{x}, \tag{4.7}$$

where A is a constant amplitude, J_1 is the Bessel function of the first kind of order 1 and $x = \frac{2\pi w r}{\lambda z_2}$, with $r = \sqrt{u^2 + v^2}$ and w is the radius of the most limiting aperture of the optical system.

4.1.2 Optical system

The DMD setup used to implement highly-resolved optical potentials is the one illustrated in Fig. 4.2. Here, all the optics are the same presented in Sec. 3.3, but the first telescope has been removed to decrease the demagnification performed in the atomic plane. Furthermore, the second objective is coupled with a different tube lens, in order to achieve a lower magnification of the image in the atomic plane. This is necessary to

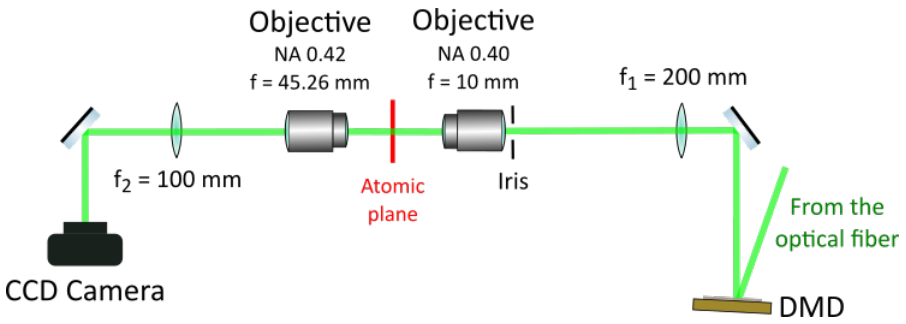

Figure 4.2: Optical setup used to create highly-resolved optical potentials.

have a smaller image of the DMD on the CCD, so that enough mirrors of the device are visible on the camera. In particular, the second objective perform a magnification of 11×, in this way the DMD screen is reduced by a factor 1.75 on the camera. With such demagnification of the whole optical system, the DMD screen is still too big to be completely observable with the CCD. Hence, for the further works only a square of 400 px side of the DMD screen is used, that corresponds to a region of 273.6 μm on the atomic plane. Another difference from the setup of Sec. 3.3 is that now a cage system has been used for the first part of the optical system, from the DMD to the first objective, to improve the stability of the alignment.

4.1.3 Point Spread Function of the optical system

First of all, the PSF of the optical system in Fig. 4.2 has been estimated using the results seen in Sec. 4.1.1 with a numerical simulation. The PSF is fixed by the most limiting aperture of the imaging system, and for the setup in Fig. 4.2 this is the first objective. It has indeed a numerical aperture of 0.28 and a focal length of 10 mm, that correspond to a pupil radius of 2.8 mm. Instead, the second objective has a higher pupil radius of 18.1 mm, because its numerical aperture of 0.40 and its focal length of 45.26 mm, and all the other optics used in the setup have a diameter of 2", that correspond to a larger pupil radius even in the case of mirrors that are tilted of 45°.

In the numerical simulation the PSF is evaluated using Eq. (4.7) and the first objective as the most limiting aperture, and the results is reported in Fig. 4.3 (a). The size of such function has been estimated with a two-dimensional Gaussian fit for convenience, as all the spot sizes in the rest of this section. In Fig. 4.3 (b) the central row of PSF matrix and of its two-dimensional Gaussian fit are plotted. In particular, from the fit we obtain $\sigma_x = \sigma_y = 0.523$ μm. Therefore, the size of the PSF is of $2\sigma = 1.046$ μm, that correspond to the resolution of the optical system: any light source with dimension lower than 1.046 μm on the atomic plane is seen as point-like by the optical system. Its image is thus dominated by the PSF, so that it cannot be resolved in detail.

It is particularly useful to compare the dimensions of one mirror of the DMD on the atomic plane with the size of the PSF, to understand if the optical system is capable to resolve single mirrors of the device. The side of 13.68 μm of a DMD mirror

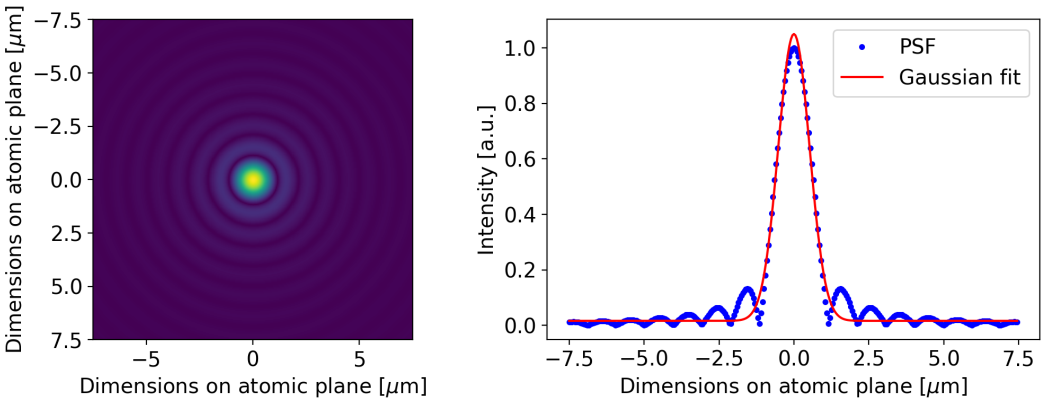

(a) Point Spread Function. **(b)** Gaussian fit of the PSF.

Figure 4.3: Point Spread Function of the optical system: in (a) such function is calculated using Eq 4.7 and a pupil radius of 2.8 mm. In (b) the Gaussian fit of the PSF is reported: to obtain the 1D plot the central row of the PSF and its two-dimensional Gaussian fit are considered.

is reduced by a factor of 20 in the atomic plane, so that here a single mirror has dimensions of 0.684 μm. Therefore, we expect that the image of a single mirror is completely dominated by the PSF of the optical system. To prove this statement, the image amplitude U_i of a single mirror object can be computed using Eq. (4.5) and the numerical expression of the PSF already estimated. Such process is illustrated in Fig. 4.4. In (a) the geometrical optics prediction of the image amplitude, calculated as in Eq. (4.6), is reported. Such matrix is convolved with the PSF of the optical system reported in Fig. 4.3 (a) to obtain the actual image amplitude in (b). We can see that the image of a single DMD mirror is completely dominated by the PSF, as expected. The size of such image has been estimated with a Gaussian fit: a two-dimensional Gaussian fit of the image in (b) is performed, and the central row of of the fitted and

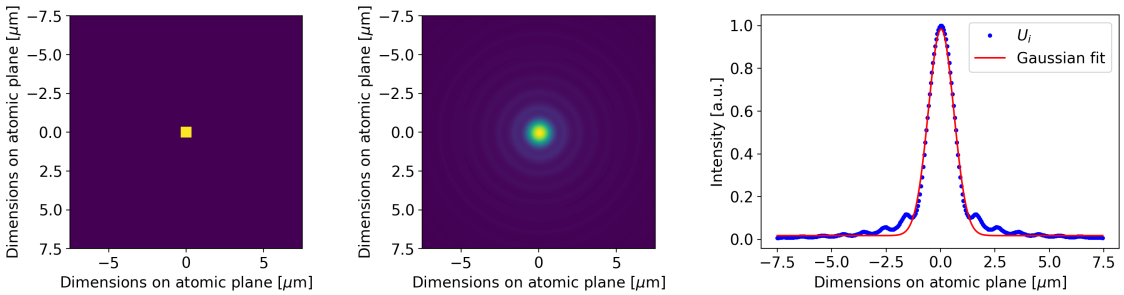

(a) Geometrical image U_g. **(b)** Image amplitude U_i **(c)** Gaussian fit of U_i

Figure 4.4: Calculation of the image of a single mirror of the DMD on the atomic plane. The geometrical optic prediction for the image U_g and the actual image amplitude U_i, numerically computed as the convolution of U_g with the PSF, are reported in (a) and (b) respectively. U_i is obtained by the convolution between the PSF and U_g, as requested by Eq. (4.5). In (c) the Gaussian fit of U_i is plotted.

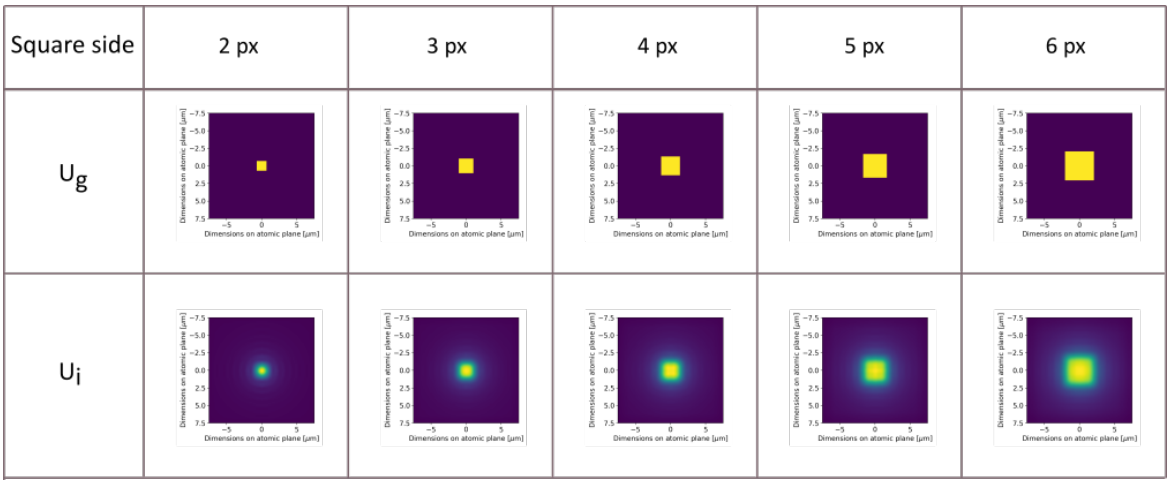

Figure 4.5: Comparison between the geometrical image U_g and the image obtained by the numerical convolution of U_g with the PSF of the optical system, for many square object of different size.

fitting image is plotted in (c). In particular, from the two-dimensional fit we obtain $\sigma_x = \sigma_y = 0.583$ μm, almost the same size of the PSF. This means that the image of single mirror cannot be well resolved by the optical system, that is not capable to reproduce the details of the image.

For bigger images on the DMD we expect that the effect of the convolution with the PSF will not be so severe. To prove this, the image of a square with side of few DMD mirrors on the atomic plane has been calculated from the convolution with the PSF. The results are reported in Fig. 4.5. We see that increasing the dimension of the object the image become more detailed, but still the smoothing effect of the PSF is visible even for the bigger object with a 6 mirrors size.

It is important to note that all the results obtained in this section are valid only for diffraction-limited imaging system. The presence of aberrations may modify the PSF of the optical system, distorting the image on the atomic plane.

4.1.4 Measurement of the resolution

From the numerical simulation of the previous section we understand that a single mirror of the DMD is seen as a point source by the optical system. Therefore, we can use a single mirror to measure the real PSF of the optical system and compare it to the results of the simulation. To do so, we need to switch on a single mirror in a fixed position of the DMD array and observe it with the CCD camera. Then, we can estimate its dimension with a Gaussian fit and compare the results with the size obtained with the simulation. The dependency of the PSF from the position on the DMD plane can be explored repeating these operations for several position of the ON mirror on the DMD mirrors array.

To increase the efficiency of the measurement, instead of scanning the DMD array mirror-by-mirror with many image acquisition of the CCD, a grid of single mirrors is

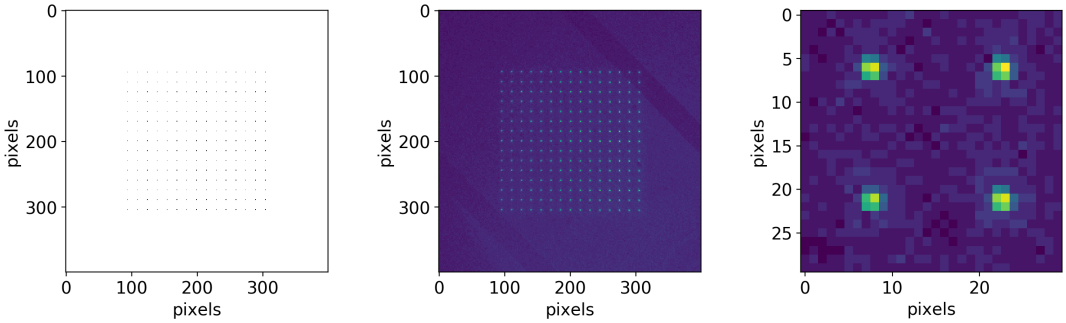

(a) DMD image. **(b)** Image on the CCD. **(c)** Detail of (b).

Figure 4.6: PSF measuring process with the DMD: a grid of single mirrors is switched on in the DMD (a) and then its image on the CCD is acquired. Such image is represented in (b), after the affine transformation to bring it back to the DMD dimensions. In (c) is reported a detail of (b): we see that the image of a single mirror covers just over 1 pixel.

switched on simultaneously on the device and a single image of such grid is acquired by the CCD. The grid used to estimate the PSF for the optical setup is reported in Fig. 4.6 (a). It consists of a 15×15 array of ON mirrors, separated one from the surroundings by 14 OFF mirrors. The illustrated area represent the 400 pixels side square used for all the image in this chapter, as already mentioned in Sec. 4.1.2. The area covered by the grid is smaller that this central square: the grid fills a region of 2.87 mm on the DMD screen, that corresponds to 143.64 μm on the atomic plane. This DMD grid is imaged by the optical system on the atomic plane and observed with the CCD. As described in Sec. 3.4.2, an affine transformation has to be applied to the image acquired by the CCD, in order to make it comparable to the DMD image. Such transformed image is reported in Fig. 4.6 (b), and Fig. 4.6 (c) illustrates a detail of (b): we can see that the image of a single mirror covers just over 1 pixel.

To measure the PSF, we need to estimate the dimensions of each point in Fig. 4.6 (b) with a Gaussian fit. The results of such fits are stored in a 15×15 matrix and reported in Fig. 4.7. The (i, j) value of such matrices correspond to the σ_x and σ_y of the Gaussian fit for the (i, j) point in the grid. For each matrix the mean value of σ and the relative error is evaluated. For the horizontal direction we obtain a mean value of (0.55 ± 0.02) μm on the atomic plane, and a relative error of 3.6%. In the vertical direction the mean value is (0.59 ± 0.03) μm on the atomic plane, with a relative error of 5.1%. We can consider the mean of these two values as a measurement of the PSF size; that is $\sigma = (0.57 \pm 0.03)$ μm.

Two important conclusion follow from these results. First, we see that the measured value of σ is slightly over the PSF size of 0.523 μm predicted by the numerical simulation: their difference is about 8%. Moreover, the measured mean value of the single mirror image size is consistent with the simulated one of 0.583 μm. We can conclude that the deformation of a single mirror image is solely due to diffraction: aberrations barely affect the PSF of the optical system, which behaves as diffraction-limited. Secondly, the change in size of the PSF among the region of interest is of the order of 4%.

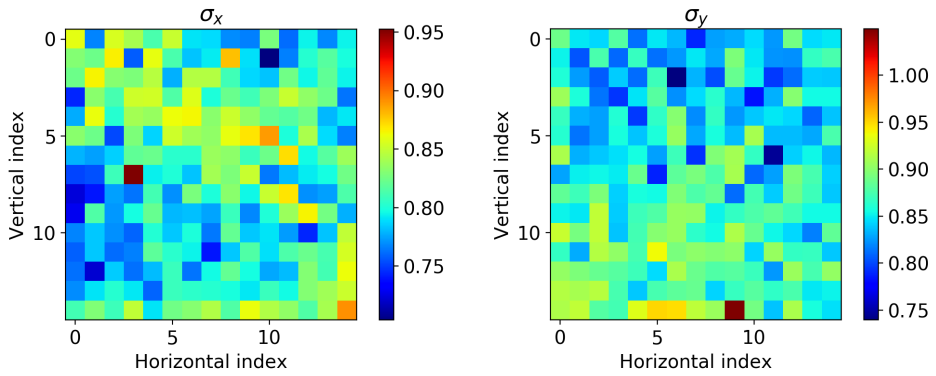

(a) **(b)**

Figure 4.7: Dimensions of the grid points in the horizontal and vertical direction. For each point a two-dimensional Gaussian fit is performed, and the values of σ_x and σ_y are stored in the plotted matrices.

Therefore, all the points in the examined area of the DMD mirrors array are imaged quite in the same way by the optical system.

Optimization of the objective position

The method for measuring the PSF already illustrated can be also used to optimize the alignment of the optics in the setup. In particular, it is very useful to find the optimal position of the left objective in Fig. 4.2. This is mounted on a three-dimensional translation stage, in order to be able to fine-tune its position. The accuracy of the imaging of the atomic plane into the CCD deeply depends on the position of the second objective, so the PSF measurement method provides a fundamental tool to achieve high resolution for the system. The alignment procedure is illustrated in Fig. 4.8: the three movement for the objective are indicated as longitudinal, in the direction of propagation of the laser beam, vertical and lateral, in the orthogonal plane respect to the propagation direction. For each direction, the movement of the objective is controlled by a micrometer drive, that enable to fine-tune its position. The resolution of the optical system is particularly sensitive to the longitudinal position of the objective, because it fixes the focus of the object. On the other hand, vertical and lateral movement changes only the portion of the image in the atomic plane observed by the objective and are thus less sensitive than the longitudinal one. While moving in these directions the position of the objective, we expect to modify its optical behaviour only in distances comparable with its field of view, that is 23 mm for the one used in this thesis work. Therefore, micrometer movements will slightly affect the imaging properties of the objective, but still an optimization of the resolution can be done.

To optimize the alignment we operate as following: the objective is moved in one direction at a time and for each position a PSF measurement with the single mirrors grid is performed, as described in the previous section. The sizes of the imaged points in the horizontal and vertical directions are stored in matrices similar to the ones in

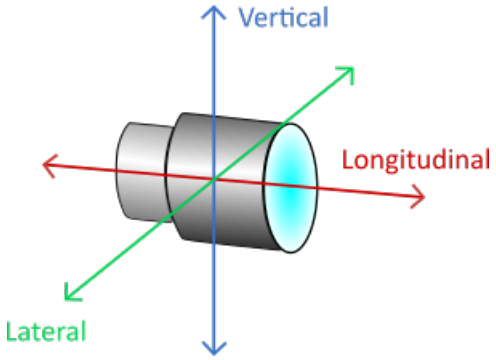

Figure 4.8: Illustration of the movement for the optimization of the objective position

Fig. 4.7, to then calculate the mean value and the relative error of σ_x and σ_y for each measurement. The best objective position is then chosen comparing these obtained values for several positions: for the longitudinal direction only the focus of the image matters, so the best position is the one with the minimum size of single mirrors image. For the other two direction is instead important that the single mirrors image is as much uniform as possible all over the grid. Therefore, the best position is the one with the minimum relative error in the points size. Finally, from the gradient of σ_x and σ_y inside the matrices is possible to identify the aberrations that may affect the optical system.

The optimization of the objective position done for this thesis work is illustrated in Fig. 4.9, 4.10 and 4.11. Here the σ_x and σ_y matrices, their mean value and relative error for the different position are reported. The displacement values are taken respect to an arbitrary initial position of the objective. For each direction the best position is the one marked with a red rectangle. The first optimization is in the longitudinal direction to fix the focus of the objective, reported in Fig. 4.9. The best position is found to be with a displacement of $\Delta x_{Long} = +0.010$ mm, where the mean sizes of the spot are: $\bar{\sigma}_x = (0.62 \pm 0.05)$ μm and $\bar{\sigma}_y = (0.50 \pm 0.03)$ μm on the atomic plane. As already mentioned, the resolution of the system is very sensitive on a change in the longitudinal direction: we can see that a movement of 5 μm modify drastically the sizes of the PSF. Then we proceed with the lateral position optimization, starting from the best longitudinal one already found. From Fig. 4.10, we can see that the system is less sensitive in a change in position: moving less than 50 μm will not modify the optical behaviour of the objective. The best lateral position is for a displacement of $\Delta x_{Lat} = +0.25$ mm, where the mean PSF sizes are: $\bar{\sigma}_x = (0.56 \pm 0.03)$ μm and $\bar{\sigma}_y = (0.57 \pm 0.03)$ μm on the atomic plane, with relative errors of 4.9% and 5.0% respectively. We can see that the spot sizes are quite uniform inside the grid and a clear direction for the gradient of sizes cannot be found. Finally, the vertical position of the objective is optimized, as reported in Fig. 4.11. The best one is found to be for a displacement of $\Delta x_{Vert} = 0$ mm, where the mean spot sizes are: $\bar{\sigma}_x = (0.55 \pm 0.02)$ μm and $\bar{\sigma}_y = (0.59 \pm 0.03)$ μm on the atomic plane, with relative errors of 4.4% and 4.3% respectively.

In conclusion, we can say that the measured PSF is spatially invariant: besides

the relative error of about 5% for the sizes of points in the grid, no gradient direction for them can be found. Furthermore, the measured value of PSF is consistent with the numerically simulated one of 0.583 μm. Therefore, it confirms the fact that the optical system is not affected by aberration and can be considered diffraction-limited. Only a slight astigmatism of the laser beam appears from the performed measurement: from the longitudinal optimization we can see that the minimum values for $\bar{\sigma}_x$ and $\bar{\sigma}_y$ do not occur for the same objective position: in the horizontal direction we have the minimum of $\bar{\sigma}_x = (0.53 \pm 0.03)$ μm for a displacement of $\Delta x_{Long} = +0.005$ mm and $\Delta x_{Long} = +0$ mm, wile for the vertical direction the minimum is $\bar{\sigma}_y = (0.50 \pm 0.03)$ μm for $\Delta x_{Long} = +0.10$ mm. That is, focuses in the two direction are $5 - 10$ μm distant.

The DMD-based method improved in this thesis work is a powerful technique to directly measure the Point Spread Function of an optical system. With such method we obtained that our optical system is almost diffraction-limited, as the value of the measured PSF size is consistent with the numerically simulated one. The measurement provides also information about the aberrations that affect the optical system: in our case only a slight astigmatism of the laser beam has been observed. We conclude that the optical system used in this chapter has an high resolution of $2\sigma = (1.14 \pm 0.05)$ μm, where σ is the mean value between σ_x and σ_y.

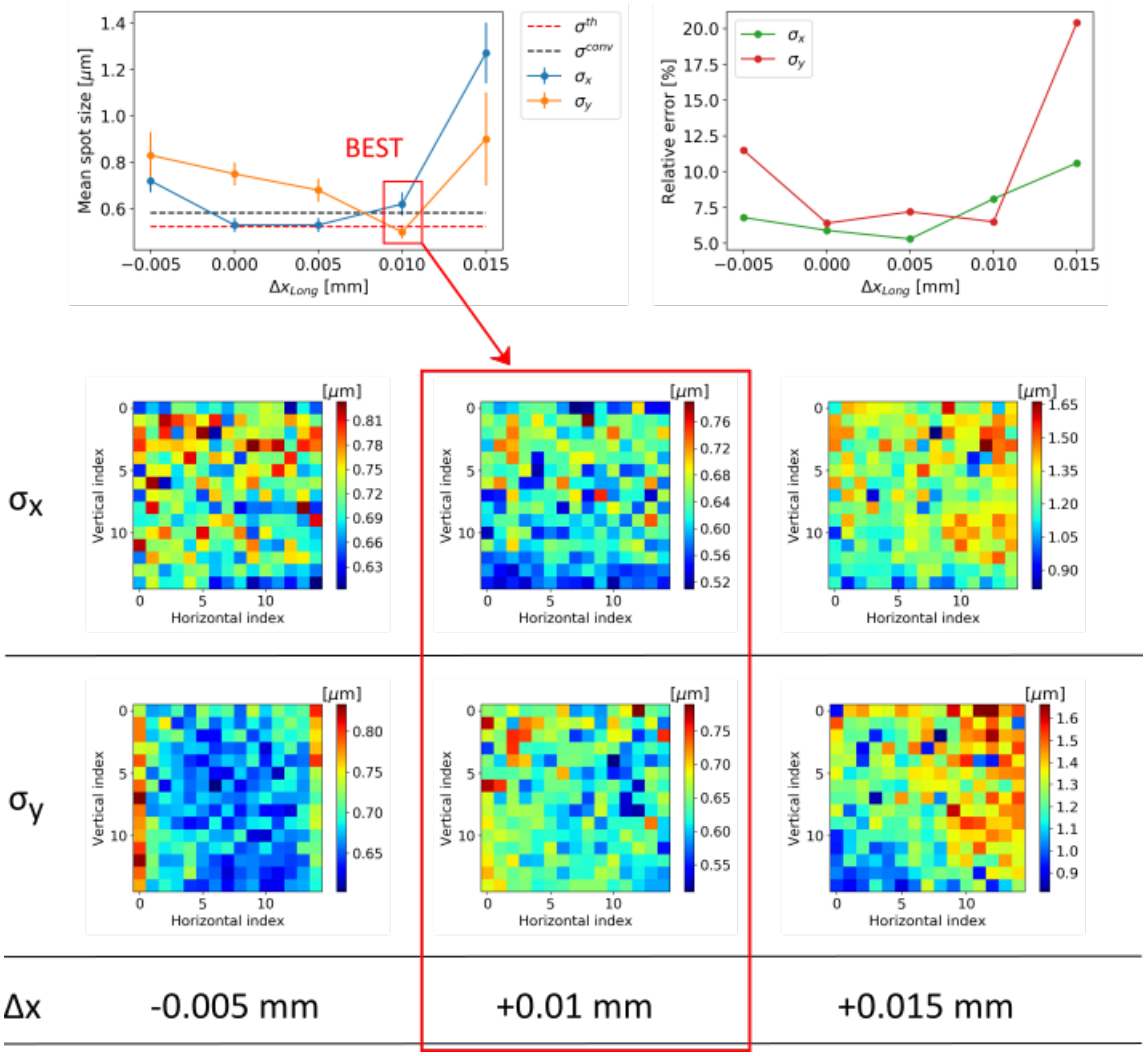

Figure 4.9: Measured value of PSF size for the optimization in the longitudinal direction. The mean value of σ_x and σ_y and their relative error are plotted versus the displacement in the longitudinal direction Δx_{Long}. The dashed lines in the σ plot represent the simulated value of the PSF size $\sigma^{th} = 0.523$ μm (red dashed line) and the simulated value of the size of a single mirror image $\sigma^{conv} = 0.583$ μm (black dashed line). The best position is chosen to be the one with minimum size of the spot and corresponds to the value of $\Delta x_{Long} = +0.01$ mm. In the grid below the σ_x and σ_y matrices for three values of displacement are reported.

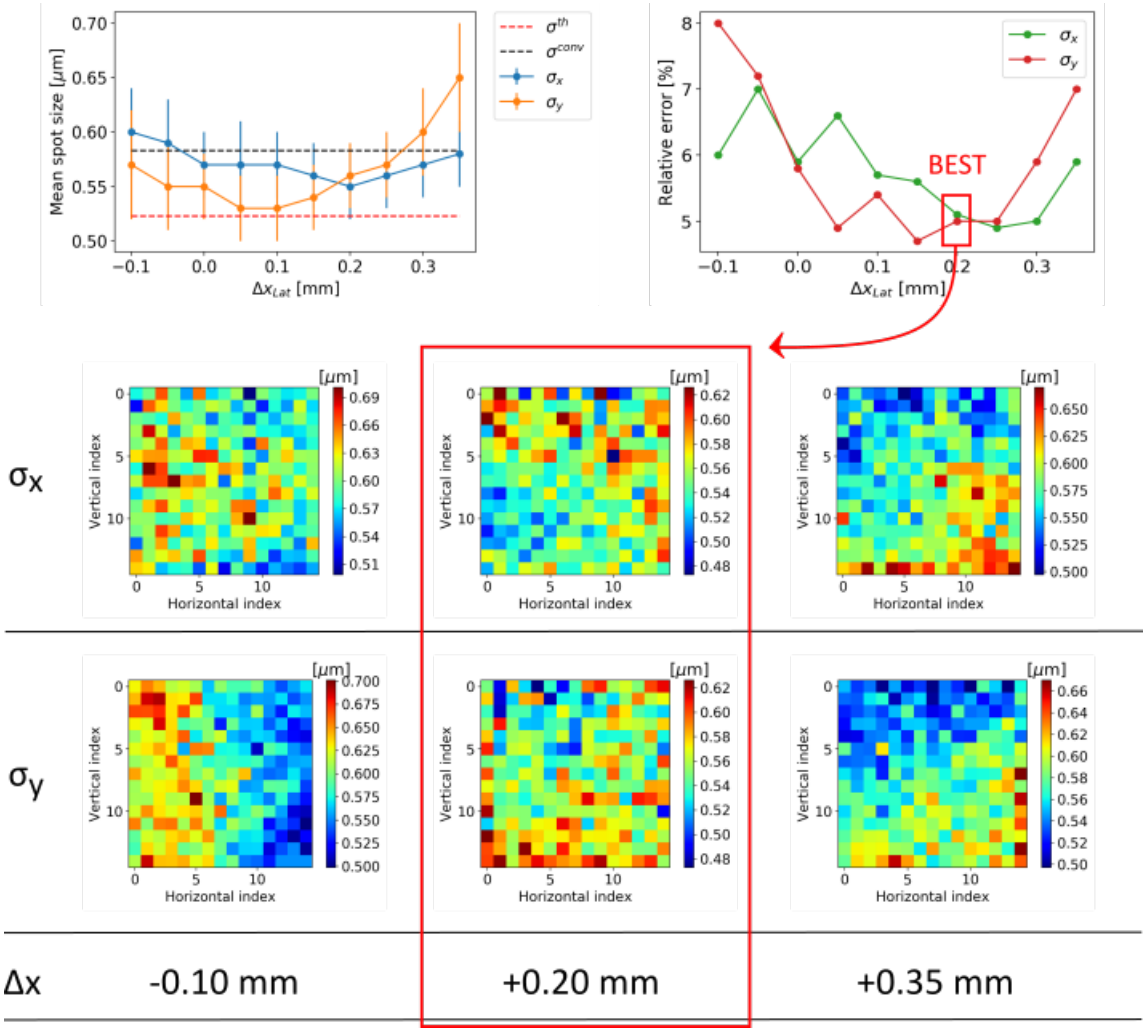

Figure 4.10: Measured value of PSF size for the optimization in the lateral direction. The mean value of σ_x and σ_y and their relative error are plotted versus the displacement in the lateral direction Δx_{Lat}. The dashed lines in the σ plot represent the simulated value of the PSF size $\sigma^{th} = 0.523$ μm (red dashed line) and the simulated value of the size of a single mirror image $\sigma^{conv} = 0.583$ μm (black dashed line). The best position is chosen to be the one with minimum relative error in the σ matrices and corresponds to the value of $\Delta x_{Lat} = +0.20$ mm. In the grid below the σ_x and σ_y matrices for three values of displacement are reported.

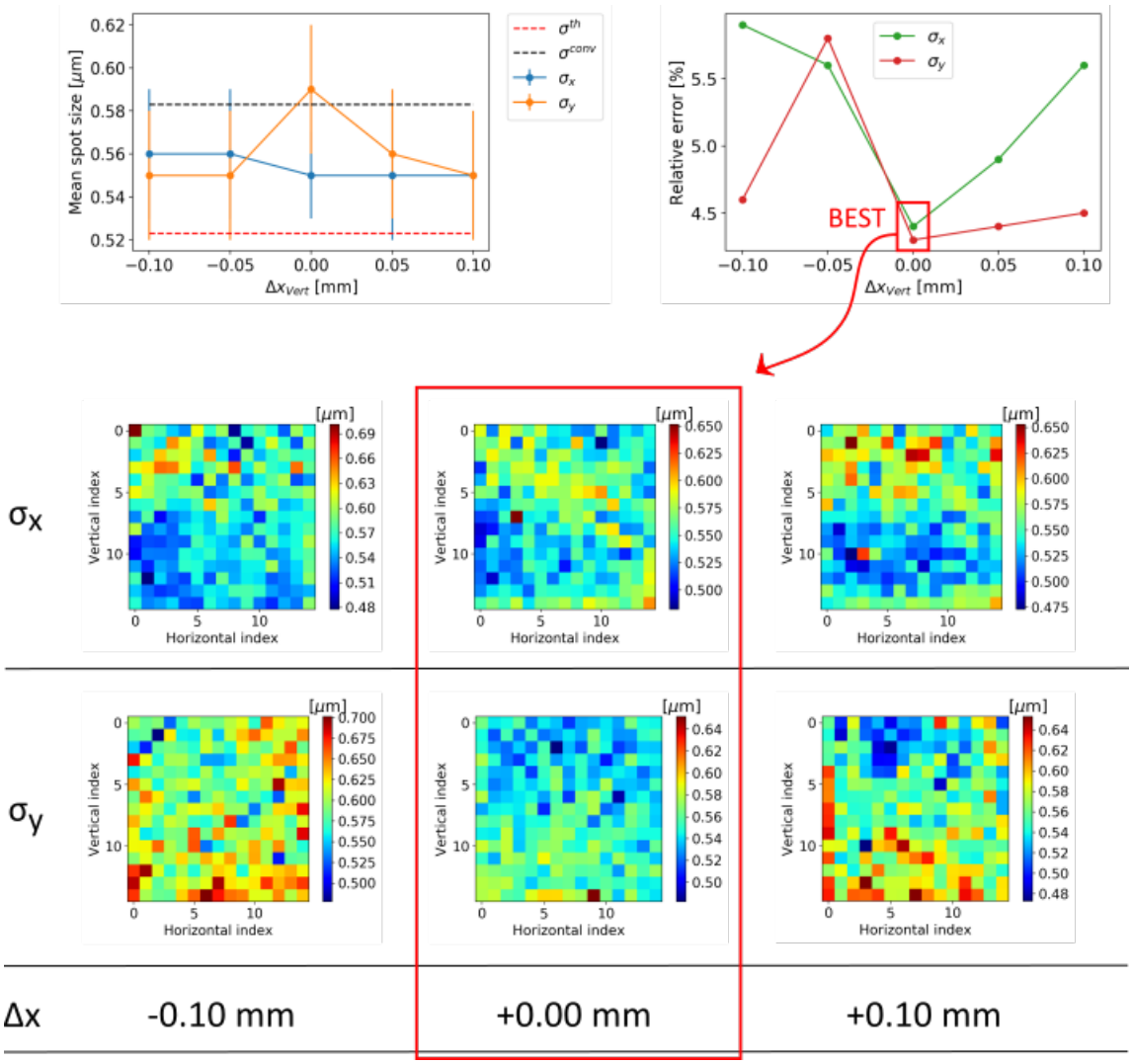

Figure 4.11: Measured value of PSF size for the optimization in the vertical direction. The mean value of σ_x and σ_y and their relative error are plotted versus the displacement in the vertical direction Δx_{Vert}. The dashed lines in the σ plot represent the simulated value of the PSF size $\sigma^{th} = 0.523$ μm (red dashed line) and the simulated value of the size of a single mirror image $\sigma^{conv} = 0.583$ μm (black dashed line). The best position is chosen to be the one with minimum size of the spot and corresponds to the vale of $\Delta x_{Vert} = +0.0$ mm. In the grid below the σ_x and σ_y matrices for three values of displacement are reported.

4.2 Disordered optical potentials

As already mentioned in Chapter 1, implementing disordered potentials to atomic clouds is interesting to study localization effects and, in the framework of quantum simulation, to introduce the randomness of impurities characteristic of any real material. A disordered light pattern can be created with the DMD setting the state of each mirror randomly. An high resolution of the optical system is then necessary to image such disordered pattern on the DMD screen to the atomic plane. From the PSF measurement of the previous section we are guaranteed that this can be done by our optical system: a single mirror can be imaged on the CCD. But, such image is distorted by the PSF of the optical system, so that the disordered light pattern created on the atomic plane will never be the same as the image sent to the DMD screen.

The purpose of this section is to investigate the properties of the disordered light pattern imaged on the atomic plane. To do so, several disordered images have been used, differing in size of the single disorder element w and in density of disorder n, defined as the ratio between the number of ON mirrors and their total number. These matrices are defined as Bernoulli distribution of ON mirrors: for $w = 1$ pixel the state of the mirror in the (i, j) is randomly decided to be:

$$M_{i,j} = \begin{cases} \text{ON} & \text{with probability } p, \\ \text{OFF} & \text{with probability } 1 - p \end{cases} \tag{4.8}$$

As pixels are dimensionless units, the density of disorder in a DMD images n correspond to the probability p of ON mirrors. To obtain images with bigger disorder elements, the DMD mirrors array is divided into w sized clusters of pixels and the state of each cluster is defined to follow the same Bernoulli distribution as before. Examples of such images are shown in Fig. 4.12. In the following work several DMD disordered images has been used. In particular, we considered images with impurity dimension varying from 1 to 6 pixels, that correspond to 0.68 μm and 4.10 μm on the atomic plane respectively, and with probability from 0.05 to 0.7.

By projecting such images with the DMD, a characterization of the disordered light pattern can be done. We focused our attention in two different kinds of disordered patterns: speckles and point-like. By now, speckles optical potentials have been the standard disorder used in atomic system. We call speckles the granular light pattern created when coherent light is reflected or diffused by a rough surface. They are usually generated by using a glass plate with a rough surface that exhibits a variability of its thickness in a scale comparable with the light wavelength. Depending on the optical path experienced, different portions of the incoming light acquire different phases. After the glass the optical wave results of many coherent component of wavelets, and the consecutive interference of the de-phased but coherent wavelets translates in the granular pattern of intensity that we call speckles. On the other hand, point-like disorder has a conceptually different basis. It is defined as the random distribution of point-like spot of light, resembling the presence of finite impurity once focused on the atomic cloud. The shape of such potential is not granular, as in the speckles case, but

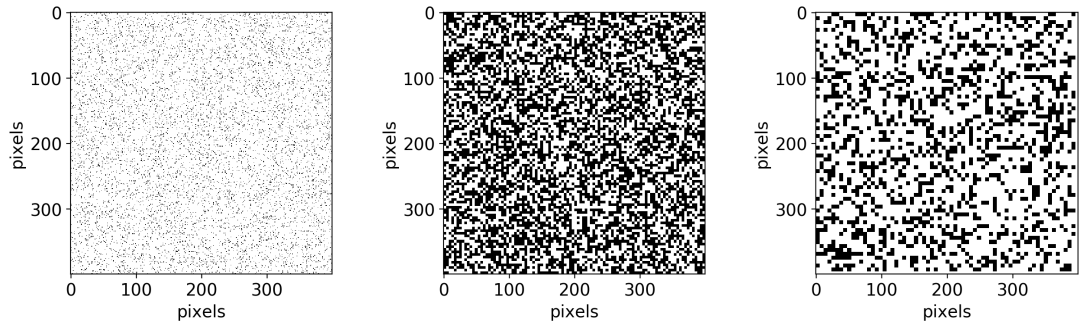

(a) $w = 1$ pixel, $n = 0.05$ **(b)** $w = 4$ pixel, $n = 0.5$ **(c)** $w = 6$ pixel, $n = 0.3$

Figure 4.12: Examples of DMD images used to implement disordered potential. w is the dimension of a single element of disorder and n the disorder density.

rather step-like.

All the DMD image used for this section (Fig. 4.12) are defined to be point-like. However, the light pattern imaged on the atomic plane would never be the same as the DMD image sent to the device: the point-like object may be transformed in a speckles image because of the smoothing operation of the PSF of the optical system. In Sec. 4.2.1 we present the expected behavior of the optical system in imaging disordered pattern in dependence on the size of the PSF. In particular, it is shown that our optical system is capable to reproduce both a speckles and a point-like pattern. In Sec. 4.2.2 the statistical properties of the two light patterns are presented, in order to enlighten a way to characterize and distinguish between the two. Finally, in Sec. 4.2.3 the experimental characterization of disordered light pattern is presented, demonstrating the capability of the optical system to reproduce both speckles and point-like disorder and the possibility to tune between them.

4.2.1 Role of PSF in imaging disordered patterns

To implement a disordered potential, a random DMD image as in Fig. 4.12 is sent to the device and imaged on the atomic plane by the optical system in Fig. 4.2. As already mentioned, the PSF modifies the image on the atomic plane, smoothing its edges. This can lead to a transformation of the point-like disorder on the DMD screen to a speckles light pattern on the atoms. In particular, we expect the occurrence of such transformation when the PSF is capable to crate an overlap between two impurity elements that are distinct in the DMD image. When this happens, the electric field of the two impurities may interfere and create the granular pattern characteristic of speckles.

To understand if this transformation can occur in our optical system, we can compare the measured size of the PSF to the mean distance between two impurity elements in a disordered image. As presented in Sec. 4.1.4, for the optical system used in this section the PSF has a mean size of $\sigma = (0.57 \pm 0.03)$ μm. On the other hand, we can define the mean distance between impurities in a pattern with impurity size w and

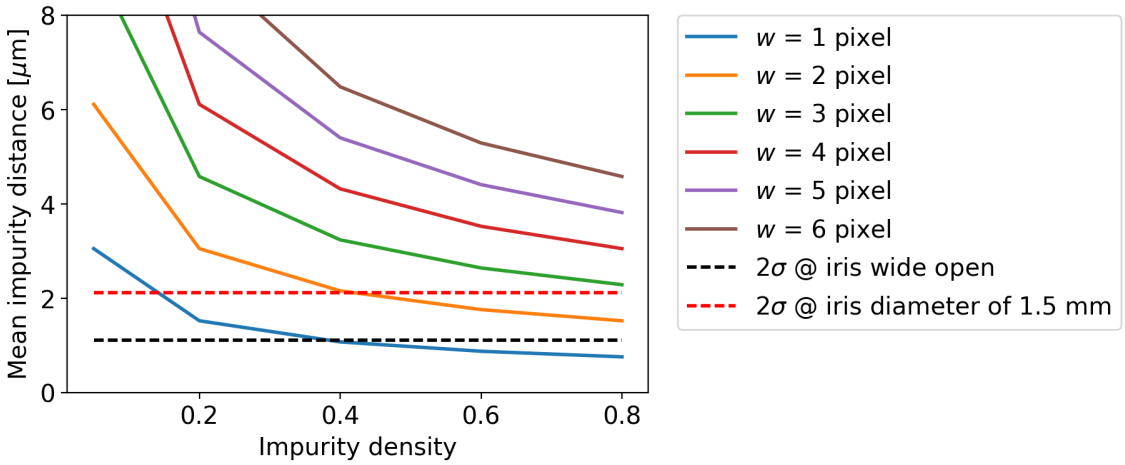

Figure 4.13: Comparison between the measured PSF of the optical system and the mean distance between impurities. The mean distance is plotted in dependence of the impurity density for several impurity size. The black dashed line represent the PSF size when the iris does not affect the resolution of the optical system, whereas the red dashed line correspond to the minimum iris diameter.

dimensionless density $n = p$ as:

$$d = \frac{w}{\sqrt{n}}. \tag{4.9}$$

We note that this distance has to be calculated in the atomic plane. We consider now two distinct impurities at distance d, each one of them is spread of σ by the PSF. If $d > 2\sigma$ the electric fields of the two do not overlap and we expect that the disordered pattern on the atomic plane will keep the characteristic of a point-like one. Instead, if $d < 2\sigma$ the electric fields of the two overlaps and interfere, and we expect to observe a speckles pattern imaged on the atomic plane.

In Fig. 4.13 the comparison between these two quantities is shown. The colored lines indicate the value of the mean distance between impurities versus their density for several impurity sizes expressed in DMD screen pixels. The black dashed line correspond to the measured value of the PSF 2σ. We can see that only for impurity size of 1 pixel the mean distance between impurities become comparable with the PSF, and it does it only for high values of density. Therefore, according to this analysis we expect to see a speckles pattern only in these cases.

To explore thoroughly the point-like to speckles pattern transition, an iris can be placed in front of the first objective (see Fig. 4.2) to reduce the most limiting aperture of the optical system, thereby increasing the size of the PSF. In particular, we consider several iris diameter: for each of them a measurement of the PSF has been done with the method discussed in Sec. 4.1.4, verifying the expected increase in its size. Fig. 4.14 shows the value of the measured size of the PSF in dependence of the iris diameter. We see that the maximum value is obtained for an iris diameter of 1.5 mm and correspond to $\sigma = (1.06 \pm 0.17)$ μm. This case correspond to the red dashed line in Fig. 4.13. Therefore, decreasing the iris diameter we expect to see a speckles pattern imaged on the atomic plane even for higher impurity size and lower densities.

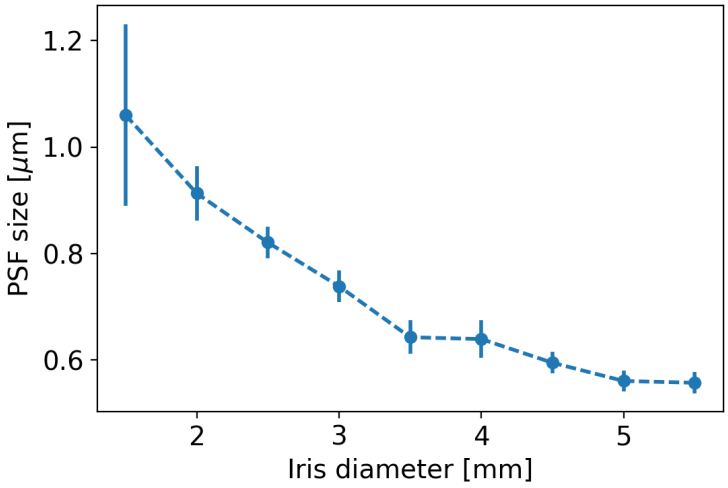

Figure 4.14: Measured values of the PSF size for several iris diameter.

4.2.2 Statistics of disordered light pattern

As we expect to reproduce both a speckles and a point-like pattern on the atomic plane, it is important to be able to distinguish between them. To do so, we can consider the statistical properties of the two light pattern. In the following the main statistical characteristic of speckles and point-like disorder are presented.

Speckles Disorder

We start considering the first-order statistical properties of laser speckles, that concerns a single point in the space. As already mentioned, for a speckles pattern the amplitude of the electric field at a given observation point (x, y) consists of a multitude of dephased contributions from different scattering regions of the rough surface used to generate it. Therefore, the amplitude of the electric field in the plane orthogonal to the laser propagation direction can be written as [58]:

$$A(x,y) = \sum_{k=1}^{N} \frac{1}{\sqrt{N}} a_k(x,y) = \frac{1}{\sqrt{N}} \sum_{k=1}^{N} |a_k| \exp^{i\phi_k}, \tag{4.10}$$

where the sum is performed over the N elementary phasor contribution to the electric field $a_k(x, y)$, and $|a_k|$ and ϕ_k are their modulus and phase respectively. The probability density function of the intensity of the speckles light pattern can be found, assuming that $|a_k|$ and ϕ_k are independent to each other and to $a_{k'}$ and $\phi_{k'}$, and that ϕ_k is uniformly distributed in $[-\pi, \pi]$. Under these assumption the mean values, the variances and the correlations of real and imaginary part of the electric field amplitude can be computed. As demonstrated in [58], they have zero means, identical variances, and are uncorrelated. Using the Central Limit Theorem, we can say that in the limit of $N \to \infty$ their distribution is asymptotically a Gaussian with the same mean and variance. Finally, the intensity probability density distribution can be computed from

such Gaussian distribution with a change in variables, that leads to [58]:

$$P(I) = \frac{1}{\langle I \rangle} \exp^{-\frac{I}{\langle I \rangle}}, \tag{4.11}$$

where $I = |A(x, y)|^2$ is the intensity and $\langle I \rangle$ its mean value. Therefore, the intensity distribution of speckles is exponential.

We now concentrate on the second-order statistics of speckles. To characterize the spatial properties of a speckles patter, we need to consider the autocorrelation function of intensity distribution:

$$\Gamma_I(\Delta r) = \langle I(r) I(r + \Delta r) \rangle , \tag{4.12}$$

where the average is over an ensemble of rough surfaces. For an imaging geometry that involves a single lens of diameter D and focal length f, it can be demonstrated that the autocorrelation function assumes the form [58]:

$$\Gamma_I(\Delta r) = \langle I \rangle \left[2 \frac{\lambda f}{\pi D \Delta r} J_1 \left(\frac{\pi D \Delta r}{\lambda f} \right) \right], \tag{4.13}$$

where λ is the laser wavelength and J_1 is the Bessel function of the first kind. The size of the speckles is fixed by the correlation length, defined as the first zero of the autocorrelation function, namely:

$$l_{corr} = 1.22 \frac{\lambda f}{D}. \tag{4.14}$$

We note that l_{corr} has the same expression of the diffraction limit of the lens.

Point-like Disorder

We now consider the point-like disorder and analyse its first and second-order statistical properties. To do so, a pattern as in Fig. 4.12 can be used to represent point-like disorder: in correspondence of the ON mirrors the light intensity is constant and equal to I_0, while in correspondence of the OFF mirrors the light intensity is null.

First of all, we determine the probability density function of the intensity for the point-like disorder. Since the possible values of intensity are only two (I_0 and 0), the probability density function is a Bernoulli distribution. It shows two peaks in correspondence of the intensity value of I_0 and 0, whose height is fixed by the dimensionless impurity density n: the probability to have an intensity value of I_0 is $p = n$, while the probability to have null intensity is $1 - p = 1 - n$. This behavior of the probability density function is intrinsic of the definition of point-like disorder we used for this thesis work, and can be verified considering a point-like disordered pattern as in Fig. 4.12 and computing the histogram of intensities of such matrix. This function shows the number of time a given value of intensity is present in the image, corresponding therefore to the probability density function of intensity for the image. Fig. 4.15 (a) report the computed histogram for several disordered images that differ in impurity density.

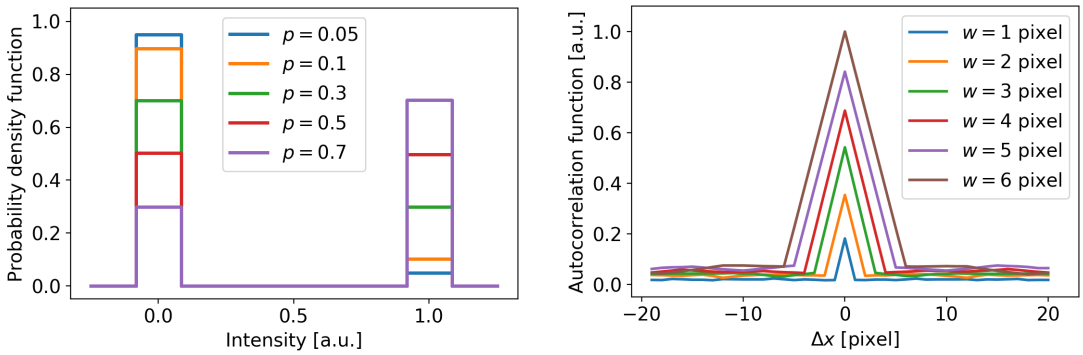

(a) Probability density function **(b)** Autocorrelation function

Figure 4.15: Statistical properties of the point-like disorder. Both the probability density function and the autocorrelation function have been calculated starting from a DMD image as in Fig. 4.12.

We consider now the autocorrelation function of point-like disordered. We use the following expression for the intensity to represent the pattern with density n of impurity of size w:

$$I(x,y) = \sum_{i=1}^{N} I_0 S_w(x_i) S_w(y_i), \tag{4.15}$$

where $N = nA$ is the number of impurities over a region of area A and S_w is a step function of width w defined as:

$$S_w(x_0) = \theta(x - x_0 + w/2)\theta(x_0 + w/2 - x), \tag{4.16}$$

where $\theta(x)$ is the Heaviside theta-function. Such expression for the intensity can be used to compute the autocorrelation function:

$$\Gamma_I = \langle I(r) I(r + \Delta r) \rangle = \langle I(x,y) I(x + \Delta x, y + \Delta y) \rangle \,, \tag{4.17}$$

where the average is over an ensemble of different random point-like pattern. We can substitute the ensemble average with an integral over the area of the disordered pattern because of the homogeneity of such pattern. Thus we have:

$$\Gamma_I = \int_{-L/2}^{L/2} dx \int_{-L/2}^{L/2} dy I(x,y) I(x + \Delta x, y + \Delta y), \tag{4.18}$$

where we have considered a square area of side L covered by the disordered pattern. Using Eq. (4.15) for the intensity, we obtain:

$$\Gamma_I = I_0^2 \sum_{i,j} \int_{-L/2}^{L/2} dx S_w(x_i) S_w(x_j + \Delta x) \int_{-L/2}^{L/2} dy S_w(y_i) S_w(y_j + \Delta y) \tag{4.19}$$

The two integrals can be treated separately. Considering the one over the x variable, we have:

$$\int_{-L/2}^{L/2} dx S_w(x_i) S_w(x_j + \Delta x) = \int_{x_i - w/2}^{x_i + w/2} dx S_w(x_j + \Delta x), \tag{4.20}$$

because the only effect of the step function $S_w(x_i)$ is to restrict the region over which we integrate. The previous integral assume different values depending on i and j.

If $i = j$ we have that the two step functions overlap for each impurity in the pattern, so the integral is non-zero. In particular, we obtain:

$$\int_{x_i-w/2}^{x_i+w/2} dx S_w(x_i + \Delta x) = \begin{cases} w - |\Delta x| & \text{if } |\Delta x| < w, \\ 0 & \text{otherwise.} \end{cases} \tag{4.21}$$

On the other hand, when $i \neq j$ the integral is non-zero only when the displacement Δx is such that the step functions of two impurities in different region of the pattern overlap. But, for each x_i in the sum over all the impurities it will happen with a different displacement Δx because of the randomness of the light pattern. Therefore, when $i \neq j$ the former integral may be non-zero for a given displacement, but when summed over all the impurities of the pattern this contribution become negligible because it is non-zero only for few i in the sum.

Putting together all these statement and considering the integral over the y variable too, we obtain the following expression for the autocorrelation function:

$$\Gamma_I = \begin{cases} I_0^2 N(w - |\Delta x|)(w - |\Delta y|) & \text{if } |\Delta x|, |\Delta y| < w, \\ \sim 0 & \text{otherwise.} \end{cases} \tag{4.22}$$

Therefore, the autocorrelation function for a point-like disordered pattern has a triangular shape, when observed in one direction at a time. This conclusion can be verified computing numerically the autocorrelation function for a point-like pattern as in Fig. 4.12 (b). The horizontal profiles of the autocorrelation function for several pattern differing in impurity size w are shown in Fig. 4.15. We see that the numerical computation confirms our calculations.

In conclusion, speckles and point-like pattern differ both in intensity probability density and in autocorrelation function. Studying such properties of the light pattern imaged on the atomic plane, it is thus possible to understand if the disorder can be properly considered speckles of point-like. Moreover, the statistical properties can be used to characterize the transition from point-like to speckles, explored by modifying the ratio between the size of the PSF and the mean distance between two different disorder elements.

4.2.3 Characterization of disordered potentials

In this section the characterization of the disordered pattern imaged on the atomic plane is presented. To do so, several DMD imaged has been used and their image on the atomic plane has been acquired with the CCD. In particular, three quantities has been varied: the size of a disorder element w, the probability of the Bernoulli distribution of the DMD image p and the iris diameter ID. In this way it is possible to observe the transition from point-like to speckles disorder imaged on the atomic plane. Fig. 4.16 shows examples of these two kinds of disorder: the point-like pattern (a) is

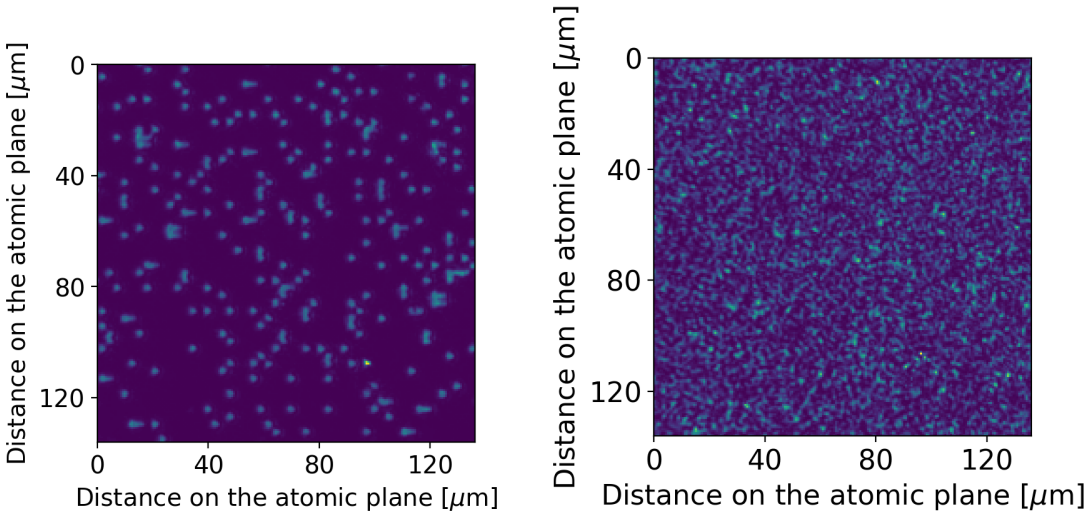

(a) Point-like disorder **(b)** Speckles disorder

Figure 4.16: Images of the point-like and the speckles disorder. The point-like pattern is obtained using a DMD image with impurities dimensions of 4 mirrors and Bernoulli probability of 0.1 and the iris wide, while the speckles one has DMD image with 1 mirror impurities dimensions and Bernoulli probability of 0.3 and an iris diameter of 1.5 mm.

realized using impurities of dimensions 4 mirrors on the DMD screen, that correspond to 2.7 μm on the atomic plane, with a Bernoulli distribution probability of 0.1 and the iris wide open. The speckles pattern (b) is instead obtained when the iris diameter is 2.0 mm for a DMD image with impurities dimension of 1 mirror and a probability of the Bernoulli distribution of 0.3. Differences between the two are clear even at first sight: the speckles image displays its typical granular pattern, while in the point-like one we can clearly see the alternation between region of light and darkness. We note that to obtain the two images in Fig. 4.16 the Gaussian profile of the incoming laser beam of the DMD has been removed. To do so, an image of the Gaussian profile, observable when all the DMD mirrors are ON, is acquired and used to rescale the disorder profile.

To fully characterize such disordered images a statistical analysis is performed. First of all, the probability density function of each acquired disordered image has been calculated. This function is obtained simply computing the histogram of the matrix, that counts the number of pixels in the acquired image that have a given intensity value. In Fig. 4.16 the probability density function for the speckles pattern and its exponential fit are shown. To compute the fit only data after the peak maximum have been considered. The data at low intensity deviate from the exponential behavior of the intensity probability density function for speckles as the density of disorder element is high enough to let no regions of darkness. We can see that the exponential trend is well suited for the probability density function, as expected for a speckles pattern of light, as in Eq. (4.11). However, for high intensity value it is possible to see a deviation between the experimental data and the fit. Here the information about the statistical properties of the pattern are quite none because this region corresponds to

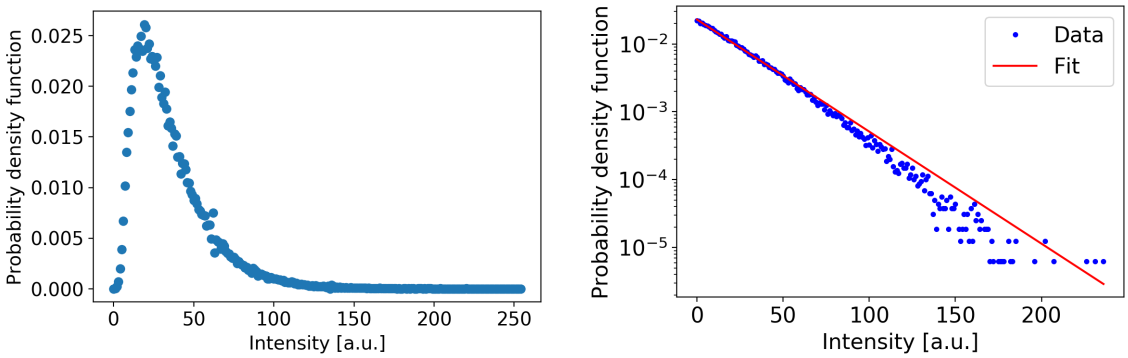

(a) Probability density function of the intensity for the speckles pattern

(b) Exponential fit of the probability density function

Figure 4.17: Probability density function for the speckles pattern and its exponential fit with the function: $y = A\exp^{-\alpha x}$. The estimated fit parameter are: $A = (22.89 \pm 0.07) \times 10^{-3}$, $\alpha = (38.02 \pm 0.18) \times 10^{-3}$ a.u.$^{-1}$, that correspond to a mean intensity $\langle I \rangle = (26.30 \pm 0.12)$ a.u.

intensity value with almost zero counts in the histogram. Therefore, we can say that the probability density function for the considered image pattern is exponential, as it should be for a speckles pattern.

The behavior of the probability density function of intensity for point-like pattern is not as clear as for the speckles instead. In particular, the presence of the two distinct peaks characteristic of the Bernoulli distribution is not observable for all the point-like images, but rather they appear only for high probability when the dark region of the image is small. Fig. 4.18 shows the histograms of the point-like patterns obtained with $w = 4$ mirrors on the DMD screen and for several probabilities, all with the iris wide open. We can see the appearance of a peak for high intensity only for probabilities higher that 0.3. That means that for the image in Fig. 4.16 (a), which seems clearly point-like, the probability density function is not the one of the Bernoulli distribution as it should be. Maybe that is because the intensity of the light spots is not homogeneously equal to a certain value I_0, but it varies continuously from a minimum to a maximum, so that the peak of counts at non zero intensity is broadened. The area of the peak is fixed by the probability of the Bernoulli distribution, so if the width of the peak is large, then its height has to be little. For low probability p, the height of the peak at

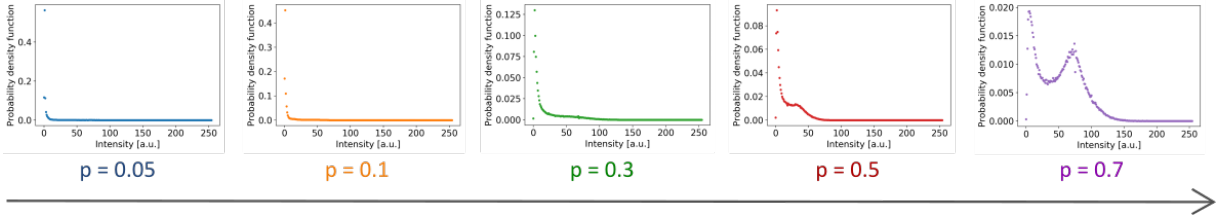

Figure 4.18: Probability density functions for a point-like disordered pattern with $w = 4$ pixel and different probability p.

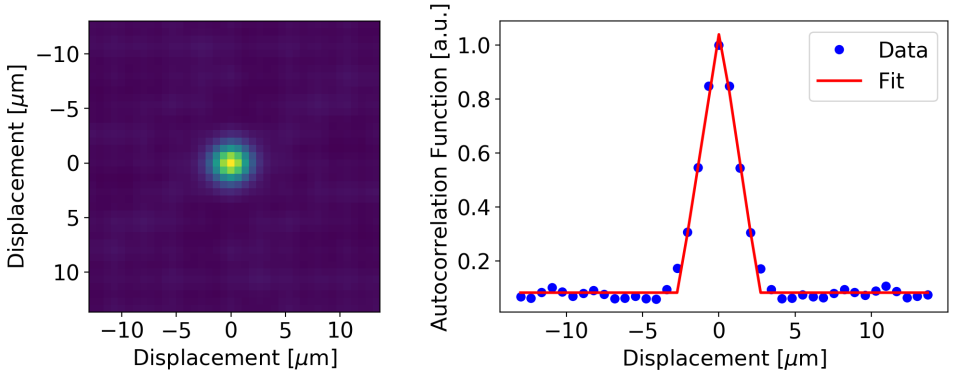

(a) Autocorrelation function for the point-like pattern

(b) Horizontal cut of the autocorrelation function

Figure 4.19: Autocorrelation function and its horizontal cut for the point-like pattern reported in Fig. 4.16 (a). The latter is obtained integrating (a) over 10 columns in the central region, and then fitted with the step function $y = m|x - x_0| + q$ for $|x - x_0| < x_1$, and $y = c$ otherwise. The estimated fit parameter are: $x_0 = (0.06 \pm 0.05)$ μm, $x_1 = (2.67 \pm 0.07)$ μm, $m = (0.359 \pm 0.015)$ a.u./μm, $c = (0.082 \pm 0.005)$ a.u. . The q parameter is not estimated by the fit, as it depends on m, x_1 and c. In particular, $q = c + m/x1$ and for the fit in figure it is: $q = (0.216 \pm 0.014)$ a.u. Comparing the fit function to Eq. (4.22), we note that x_1 corresponds to the impurity size w.

non zero intensity is so small that it cannot be seen in the histogram. Moreover, we note that in these cases the probability density function seems to have an exponential trend, the same of the speckles pattern.

Subsequently, we consider the autocorrelation function of each image acquired, both for speckles and point-like patterns for several values of w and p. This function is computed with the `correlate2d` function of the Python Scipy module, with the `wrap` circular boundary condition. In this way the two images are superimposed once shifted of a finite amount, and, when the shift is such that part of an image escape from the area of the other, the exceeding pixels are repeated at the opposite edge of the second image. This method is suitable for our characterization, as we assume the disordered patterns to be spatially homogeneous. The autocorrelation function of the point-like pattern of Fig. 4.16 (a) is shown in Fig. 4.19 (a), while in (b) the horizontal cut of such function integrated over 10 columns in the central part is plotted. Then, a fit of such one-dimensional function is performed according to the expected trend of Eq. (4.22). We can see that the fit function can well represent the experimental data, so we can conclude that the pattern of Fig. 4.16 (a) is actually a point-like disorder. In particular, from the fit we obtain an impurity size of $w^{exp} = (2.67 \pm 0.07)$ μm, consistent with the expected value of $w = 2.74$ μm for a DMD image with impurity cluster of 4 mirrors.

Fig. 4.20 shows the autocorrelation function of the speckles pattern reported in Fig. 4.16 (b). In (a) is presented the two-dimensional autocorrelation function, while in (b) the horizontal cut of such function integrated over 10 columns is plotted. The

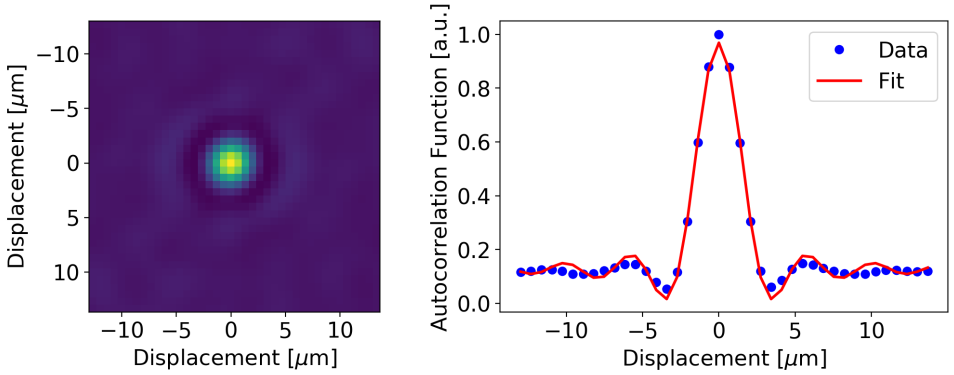

(a) Autocorrelation function for the speckles pattern

(b) Horizontal cut of the autocorrelation function

Figure 4.20: Autocorrelation function and its horizontal cut for the speckles pattern reported in Fig. 4.16 (b). The latter is obtained integrating (a) over 10 columns in the central region, and then fitted with a Bessel function $y = \frac{A}{B} J_1(\frac{x-x_0}{B})/(x - x_0) + C$, as expected for a speckles pattern (Eq. (4.13)). The estimated fit parameter are: $A = (0.76 \pm 0.02)$ μm a.u., $B = (0.67 \pm 0.01)$ μm, $x_0 = (-0.001 \pm 0.022)$ μm, $C = (0.126 \pm 0.004)$ a.u. . From Eq. (4.14) and the fit results, we obtain a correlation lenght for the speckles pattern of $l_{corr} = (2.61 \pm 0.04)$ μm.

one-dimensional profile of the autocorrelation function is fitted using a Bessel function, as suggested by Eq. (4.13). We can see that this function fits properly the profile of the measured autocorrelation function, so we can identify the image in Fig. 4.16 (b) as a speckles pattern. From the fit results and using Eq. (4.14), we can obtain the correlation length of the speckles pattern $l_{corr} = (2.61 \pm 0.04)$ μm.

The statistical analysis of the two images in Fig. 4.16, and in particular the study of the autocorrelation function, confirm their different nature. Therefore, our optical system is capable to image on the atomic plane both a speckles pattern and a point-like one, starting from Bernoulli distributed DMD images.

Transition from point-like to speckles disorder

We now investigate in detail the transition from point-like to speckles pattern. As already discussed in Sec. 4.2.1, we expect to have one pattern rather than the other depending on the value of the ratio $2\sigma/d$ between the size 2σ of the PSF of the optical system and the mean distance d between two different elements of disorder. Therefore, we study the properties of the several acquired images versus the ratio $2\sigma/d$.

A first property able to distinguish between speckles and point-like disorder is the value of the fluctuations of intensity respect to its mean value. Indeed, in a speckles pattern the intensity varies smoothly from a minimum to a maximum, while for a point-like disorder image only two values of intensity are permitted. Therefore, we expect that fluctuations are large for a point-like pattern and small for a speckles one. To demonstrate this scenario, the value of fluctuations $\Delta I/I$ has been calculated for

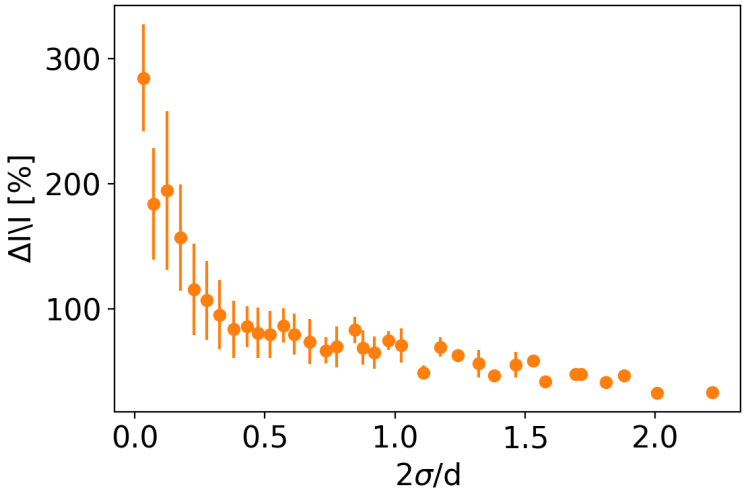

Figure 4.21: Measured intensity fluctuations in dependence of the ratio between the PSF size 2σ and the mean distance between two element of disorder d, calculated as in Eq. (4.9). For $\frac{2\sigma}{d} < 1$ we are in a point-like regime of large intensity fluctuations, while for $\frac{2\sigma}{d} > 1$ we enter in a speckles regime characterized by small intensity fluctuations.

all the imaged acquired at different disorder element size w, probability p and iris diameter ID. The dependence of intensity fluctuations on the ratio $2\sigma/d$ is obtained by calculating the value of the ratio for each image and then binning it in the range of 2σ and d considered. We calculate the mean value of the fluctuations and its standard deviation for all the points in the same bin and finally obtain the profile reported in Fig. 4.21. We see that for $2\sigma/d < 1$, where we expect to image a point-like disorder pattern on the atomic plane, intensity fluctuations are large, while for increasing values of $2\sigma/d$ fluctuations decrease, as the image on the atomic plane becomes more speckles-like. We note that the standard deviation error in the speckles regime is lower than in the point-like one. It is due to the fact that the number of acquired image with $2\sigma/d > 1$ is little compared to that in the point-like regime.

As discussed in the previous section, the histogram profile of the acquired image does not help in distinguish between the two different kinds of disorder. However, we can use a different information from the images histograms to characterize the speckles and the point-like regime: we can look to the number of count at very low intensity. As can be seen from Fig. 4.17 (a) and Fig. 4.18, for a speckles pattern the counts at very low intensity, at most the zero intensity counts, are little, while for a point-like one the image histogram takes its maximum exactly for low intensity. That is due to the fact that in a point-like image there are spots of light surrounded by dark regions, whereas in a speckles pattern darkness is almost completely cancelled out by the granularity of the pattern. We expect thus to have a small number of count at low intensity in the speckles regime, and large counts in the point-like regime. This apparently contradict the exponential behavior of the probability density function for speckles, as the exponential is maximum at zero intensity. But, as we can see from Fig. 4.17 (a), the histogram shows an exponential behavior only after a peak. At very low

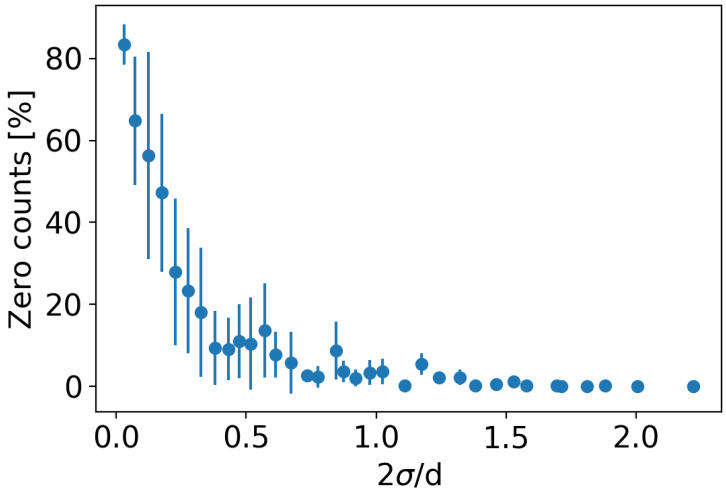

Figure 4.22: Counts at zero intensity in the images histogram versus the ratio between the PSF size 2σ and the mean distance between two element of disorder d, calculated as in Eq. (4.9). The value of zero counts is obtained considering the percentage of pixels in each acquired image where the intensity is less than 5, after the image have been rescaled to have the intensity maximum equal to 255.

intensity the count in the histogram are little because in a speckles pattern there are no regions of complete darkness. In Fig. 4.22 is reported the percentage of zero counts in dependence to the ratio $2\sigma/d$, obtained with the same binning procedure previously described. Each acquired image has been rescaled to have its maximum intensity value equal to 255, then the zero counts percentage has been calculated by summing the number of pixels where the intensity is less than 5. We can see that the zero counts percentage is high in the point-like regime for $2\sigma/d < 1$, whereas it decreases as the speckles regime is reached for $2\sigma/d1$, as we expected.

Finally, we can look to the autocorrelation function profile to characterize the transition between point-like and speckles. To do so, for each acquired image the autocorrelation function has been calculated, and the horizontal profile has been analyzed. In particular, for each one-dimensional autocorrelation function obtained both a triangular and a Bessel fit has been performed, with the same fit functions used for Fig. 4.19 (b) and 4.20 (b). Then, the residual sum has been calculated as the difference between the fit function and the experimental data in absolute value. Fig. 4.23 shows the values of the residual sum for a point-like fit with the triangular function and for a speckles fit with the Bessel function versus the ratio between the PSF size 2σ and the mean distance between two elements of disorder d. We can see that in the point-like regime for $2\sigma/d < 1$ the residual sum for the point-like fit is always less than the residual sum for the speckles fit, and vice versa in the speckles regime for $2\sigma/d > 1$.

In conclusion, the intensity fluctuations, the zero intensity counts and the residual sum for the autocorrelation fit confirm that our optical system is capable to perform a smooth transition from a point-like to a speckles disordered pattern imaged on the atomic plane. Such transition is driven by the change of the ratio between the PSF size

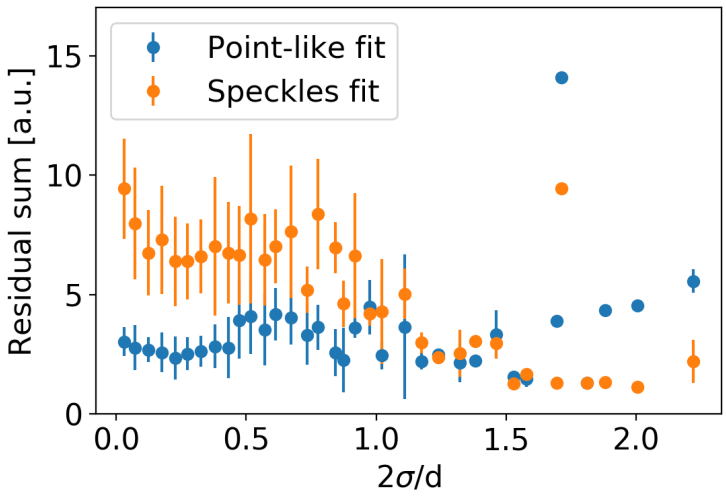

Figure 4.23: Residual sum for a point-like fit of the one-dimensional autocorrelation function with a triangular function and for a speckles fit with a Bessel function in dependence on the ratio between the PSF size 2σ and the mean distance between two elements of disorder d. The residual sum is calculated by summing the difference between the fit function and the measured autocorrelation function in absolute value for each point.

2σ, varied with the iris diameter, and the mean distance between two disorder element d, that depends on the the dimension and density of disorder. In particular, for $2\sigma < d$ we are in a point-like regime where the resolution of the optical system is high enough to image a point-like pattern on the atomic plane. On the other hand, when $2\sigma > d$ the resolution of the optical system is so low that the images of two different disorder element overlap, giving rise to a speckles pattern on the atomic plane.

Correlation length of the disordered pattern

Another important information can be extracted from the autocorrelation analysis performed on the acquired images: the size or the correlation length of the disordered pattern on the atomic plane. For a point-like pattern we can consider the size of a disorder element as the characteristic length scale, whereas for the speckles we have to consider the correlation length defined as in Eq. (4.14). In both cases these length scales can be obtained from the one-dimensional autocorrelation fit.

Fig. 4.24 shows the measured values of the point-like disorder size in dependence on the DMD image disorder size w for different value of the probability p (a) and the iris diameter ID (b). The plotted data correspond to acquired images in the point-like regime, where $2\sigma < d$. We can see that the disorder size for a fixed value of w depends on the probability p, but not on the iris diameter ID. In particular, w^{meas} grows linearly as w increases, except for the region at little w where the smoothing effect of the PSF begin to be remarkable. In any case, these results show that the size of the point-like disorder can be tuned by changing the probability and the dimension of a disorder element in the image sent to the DMD.

In Fig. 4.25 the measured values of the correlation length for the speckles patterns

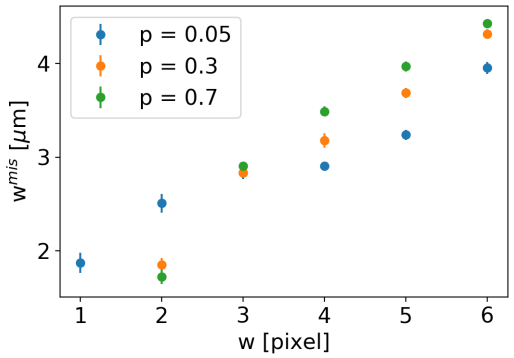

(a) Disorder size for different probability

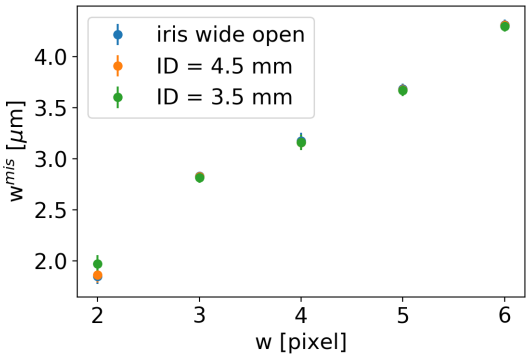

(b) Disorder size for different iris diameter

Figure 4.24: Measured size of the point-like disorder element in dependence on the DMD image disorder size for different value of the probability p (a) and the iris diameter ID (b).

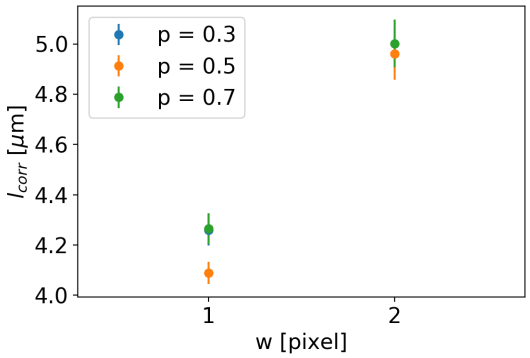

(a) Correlation length for different probability

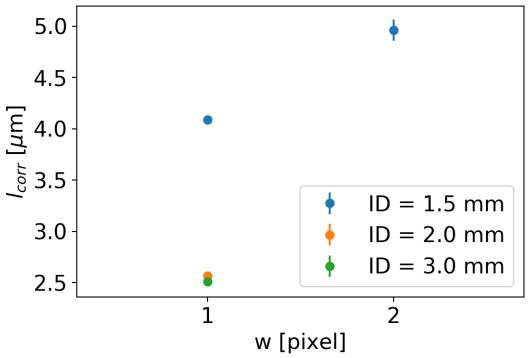

(b) Correlation length for different iris diameter

Figure 4.25: Measured correlation length of the speckles disorder in dependence on the DMD image disorder size for different value of the probability p (a) and the iris diameter ID (b).

are plotted in dependence on the DMD disorder size w for different value of the probability p (a) and the iris diameter ID (b). In this figure only the data from acquired images in the speckles regime, for $2\sigma > d$, have been considered. We see that the correlation length of the speckles pattern depends both on the probability and on the iris diameter. Therefore, also for a speckles pattern we are able to tune the correlation length to adapt it to the experimental necessities.

Therefore, our optical setup is capable to image both a point-like and a speckles pattern on the image plane with tunable characteristic length. The latter can be modified by acting on the image sent to the DMD, changing w or p, or on the iris diameter that modify the resolution of the system. Anyway, in both cases the characteristic length of the disordered pattern is of the order of μm, therefore comparable to the resolution of the optical system.

Conclusions

In this thesis work I have illustrated the possibility to create arbitrary optical potentials with a Digital Micromirror Device useful for the study of superfluidity phenomena of an atomic Bose-Einstein condensate.

Part of the work was devoted to the alignment and the optimization of a magneto optical trap for ^{87}Rb atoms. I performed the optimization of both the parameter of the 2D MOT and the 3D MOT, obtaining at the end a MOT of about 10^9 atoms with a temperature of about 200 μK and a loading efficiency of $\sim 10^8$ atoms/s. Such cooling technique represent the first step to obtain a condensate, as the critical temperature for the BEC transition is about 100 nK.

Then I focused my attention on the realization and characterization of optical potentials with the DMD. In particular, I developed two different optical setups: one for the realization of homogeneous optical potentials and the other for the implementation of disordered potentials on the length scale of a μm. For the first part, I used a spatial filter to smooth the spatial intensity profile of the DMD-made light pattern, and wrote a feedback program to improve the image quality. In particular, with such program it is possible to obtain images that differs around 5% from the target pattern sent to DMD. Moreover, such patterns have only a residual fluctuation in intensity of 1.4% on the length scale of about 5 μm, such that they can be considered homogeneous for what concerns the superfluid motion. Then, I analyzed the properties of time-dependent potentials than can be created with the DMD. In particular, the maximum velocity of a DMD-made time-dependent light pattern is of the order of mm/s, comparable to the critical velocity of an atomic superfluid.

Finally, I used an high-resolution optical system to realize disordered potentials on the length scale of μm. I developed a DMD-made technique for measuring the point spread function (PSF) of the optical system, and using it I verified that the optical setup I aligned was diffraction limited. Successively, I implemented two different kinds of disordered potentials: point-like and speckles pattern. They differ in both intensity probability function and autocorrelation function, so that studying such properties I performed a characterization of the two patterns. Using a point-like target pattern on the DMD it is possible to image on the atomic plane both a speckles and a point-like disorder, depending of the ratio between the size of the PSF 2σ and the mean distance between disorder elements d. For $2\sigma < d$ the resolution of the optical system is high enough to image a point-like pattern, wheres for $2\sigma > d$ the resolution of the optical system is so low that the images of two different disorder element overlap giving rise to

a speckles pattern. I investigated the point-like to speckles transition by using several target image with different d and by changing the PSF of the optical system with an iris. The results confirm what expected: the intensity fluctuation of the acquired image, the zero intensity counts and the residual sums of the fit of the autocorrelation functions versus the ratio $2\sigma/d$ have different behavior above and below the value $2\sigma/d = 1$. Both for speckles and for point-like patterns the characteristic length scale of disorder can be set adjusting the size and the density of disorder elements: in both cases it is of the order of μm.

In conclusion, this master thesis work presents the DMD as a powerful device to create optical potentials and demonstrate that it is well suited for applications in experiments with atomic superfluid. Both static and time-depending DMD-made potentials exhibit properties convenient for the study of superfluidity, and with an high-resolution optical system it is possible to create disordered potentials with controllable size and density of disordered element.

The main perspective of this work is to implement the optical potentials that I characterized on an atomic system. To do that, first a Bose-Einstein condensate of ^{87}Rb has to be produced, using the evaporative cooling technique to reach the low temperature of condensation ($T_C \simeq 100$ nK). Then, the DMD setup can be aligned on the experiment in order to imprint the optical potential on the atomic system. To do so, a custom-made high-resolution microscope objective has to be designed, in order to match the high resolution requests to the geometric experimental setup constrains. Finally, a ring-shaped optical potential will be imprinted of the atomic system, in order to study persistent current phenomena. As a repulsive optical potential will be used, the feedback program presented in this work cannot be used to create homogeneous intensity profile, but rather it will be implemented to have a feedback directly on the atomic population. The idea is to compare the target image of the DMD with the density distribution of atom, and perform a feedback process similar to that presented in this thesis.

Ringraziamenti

L'esistenza di questo capitolo è stata incerta fino alla fine. Inizialmente pensavo ai ringraziamenti con terrore, percependo l'imbarazzo nello scriverli e la difficoltà nel dare spazio a tutti col rischio di dimenticare qualcuno. Ma adesso che la fine è arrivata sento questo capitolo più che mai necessario perchè se sono riuscita a fare tutto quello che avevo programmato in questo periodo, e a sopravviverne, è anche merito vostro.

Prima di tutto un grandissimo grazie a tutte le persone con cui ho avuto il piacere di lavorare durante questo periodo di tesi. Grazie al mio relatore Francesco Minardi, che mi ha seguito con cura ed è riuscito ad alleggerire l'ansia degli ultimi giorni. Grazie a Giacomo Roati, che mi ha accolto nel laboratorio del Litio-6 per tutta la parte del DMD, spronandomi sempre verso nuove sfide fiducioso delle mie capacità. Grazie a tutte le componenti della BEC3: Sara Rosi, con cui ho condiviso i primi giochi col DMD, Alessia Burchianti, Chiara D'Errico e Chiara Fort, che mi hanno insegnato infinite cose con gentilezza e pazienza. Grazie a Francesco Scazza che mi ha aiutato ampiamente con i potenziali disordinati ed è riuscito a dare un senso al disordine nella mia testa. E grazie ad Andrea Amico, Pedro Tavares e Matteo Zaccanti che nei lunghi pomeriggi in cui i programmi non volevano funzionare mi hanno risollevato il morale con una battuta ed una gocciola. Un grazie speciale alla mia amica e compagna di laboratorio Eleonora Lippi: ci siamo sostenute e messe ansia a vicenda, lo stress di concorsi e tesi è stato più sostenibile con te.

Poi la mia grande e sempre presente famiglia, grazie per essermi stati accanto in questi lunghi mesi di clausura da tesi. Grazie alla mia mamma, che mi dimostra ogni giorno che nessuna sfida è troppo grande per poter essere affrontata. Grazie al mio babbo, che mi sostiene con tranquillità e ironia, ricordandomi sempre che prendersi troppo sul serio nuoce gravemente alla salute. Grazie a Luca che ascolta le mie lamentele e si schiera sempre dalla mia parte; grazie a Donatella che capisce al volo quello che intendo e sa cosa dire quando sono giù. Grazie ai miei fratelli: alla mia sorellina Ayla, che cresce sempre di più e diventerà una donna fantastica, capace di ascoltare e aiutare e arrabbiarsi al momento giusto, e al mio fratelligno Sebastiano che è già cresciuto, ma mantiene la voglia di giocare e scherzare di sempre. Grazie ai miei nonni: Nonna Lella e Nonno Sergio che mi hanno visto studiare come una matta nell'ultimo anno, senza disturbare o interrompendomi giustamente quando era il momento. Grazie perchè ci siete sempre, quando saltello allegra per la casa e quando mi rannicchio disperata sul divano, tutte le volte trovate il modo giusto di starmi accanto. Grazie al Nonno Sergio e Wilma, che credono in me e mi scusano per la lontanza

indotta dallo studio. Grazie ai miei zii e cugini: grazie Selenio e Roberta, sempre interessati ai miei impegni accademici e pronti a ideare piani B in caso la tecnologia venisse meno. Grazie a Sonia e Mario, che mi seguono curiosi, fotografando tutti i traguardi raggiunti. Grazie alla mia cugina Jenny, internazionale e innovativa, che mi offre uno sguardo sempre diverso sulle cose. Grazie agli zii Antonio e Isabella, Roberto e Jenny e alle cugine Gemma, Maria Laura, Cristina e Margherita, con cui ci divertiamo come cittine tutte le volte che ci vediamo.

Grazie a tutte le mie amiche, vecchie e nuove. Grazie a Franci e Sere, amiche immancabili del liceo, grazie per aver accettato le mie assenze di questo ultimo periodo e grazie per essere cresciute con me. Sei lunghi anni ci separano dalle avventure vissute sui banchi di scuola, ma abbiamo trovato il modo di restare insieme nonostante le diverse strade che percorriamo. Qualsiasi cosa ci riservi il futuro, so di poter sempre contare su di voi, che mi ascolterete senza giudicare e che capirete quello che mi passa per la testa, spero di essere in grado di offrirvi altrettanto. E grazie a Margherita, Sarah, Giulia e Margherita, amiche che mi ricordano che esistono mondi diversi dal mio, ma ugualmente ricchi e colorati. Grazie per tutte le serate passate insieme a parlare di cose frivole e meno frivole, nella giusta percentuale. Grazie a tutti i miei amici dell'università, con cui ho condiviso pranzi a mensa, esami e momenti felici. Vale la pena spendere tutto quel tempo in treno se all'università trovo persone come voi.

E infine grazie a Leonardo, con cui ho avuto la fortuna di condividere quasi tutto il mio percorso universitario. Sai farmi ridere e riflettere, sai di cosa ho bisogno prima che lo sappia io. Grazie per credere nelle mie capacità e per spingermi sempre a dare il massimo, rispettando i miei tempi e assecondando i miei sbalzi di umore.

Bibliography

[1] A. Einstein, *Quantentheorie des einatomigen idealen Gases*. Akademie der Wissenshaften, in Kommission bei W. de Gruyter, 1924.

[2] S. N. Bose, *Plancks gesetz und lichtquantenhypothese*. Springer, 1924.

[3] H. K. Onnes, "The resistance of pure mercury at helium temperatures," *Commun. Phys. Lab. Univ. Leiden*, vol. 12, no. 120, p. 1, 1911.

[4] P. Kapitza, "Viscosity of liquid helium below the l-point," *Nature*, vol. 141, no. 3558, p. 74, 1938.

[5] J. Allen and A. Misener, "Flow of liquid helium ii," *Nature*, vol. 141, no. 3558, p. 75, 1938.

[6] F. London, "The lambda-phenomenon of liquid helium and the bose-einstein degeneracy," *Nature*, vol. 141, pp. 643–644, 1938.

[7] J. Bardeen, L. N. Cooper, and J. R. Schrieffer, "Theory of superconductivity," *Physical Review*, vol. 108, no. 5, p. 1175, 1957.

[8] M. H. Anderson, J. R. Ensher, M. R. Matthews, C. E. Wieman, E. A. Cornell, *et al.*, "Observation of bose-einstein condensation in a dilute atomic vapor," *science*, vol. 269, no. 5221, pp. 198–201, 1995.

[9] K. B. Davis, M.-O. Mewes, M. R. Andrews, N. Van Druten, D. Durfee, D. Kurn, and W. Ketterle, "Bose-einstein condensation in a gas of sodium atoms," *Physical review letters*, vol. 75, no. 22, p. 3969, 1995.

[10] J. Abo-Shaeer, C. Raman, J. Vogels, and W. Ketterle, "Observation of vortex lattices in bose-einstein condensates," *Science*, vol. 292, no. 5516, pp. 476–479, 2001.

[11] K. Madison, F. Chevy, W. Wohlleben, and J. Dalibard, "Vortex formation in a stirred bose-einstein condensate," *Physical Review Letters*, vol. 84, no. 5, p. 806, 2000.

[12] M. R. Matthews, B. P. Anderson, P. Haljan, D. Hall, C. Wieman, and E. A. Cornell, "Vortices in a bose-einstein condensate," *Physical Review Letters*, vol. 83, no. 13, p. 2498, 1999.

[13] A. Kumar, N. Anderson, W. D. Phillips, S. Eckel, G. K. Campbell, and S. Stringari, "Minimally destructive, doppler measurement of a quantized flow in a ring-shaped bose–einstein condensate," *New Journal of Physics*, vol. 18, no. 2, p. 025001, 2016.

[14] T. Fukuhara, A. Kantian, M. Endres, M. Cheneau, P. Schauß, S. Hild, D. Bellem, U. Schollwöck, T. Giamarchi, C. Gross, *et al.*, "Quantum dynamics of a mobile spin impurity," *Nature Physics*, vol. 9, no. 4, pp. 235–241, 2013.

[15] D. Bellem, "Generation of spatially and temporally varying light po- tentials in optical lattices," Master's thesis, Ludwig-Maximilians-Universitat Munchen, 2011.

[16] C. J. Pethick and H. Smith, *Bose-Einstein condensation in dilute gases*. Cambridge university press, 2002.

[17] K. Huang, *Statistical Mechanics, 2nd.* Edition (New York: John Wiley & Sons), 1987.

[18] F. Dalfovo, S. Giorgini, L. P. Pitaevskii, and S. Stringari, "Theory of bose-einstein condensation in trapped gases," *Reviews of Modern Physics*, vol. 71, no. 3, p. 463, 1999.

[19] A. J. Leggett, "Superfluidity," *Reviews of Modern Physics*, vol. 71, no. 2, p. S318, 1999.

[20] L. Landau, "Theory of the superfluidity of helium ii," *Physical Review*, vol. 60, no. 4, p. 356, 1941.

[21] C. Cohen-Tannoudji and D. Guéry-Odelin, *Advances in atomic physics: an overview*. World Scientific, 2011.

[22] M. Inguscio and L. Fallani, *Atomic physics: precise measurements and ultracold matter*. OUP Oxford, 2013.

[23] R. Grimm, M. Weidemüller, and Y. B. Ovchinnikov, "Optical dipole traps for neutral atoms," *Advances in atomic, molecular, and optical physics*, vol. 42, pp. 95–170, 2000.

[24] A. J. Leggett, "Bose-einstein condensation in the alkali gases: Some fundamental concepts," *Rev. Mod. Phys.*, vol. 73, pp. 307–356, Apr 2001.

[25] T. Simula, S. Virtanen, and M. Salomaa, "Stability of multiquantum vortices in dilute bose-einstein condensates," *Physical Review A*, vol. 65, no. 3, p. 033614, 2002.

[26] S. Moulder, S. Beattie, R. P. Smith, N. Tammuz, and Z. Hadzibabic, "Quantized supercurrent decay in an annular bose-einstein condensate," *Physical Review A*, vol. 86, no. 1, p. 013629, 2012.

[27] C. Ryu, M. Andersen, P. Clade, V. Natarajan, K. Helmerson, and W. D. Phillips, "Observation of persistent flow of a bose-einstein condensate in a toroidal trap," *Physical Review Letters*, vol. 99, no. 26, p. 260401, 2007.

[28] A. Kumar, S. Eckel, F. Jendrzejewski, and G. K. Campbell, "Temperature-induced decay of persistent currents in a superfluid ultracold gas," *Physical Review A*, vol. 95, no. 2, p. 021602, 2017.

[29] S. Beattie, S. Moulder, R. J. Fletcher, and Z. Hadzibabic, "Persistent currents in spinor condensates," *Physical review letters*, vol. 110, no. 2, p. 025301, 2013.

[30] P. Halkyard, M. Jones, and S. Gardiner, "Rotational response of two-component bose-einstein condensates in ring traps," *Physical Review A*, vol. 81, no. 6, p. 061602, 2010.

[31] G. E. Marti, R. Olf, and D. M. Stamper-Kurn, "Collective excitation interferometry with a toroidal bose-einstein condensate," *Physical Review A*, vol. 91, no. 1, p. 013602, 2015.

[32] A. Ramanathan, K. Wright, S. Muniz, M. Zelan, W. Hill III, C. Lobb, K. Helmerson, W. Phillips, and G. Campbell, "Superflow in a toroidal bose-einstein condensate: an atom circuit with a tunable weak link," *Physical review letters*, vol. 106, no. 13, p. 130401, 2011.

[33] P. W. Anderson, "Absence of diffusion in certain random lattices," *Physical review*, vol. 109, no. 5, p. 1492, 1958.

[34] M. Piraud, L. Pezzé, and L. Sanchez-Palencia, "Quantum transport of atomic matter waves in anisotropic two-dimensional and three-dimensional disorder," *New Journal of Physics*, vol. 15, no. 7, p. 075007, 2013.

[35] P. A. Lee and T. Ramakrishnan, "Disordered electronic systems," *Reviews of Modern Physics*, vol. 57, no. 2, p. 287, 1985.

[36] D. Haviland, Y. Liu, and A. Goldman, "Onset of superconductivity in the two-dimensional limit," *Physical Review Letters*, vol. 62, no. 18, p. 2180, 1989.

[37] A. a. Goldman, "Superconductor-insulator transition in the two-dimensional limit," *Physics Today*, vol. 51, no. 11, p. 39, 1998.

[38] Y. Dubi, Y. Meir, and Y. Avishai, "Nature of the superconductor-insulator transition in disordered superconductors.," *Nature*, vol. 449, no. 7164, pp. 876–880, 2007.

[39] G. Roati, C. D'Errico, L. Fallani, M. Fattori, C. Fort, M. Zaccanti, G. Modugno, M. Modugno, and M. Inguscio, "Anderson localization of a non-interacting bose–einstein condensate," *Nature*, vol. 453, no. 7197, pp. 895–898, 2008.

[40] J. Billy, V. Josse, Z. Zuo, A. Bernard, B. Hambrecht, P. Lugan, D. Clément, L. Sanchez-palencia, P. Bouyer, and A. Aspect, "Direct observation of anderson localization of matter waves in a controlled disorder.," *Nature*, vol. 453, no. 7197, pp. 891–894, 2008.

[41] S. Kondov, W. McGehee, J. Zirbel, and B. DeMarco, "Three-dimensional anderson localization of ultracold matter," *Science*, vol. 334, no. 6052, pp. 66–68, 2011.

[42] F. Jendrzejewski, A. Bernard, K. Mueller, P. Cheinet, V. Josse, M. Piraud, L. Pezzé, L. Sanchez-Palencia, A. Aspect, and P. Bouyer, "Three-dimensional localization of ultracold atoms in an optical disordered potential," *Nature Physics*, vol. 8, pp. 398–403, 2012.

[43] W. Morong and B. DeMarco, "Simulation of anderson localization in two-dimensional ultracold gases for pointlike disorder," *Physical Review A*, vol. 92, no. 2, p. 023625, 2015.

[44] C. J. Foot, *Atomic physics*, vol. 7. Oxford University Press, 2005.

[45] C. Monroe, W. Swann, H. Robinson, and C. Wieman, "Very cold trapped atoms in a vapor cell," *Physical Review Letters*, vol. 65, no. 13, p. 1571, 1990.

[46] T. Tiecke, S. Gensemer, A. Ludewig, and J. Walraven, "High-flux two-dimensional magneto-optical-trap source for cold lithium atoms," *Physical Review A*, vol. 80, no. 1, p. 013409, 2009.

[47] J. Schoser, A. Batär, R. Löw, V. Schweikhard, A. Grabowski, Y. B. Ovchinnikov, and T. Pfau, "Intense source of cold rb atoms from a pure two-dimensional magneto-optical trap," *Physical Review A*, vol. 66, no. 2, p. 023410, 2002.

[48] K. Dieckmann, R. Spreeuw, M. Weidemüller, and J. Walraven, "Two-dimensional magneto-optical trap as a source of slow atoms," *Physical Review A*, vol. 58, no. 5, p. 3891, 1998.

[49] S. Weyers, E. Aucouturier, C. Valentin, and N. Dimarcq, "A continuous beam of cold cesium atoms extracted from a two-dimensional magneto-optical trap," *Optics communications*, vol. 143, no. 1-3, pp. 30–34, 1997.

[50] J. Noh, S. J. Park, C. Y. Park, W.-K. Lee, D.-H. Yu, and J. Mun, "High-performance experimental apparatus for large atom number 87 rb bose-einstein condensates," *Journal of the Korean Physical Society*, vol. 61, no. 7, pp. 1021–1027, 2012.

[51] D. McCarron, S. King, and S. Cornish, "Modulation transfer spectroscopy in atomic rubidium," *Measurement science and technology*, vol. 19, no. 10, p. 105601, 2008.

[52] G. C. Bjorklund, "Frequency-modulation spectroscopy: a new method for measuring weak absorptions and dispersions," *Optics Letters*, vol. 5, no. 1, pp. 15–17, 1980.

[53] S. M. Popoff, "wavefronthsaping/alp4lib: First release," Feb 2017.

[54] W. E. Born M., *Principle of Optics*. Cambridge University Press, 1999.

[55] E. Perego, "Generation of arbitrary optical potentials for atomic physics experiments using a digital micromirror device," Master's thesis, Università degli studi di Firenze, 2015.

[56] J. Goodman, *Introduction to Fourier Optics*. McGraw-Hill physical and quantum electronics series, W. H. Freeman, 2005.

[57] A. Allen, N. Parker, N. Proukakis, and C. Barenghi, "Isotropic vortex tangles in trapped atomic bose-einstein condensates via laser stirring," *Physical Review A*, vol. 89, no. 2, p. 025602, 2014.

[58] J. W. Goodman, *Speckle Phenomena in Optics: Theroy and Applications*. Robert and Co., 2007.